OPTICAL STUDIES OF SEMICONDUCTOR HETEROSTRUCTURES: MEASUREMENTS OF TUNNELING TIMES, AND STUDIES OF STRAINED SUPERLATTICES

Thesis by
Michael Kevin Jackson

In Partial Fulfillment of the Requirements
for the Degree of
Doctor of Philosophy

California Institute of Technology
Pasadena, California

1991
(Submitted July 23, 1990)

To my parents, Helen, Alan, and Tasha

Acknowledgements

I would like to thank my advisor, Dr. T.C. McGill, for the opportunity to work in the exciting and friendly research group that he has assembled. His ceaseless efforts to keep the group well-equipped and working on interesting problems are greatly appreciated.

In the course of working in Dr. McGill's research group, I have had the pleasure, both personally and professionally, of working with a great number of enthusiastic and talented people. I would especially like to thank those who have had the greatest impact on my time as a graduate student, in both work-related and personal matters: Dr. Richard Miles, whose patient introduction to optical experiments, keen insight, and steady encouragement have helped me tremendously; Dr. David Chow, whose unfailing good nature and concern for others made our years of sharing an office very enjoyable; and Dr. David Ting, whose friendly manner, and sound advice are greatly appreciated. I would like to thank Dr. Matthew Johnson for his patience in teaching me laboratory techniques, in particular regarding the CPM laser, and for his stubborn insistence on quality and honesty; without Matthew's help, little of the work presented in this thesis would ever have been done. I have also enjoyed many discussions with my classmate, Yasantha Rajakarunanayake, whose energy, enthusiasm, and optimism are a source of constant amazement and inspiration. I have enjoyed many discussions with Ed Yu, and am grateful for having had the benefit of his insight. I would particularly like to thank Ed for his role in the work presented in Chapter 2. I have enjoyed working with Jan Söderström during his brief time spent at Caltech, and would like to acknowledge his help in the work presented in Chapter 4. The exceptional efforts in MBE growth by Doug Collins during our collaboration on the work presented in Chapter 3 are greatly appreciated. I have also enjoyed

many discussions with Ed Croke, Mark Phillips, and Todd Rossi, and would like to acknowledge Todd's help with the autocorrelator described in Appendix A. I would like to acknowledge the encouragement of Dr. Alice Bonnefoi, who made my adjustment to Caltech much easier. It is a pleasure to acknowledge discussions with Drs. J.O. McCaldin, George Wu, Bob Hauenstein, Ted Woodward, and Wesley Boudville. I have also benefited from my contacts with Pete Zampardi, Yixin Liu, Johanes Schwenberg, Mike Wang, Ron Marquardt, Harold Levy, Rob Miles, and Tracey Fu. I would also like to thank all those who helped me by critical reading of this thesis; their efforts have greatly improved the content.

I would like to thank Marcia Hudson and Carol McCollum, for their excellent support on administrative matters, and for many interesting conversations. Vere Snell, whose professional and friendly manner helped shape the research group when I joined, is greatly missed.

I have also benefited greatly from my interactions with Dr. A. Yariv. I would like to acknowledge helpful conversations with Dr. Darryl Smith, of Los Alamos National Laboratory, and Dr. Ogden Marsh, of Hughes Research Laboratories. I would also like to acknowledge the tremendous help I received regarding the CPM laser from a number of people: Dr. Janis Valdmanis, of the University of Michigan, who gave very freely of his time to talk to me about the laser; Marcos Dantus and Bob Bowman at Caltech were also very helpful. The appendix on the CPM laser is largely a result of conversations with these people. I would also like to thank Dr. C.W. Nieh, of Caltech, for providing TEM data; Dr. J.-P. Faurie, of the University of Illinois, for providing CdTe/ZnTe superlattice samples; and Bobby Weikle for help with electron-beam evaporations.

During my time at Caltech I have enjoyed talking with Vicki Arriola, Jana Mercado, Laura Rodriguez, Ali Ghaffari, and Rosalie Rowe. I would also like to acknowledge the staff in all of the shops, stockrooms, and administrative capacities for making my stay at Caltech more enjoyable.

I would like to acknowledge financial support, in the form of fellowships, from the Natural Sciences and Engineering Research Council of Canada, and the California Institute of Technology.

Finally, I would like to thank Lionel Laroche, and Dr. Hal Zarem, for their friendship and support. I also owe thanks to Peter Leigh-Spencer, of Edmonton, who taught me about racing cars and, without realizing it, about doing experiments. I would like to thank my family for their unfailing encouragement and support; in particular, I would like to thank my parents for the high value they placed upon education. Finally, I would like to thank Tasha for her love and support; without her, I surely would have given this up long ago.

Abstract

This thesis describes experimental studies of semiconductor heterostructures, using optical techniques. The work presented concerns two topics in the study of semiconductor heterostructures: the escape of confined electrons and holes by tunneling, and the accomodation of lattice mismatch by strain. Time-resolved photoluminescence techniques have been used to measure the times required for electrons and holes to escape by tunneling through the AlAs barriers of GaAs/-AlAs/GaAs/AlAs/GaAs double barrier heterostructures. The effect of the indirect (X-point) levels in the AlAs barriers upon escape of confined electrons has been investigated using continuous (CW) photoluminescence. Time-resolved studies of electrically biased double-barrier heterostructures have been made, using both photoluminescence and photocurrent techniques. Finally, the accomodation of the large (6%) lattice mismatch in CdTe/ZnTe superlattices has been studied using Raman scattering.

In Chapter 2 we describe the measurement of tunneling escape times for electrons and holes confined in the quantum well of undoped GaAs/AlAs/GaAs/-AlAs/GaAs double-barrier heterostructures. Photoluminescence from carriers photoexcited in the quantum well by short optical pulses was used to study escape from the quantum well. By using the two-beam technique of photoluminescence excitation correlation spectroscopy (PECS), the first experimental measurements of the tunneling escape times for both the electrons and the holes were obtained. The tunneling escape times were seen to be exponentially dependent upon the barrier thickness for barriers between 16 and 34 Å. Escape times for both electrons and holes were found to be fast, and were as short as 12 ps in structures with 16 Å (6 monolayer) AlAs barriers. The rapid escape of heavy holes that was observed experimentally was in disagreement with simple calculations of the

heavy-hole tunneling escape times, which indicated that the heavy holes should escape on a time scale many orders of magnitude longer than the times observed experimentally. This drastic difference can be explained theoretically by considering a four-band model for holes in confined systems. For finite carrier densities and temperatures, mixing of the quantum well heavy hole levels with light hole levels, due to dispersion perpendicular to the growth direction, can explain the experimental observations. This observation that heavy holes can escape rapidly by tunneling is quite general, and is applicable to a wide variety of problems involving tunneling of holes in semiconductor heterostructures.

Chapter 3 describes a study of the effect of indirect (X-point) levels in the AlAs barriers on the tunneling escape of electrons in undoped GaAs/AlAs/GaAs/-AlAs/GaAs double-barrier heterostructures. The X-point levels, thought to be important in the electrical characteristics of double-barrier heterostructures, were found to affect the escape of photoexcited electrons in devices where the energy of the electron state confined in the GaAs quantum well is nearly equal to, or higher than, that of the X-point levels in the AlAs barriers.

In Chapter 4, we present time-resolved photoluminescence and photocurrent studies of tunneling in doped devices under electrical bias, in which current is flowing. Studies of the photoluminescence decay indicate that significant transport of photoexcited carriers from the electrodes into the quantum well occurs. This transport of photoexcited carriers constitutes a photocurrent, and the two-beam PECS technique for photoluminescence has been extended to a study of photocurrents in these devices. This technique may be useful for the study of tunneling in devices not amenable to photoluminescence techniques.

Chapter 5 describes a study of the accomodation of lattice mismatch in CdTe/-ZnTe strained layer superlattices. Using resonance Raman scattering, the energies of the ZnTe-like phonons were determined in a series of superlattices of varying average CdTe content. The ZnTe-like phonon energies decrease with increasing average CdTe content, indicative of the increasing strain of the ZnTe layers. The observed energies agree well with calculations of the strain shift of the phonons. The results indicate that the superlattice layers adopt a lattice constant independent of the buffer layer on which they are grown, and are coherently strained to a lattice constant that minimizes the strain energy of the superlattice.

Finally, the Appendix describes operation of the colliding pulse mode-locked (CPM) dye laser used in the time-resolved photoluminescence and photocurrent experiments. Alignment of the laser, and routine operation are documented.

List of Publications

Parts of this thesis have been, or will be, published under the following titles:

Chapter 2:

Electron Tunneling Time Measured by Photoluminescence Excitation Correlation Spectroscopy,
M.K. Jackson, M.B. Johnson, D.H. Chow, T.C. McGill, and C.W. Nieh, *Appl. Phys. Lett.* **54**, 552 (1989).

Electron Tunneling Time Measured by Photoluminescence Excitation Correlation Spectroscopy,
M.K. Jackson, M.B. Johnson, D.H. Chow, J. Söderström, T.C. McGill, and C.W. Nieh, in *Proceedings of the OSA Topical Meeting on Picosecond Electronics and Optoelectronics, Salt Lake City, Utah, March 8-10, 1989,* edited by T.C.L.G. Sollner and D.M. Bloom, p. 124.

Hole Tunneling Times in GaAs/AlAs Double Barrier Structures,
E.T. Yu, M.K. Jackson, and T.C. McGill, *Appl. Phys. Lett.* **55**, 744 (1989).

Chapter 3:

X-point tunneling in AlAs/GaAs double barrier heterostructures,
D.Z.-Y. Ting, M.K. Jackson, D.H. Chow, J.R. Söderström, D.A. Collins, and T.C. McGill, *Solid-State Electronics* **32**, 1513 (1989).

X-point Escape of Electrons from the Quantum Well of a Double-Barrier Heterostructure,

M.K. Jackson, D. Z.-Y. Ting, D.H. Chow, D.A. Collins, J.R. Söderström, and T.C. McGill, in preparation.

Chapter 4:

Time-Resolved Photoluminescence and Photocurrent Studies of GaAs/AlAs Double-Barrier Heterostructures,

M.K. Jackson, D.H. Chow, J.R. Söderström, and T.C. McGill, in preparation.

Chapter 5:

Raman Scattering Determination of Strain in CdTe/ZnTe Superlattices,

M.K. Jackson, R.H. Miles, T.C. McGill and J.P. Faurie, *Appl. Phys. Lett.* **55**, 786 (1989).

Contents

List of Figures

List of Tables

Chapter 1

Introduction

1.1 Introduction to Thesis

1.1.1 Overview

This thesis describes experimental studies of semiconductor heterostructures, using optical techniques. Recent advances in semiconductor epitaxial growth techniques have resulted in a wealth of new electrical, optical, and optoelectronic device applications, and have also allowed us to study a variety of fundamental issues in physics. The work described in this thesis concerns two major topics in the study of such semiconductor heterostructures: the time required for escape of confined electrons and holes by tunneling, and the accomodation of lattice mismatch by strain. The first part, concerning tunneling, describes studies of carriers confined in GaAs/AlAs/GaAs/AlAs/GaAs double-barrier heterostructures. Time-resolved photoluminescence techniques have been used to measure the times required for electrons and holes to escape by tunneling through the AlAs barriers. The tunneling time results have implications for high-speed devices based on tunneling of electrons or holes. The final chapter of the thesis describes a study of the accomodation of lattice mismatch in CdTe/ZnTe superlattices. The lattice mismatch between CdTe and ZnTe is large (6%) and makes the growth of these superlattices difficult. A series of these superlattices has been studied, using resonance Raman scattering; measurements of the phonon energies in these structures are used to determine the extent of accomodation of the lattice mismatch by strain in the layers composing the superlattice.

1.1.2 Summary of Results

One of the major results of this thesis is the measurement of tunneling escape times for electrons and holes confined in the quantum well of undoped GaAs/AlAs/GaAs/AlAs/GaAs double-barrier heterostructures. Photoluminescence from carriers photoexcited in the quantum well by short optical pulses was used to study escape from the quantum well. By using the two-beam technique of photoluminescence excitation correlation spectroscopy (PECS), the first experimental measurements of the tunneling escape times for both the electrons and the holes were obtained. The tunneling escape times were seen to be exponentially dependent upon the barrier thickness for barriers between 16 and 34 Å. Escape times for both electrons and holes were found to be fast, and were as short as 12 ps in structures with 16 Å (6 monolayer) AlAs barriers. The rapid escape of heavy holes that was observed experimentally was in disagreement with simple calculations of the heavy-hole tunneling escape times, which indicated that the heavy holes should escape on a time scale many orders of magnitude longer than the times observed experimentally. This drastic difference can be explained theoretically by considering a four-band model for holes in confined systems. For finite carrier densities and temperatures, mixing of the quantum well heavy hole levels with light hole levels, due to dispersion perpendicular to the growth direction, can explain the experimental observations. This observation that heavy holes can escape rapidly by tunneling is quite general, and should be applicable to a wide variety of problems involving tunneling of holes in semiconductor heterostructures.

This thesis also describes a study of the effect of indirect (X-point) levels in the AlAs barriers on the tunneling escape of electrons in undoped GaAs/AlAs/-GaAs/AlAs/GaAs double-barrier heterostructures. The X-point levels, thought to be important in the electrical characteristics of double-barrier heterostructures, were found to affect the escape of photoexcited electrons in devices where the energy of the electron state confined in the GaAs quantum well is nearly equal to, or higher than, that of the X-point levels in the AlAs barriers.

Photoluminescence studies of tunneling in undoped double barriers have also been extended to doped devices under electrical bias, in which current is flowing. Studies of the photoluminescence decay indicate that significant transport of photoexcited carriers from the electrodes into the quantum well occurs. This transport of photoexcited carriers constitutes a photocurrent, and the two-beam PECS technique for photoluminescence has been extended to a study of photocurrents in these devices. This technique may be useful for the study of tunneling in devices not amenable to photoluminescence techniques.

The final result described in this thesis is a study of the accomodation of lattice mismatch in CdTe/ZnTe strained layer superlattices. Using resonance Raman scattering, the energies of the ZnTe-like phonons were determined in a series of superlattices of varying average CdTe content. The ZnTe-like phonon energies decrease with increasing average CdTe content, indicative of the increasing strain of the ZnTe layers. The observed energies agree well with calculations of the strain shift of the phonons. The results indicate that the superlattice layers adopt a lattice constant independent of the buffer layer on which they are grown, and are coherently strained to a lattice constant that minimizes the strain energy of the superlattice.

1.1.3 Outline of Chapter

The purpose of Chapter 1 is to introduce the topics to be discussed in the remainder of the thesis, provide background information that will allow the results that will be presented to be viewed in the context of previous work in this field, and outline the rest of the thesis. Section 1.2 describes the motivation for our studies of semiconductor heterostructures; in particular, applications to high-speed devices, including background on studies of the characteristic time for tunneling, and applications of strained layer superlattices are discussed. In Section 1.3, experimental techniques applied to the study of tunneling times are described. Section 1.4 describes studies of strained layer superlattices using Raman scattering. Finally, Section 1.5 describes the organization of the remainder of the thesis.

1.2 Background and Motivation

1.2.1 Semiconductor Heterostructures

The ability to grow the semiconductor heterostructures studied in this thesis is based upon great advances in the last decade in epitaxial* growth techniques such as molecular beam epitaxy (MBE) and metalorganic chemical vapor deposition (MOCVD). The ability to grow epitaxial films with abrupt interfaces between different semiconductors has resulted in a huge variety of device applications,

---

*In the current context, epitaxial means that the film has a crystallographic structure related to that of the substrate.

some of which will be described in the following sections. These heterostructure systems also offer an ideal test of some of our conceptions of basic physics, in devices that can be studied in the laboratory. An example of such a topic is the time required for tunneling escape of confined electrons and holes, which can be studied in semiconductor heterostructure devices.

Epitaxial growth techniques have been used to grow a wide variety of semiconductor materials. Figure 1.1 shows the energy gap versus the lattice constant for a variety of III-V and II-VI zincblende semiconductors that have been grown with these techniques. Epitaxial growth techniques were first perfected for heterostructures composed of materials whose lattice constants are quite close, such as GaAs and AlAs. As can be seen in Figure 1.1, the lattice mismatch in the GaAs/AlAs system is a small fraction of a percent, which has greatly facilitated development of epitaxial growth techniques in this system. Largely as a consequence of the growth techniques being in a fairly advanced state of development, the GaAs/AlAs system has seen the greatest success in application to novel electronic, optical, and optoelectronic applications. The application of this material system to high-speed tunneling devices will be considered in Section 1.2.2.

In addition to the relatively small number of lattice-matched semiconductor systems, it is also possible to grow high quality strained heterostructures of materials with lattice mismatches as high as 7%. The freedom to combine a wider variety of materials greatly increases the possible heterostructure combinations, allowing a greater ability to tailor material properties. It is also possible to take advantage of the strain to control energy levels and nonlinear optical properties in ways not possible by other means [1, 2]. Recent advances in the understanding of the influence of growth conditions, such as substrate temperature, upon the formation of defects and the relaxation of strain [3], and demonstrations of long-lived InGaAs strained quantum well lasers [4] indicate that strained systems hold

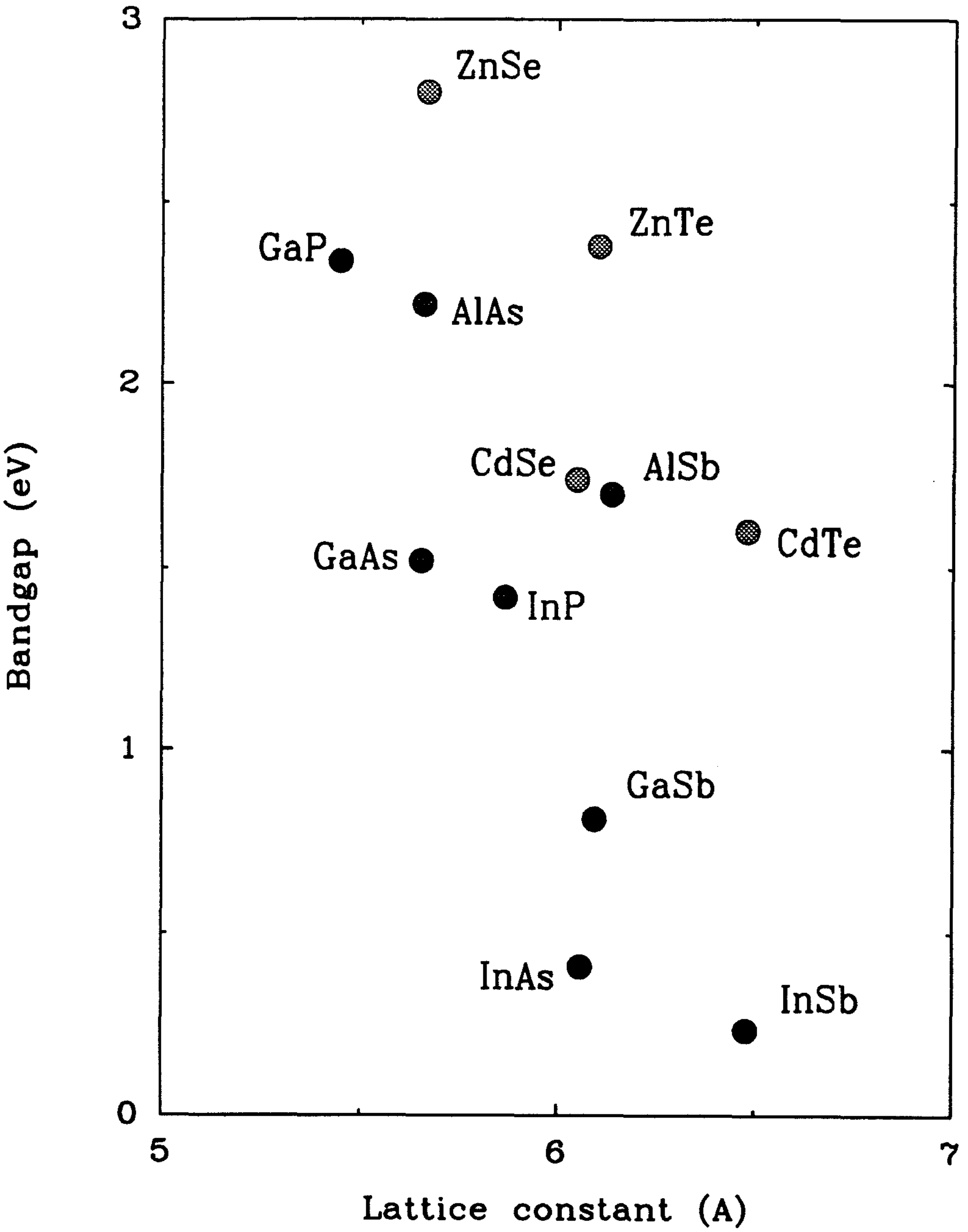

Figure 1.1: Energy gap at 4.2K versus lattice constant for some zincblende semiconductors. The dark shaded circles are III-V semiconductors, and the lighter shaded circles are II-VI semiconductors.

great promise for further development and device applications. Some specific applications of strained II-VI superlattices will be considered in Section 1.2.4.

1.2.2 Tunneling: High-Speed Device Applications

Solid-state devices based on tunneling have been of interest since the pioneering work of Esaki [5]. Tunnel diodes, also known as Esaki diodes, are based on homojunctions of heavily doped *p*-type and *n*-type materials such as GaAs. The essential feature of these devices is a current-voltage characteristic that shows an initial increase in current with increasing voltage, followed by a decreasing current with further increase in voltage. This region of decreasing current with increasing voltage, known as negative differential resistance (NDR), is of use in high frequency oscillators. By placing the device in a waveguide resonator and applying a voltage sufficient to bias the diode into the NDR region, oscillation can be sustained [6]. Early work on Esaki diodes, based on point contacts of zinc with heavily doped *n*-type GaAs, showed oscillation at frequencies up to 103 GHz [6]. One of the main reasons for interest in oscillators based on tunnel devices is that there are very few compact sources of radiation in the 100 to 1000 GHz frequency range. This frequency range is of interest for atmospheric monitoring [7], and for millimeter wave astronomy [8]. Sources of radiation in this region allow the use of heterodyne detectors, such as superconductor-insulator-superconductor (SIS) tunnel junctions, which are advantageous for narrow bandwidth operation in the millimeter wave region [9]. Sources based on multiplication of lower frequency Gunn oscillators have been demonstrated at up to 500 GHz [10], but there are few solid state devices capable of fundamental oscillation at such high frequencies. Devices based on tunneling present a possible solution to the lack of sources in this frequency range.

New concepts for tunnel devices based on heterostructure materials were proposed in 1973 by Tsu and Esaki [11] and have stimulated a resurgence of interest in this field. Figure 1.2 shows a diagram of the conduction band edge versus position for one such device, known as a double-barrier heterostructure. The device consists of two heavily doped electrodes surrounding the three layer region in the center. This central region consists of two thin layers of a large bandgap material, which act as barriers, surrounding a single thin layer of a smaller bandgap material. The electron states in the thin central region, called the quantum well, are affected by confinement of the electrons by the large bandgap barriers on the scale of their deBroglie wavelength. Typical quantum well widths are on the order of 50 Å and lead to to an increase in the lowest allowed energy for electrons in the quantum well on the order of 100 meV. The position of the lowest allowed energy level in the quantum well is indicated in Figure 1.2 by a dashed line. When electrical bias is applied to the device, the current increases, reaching a peak when the electrons in the negatively biased electrode are at an energy equal to that of the lowest electron state in the quantum well. At this bias condition, illustrated in Figure 1.2(b), the device is said to be at resonance. Further increase in the bias results in the electrons in the negatively biased region having an energy above that of the lowest quantum well state, and results in a decrease in the current. The region of decreased current past the resonance voltage is referred to as the valley, and negative differential resistance devices are often characterized in terms of their peak-to-valley current ratio. Further increase in bias past the valley eventually results in an increase in the current through the device due to nonresonant mechanisms, or transport through higher excited states in the quantum well.

Double-barrier heterostructure devices were first demonstrated in the GaAs/-/AlGaAs system by Chang et al. [12]. Subsequent development of this material

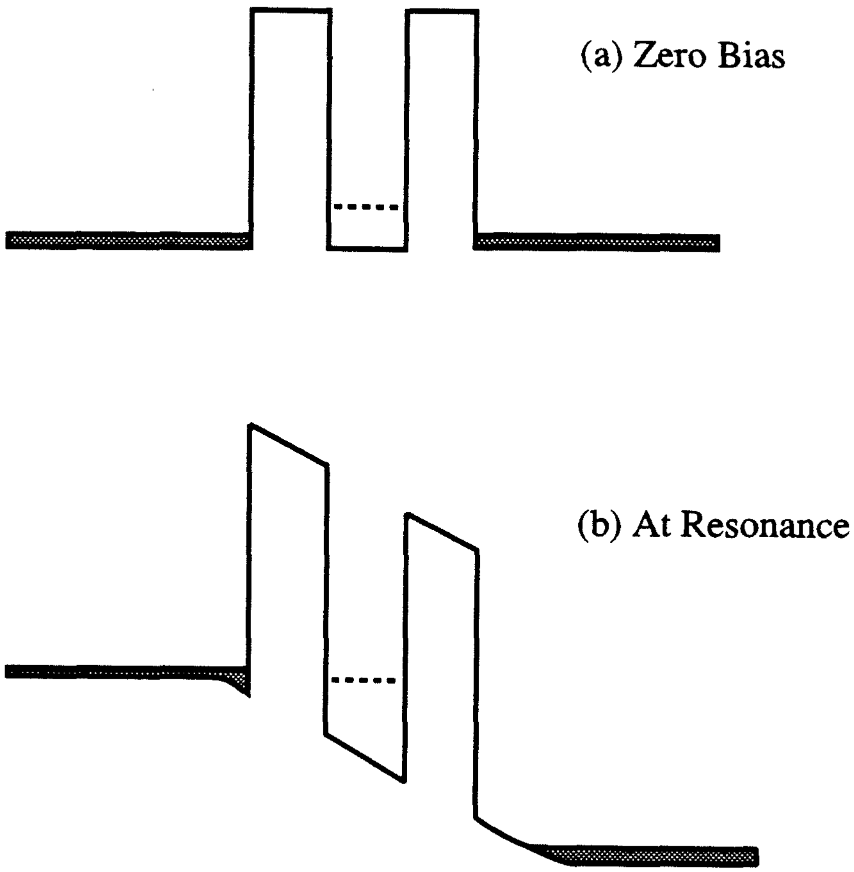

Figure 1.2: Conduction band versus position for a double-barrier heterostructure, (a) at zero bias, and (b) at resonance. The two outermost layers are doped n-type, indicated by the shaded region, and act as electrodes. The two large-bandgap layers act as barriers, and surround the quantum well in the center of the device. The dashed line in the quantum well indicates the energy of the lowest allowed electron state in the well.

system has progressed to the point where room temperature current densities can be as high as $1.3 \times 10^5 \mathrm{A/cm^2}$ in devices with peak-to-valley current ratios of approximately 2 [13]. Higher peak-to-valley current ratios are possible at the expense of decreased peak current density, and can be as high as 5.1:1 at room temperature for peak current densities of $10^4 \mathrm{A/cm^2}$ [14]. The high current density devices have been used in oscillators at frequencies as high as 420 GHz [15], and mixing action has been observed at frequencies up to 2.5 THz [16].

Recent efforts in this field have centered on the demonstration of double-barrier devices with superior performance, using other material systems. Working devices have been demonstrated in the InGaAs/GaAs/AlAs system [17], and the InAs/AlSb system [18]. The InAs/AlSb system shows the highest peak current densities observed to date, with maximum room temperature values of $4 \times 10^5 \mathrm{A/cm^2}$ and peak-to-valley current ratios of 4:1 [18, 19]. These devices have recently been demonstrated to oscillate at frequencies up to 675 GHz [19], and are predicted to be capable of oscillation at up to 1.3 THz.

This frequency of 675 GHz represents the highest frequency of fundamental oscillation for any solid-state device, and demonstrates very clearly the suitability of tunneling devices for high-frequency operation. Recent proposals and demonstrations of three-terminal tunnel structures [20, 21, 22, 23, 24, 25, 26] suggest that the high-frequency application of the two-terminal devices described above may be followed by three-terminal devices based on tunneling. These devices could have application in high-frequency analog or digital circuits, and may aid in the development of multilevel digital logic [21, 23].

Although high-frequency tunneling devices are affected by conventional considerations of stray capacitances and transit times across the depletion region, the ultimate speed of operation is expected to be limited by the tunneling time. Recently, Brown [27] has been able to quantify the dependence of the power output of the double-barrier oscillators on these three factors. The lifetime of electrons confined in the quantum well was found to be an important limitation on the output power of the oscillators at high frequency. The importance of the speed of tunneling to the performance of these devices has been a major motivation for the time-resolved studies of tunneling reported in this thesis.

1.2.3 The Characteristic Time for Tunneling

As discussed in the previous section, there is currently great technological interest in the speed of tunneling. There is, however, a more fundamental reason for the interest in the characteristic time for tunneling, related to our understanding of basic quantum mechanics. The question of the characteristic time for tunneling remains unanswered even after 50 years of study. As will be discussed in this section, there are many differing definitions of tunneling times; the measurements described in Chapter 2 are, strictly speaking, measurements of tunneling *escape* times. The relationships between the various tunneling times, and experiments intended to measure them, are not clear. It is not the purpose of the work in this thesis to attempt to resolve this issue; however, this section is intended as background to our study of tunneling escape times in double-barrier heterostructures. First discussed in 1931 by Condon [28], the time scale for the tunneling process has many important implications. For example, during tunneling, the motion of the electronic charge could be expected to cause polarization of the material through which the tunneling is occurring, or induce image charges in the surrounding electrodes. This image charge effect would be negligible if the time for tunneling were fast with respect to the time required for the electron plasma to respond (given by the plasma frequency). This issue is of current interest in the field of scanning tunneling microscopy (STM), in which the extent of the image charge effect on the tunneling current is thought to be important in understanding the results of STM experiments [29].

In this section, we will briefly outline the basic questions in this field, and try to give a feel for the origin of the controversy. The various competing theories for tunneling times have recently been reviewed by Collins et al. [30] and by Hauge and Støvneng [31]. In passing it is important to note that even these review articles are controversial, as seen by the comment [32] and reply [33] concerning Ref. [30]. The purpose of this section is not to duplicate these two extensive reviews, but to give a brief survey of the open questions in this area, and to suggest that the only satisfactory resolution of the debate will derive from comparison of the various theories with new experimental data. The reader interested in the details of the various theories, and the various arguments relating to their relative merit, is referred to Refs. [30, 31] and the references therein. The various experimental approaches to measurements of tunneling times will be discussed in Section 1.3.1, and the experimental results pertaining to tunneling obtained during the course of this thesis will be described in Chapters 2, 3, and 4.

The question which has generated so much debate, simply phrased, is: what is the time scale relevant for the tunneling of an electron from one side of a barrier to another? This situation is schematically illustrated in Fig. 1.3(a), which shows an electron tunneling across a single barrier. A related question, and one that is more directly addressed by the experiments in this thesis, is: what is the characteristic time for escape from a metastable state, and are there other time scales in addition to this escape time? This situation is illustrated in Fig. 1.3(b), in which an electron, initially confined in the quantum well of a double-barrier heterostructure, is shown tunneling through the barriers.

Thornber et al. [34], in their work on single-barrier tunneling (as illustrated in Fig. 1.3(a)), have suggested that there is a single time scale for the entire tun-

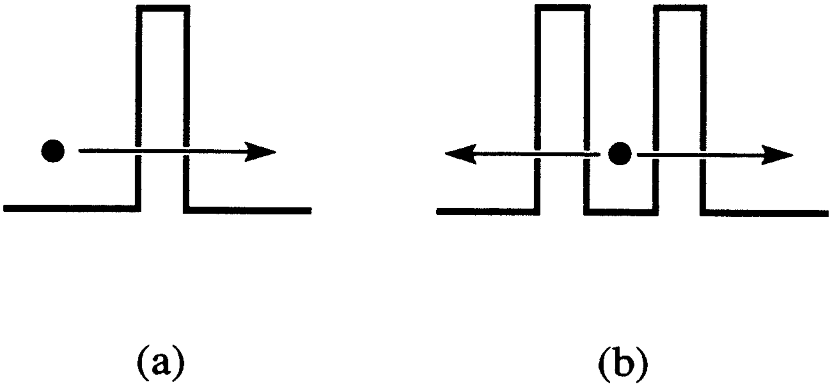

Figure 1.3: Schematic diagram of an electron (a) tunneling through a single barrier (b) escaping from the quantum well of a double-barrier heterostructure.

neling process, and that the relevant time is given by the inverse of the transition rate for incoming electrons to tunnel through the device. They argued that because the electron wavefunction in tunneling has a finite tail in the barrier during the entire process, that it was essentially interacting with the barrier during the entire time. Applied to the case of escape from a metastable state, illustrated in Fig. 1.3(b), this approach implies that the relevant time scale for the process is the quasi-bound state lifetime for the state in the quantum well.

In another approach, Büttiker and Landauer [35] have used semiclassical arguments to suggest that in single-barrier tunneling, as illustrated in Fig. 1.3(a), it is possible to define a traversal time for an electron to cross the barrier region, given by

$$\tau_{\mathrm{BL}} = \int_{x_1}^{x_2} \frac{m}{\hbar\,\kappa(x)} dx$$

where x_1 and x_2 define the classical turning points, and m is the mass. $\kappa(x) =$

$\sqrt{2m(V_0(x) - E)}/\hbar$ is the decay constant in the classically forbidden region, where $V_0(x)$ is the potential energy as a function of position, and E is the energy of the incoming electron. This time appears to be simply an integral of the distance divided by an effective velocity, where the standard expression for the velocity of a particle in a classically allowed region is extended to the forbidden region, ignoring the fact that such a velocity is imaginary. In the extension of this semi-classical approach to the escape from a metastable state illustrated in Fig. 1.3(b), it is claimed [36] that it is possible to separately and unambiguously identify a traversal time, related to the tunneling through the barrier, and that this time is different from the lifetime of the metastable state. This idea seems to imply that it is possible to identify a time at which a particle starts tunneling, and make some measurement of the time of interaction with the barrier starting when the particle "decides" to tunnel, and ending when the particle has completed tunneling. Although there is no obvious reason that this semiclassical approach is valid in the quantum mechanical problem, it has had some support in the results of some experiments regarding tunneling in single barriers and Josephson junctions, which will be briefly described in Section 1.3.1. Büttiker has suggested [37] that the photoluminescence decay measurements described in Chapter 2 of this thesis constitute measurements of the lifetime of the metastable state, but do not contain information regarding the traversal time.

As can be concluded from the above discussion, and from inspection of the other literature in which various workers have proposed tunneling times that are independent of the barrier thickness [38], or go to zero in the limit of zero incident kinetic energy [39], that there are a wide variety of procedures for calculating quantities in the tunneling problem that have the dimensions of time. The difficulty in defining and measuring a tunneling time originates in the fact that time is not an observable in quantum mechanics. The only procedure at our disposal is to follow the time evolution of other observable quantities, such as charge densities, and from the evolution of these quantities, infer information about the relevant time scale for tunneling. Nevertheless, the work in the last 50 years does not seem to have addressed this aspect of the problem seriously, i.e., the need to define the observables that can be measured experimentally. The original work of Condon [28] and MacColl [40] advocated the use of wave packets, in solutions of the time-dependent Schrödinger equation, as a method for making this connection. Their approach, which depends upon identification of the peak positions or the center of gravity of the wavepacket, has been criticized on the grounds that there is no physical basis for identification of the peak of the wavepacket [35]. On the other hand, the semiclassical approach advanced by Büttiker and Landauer, among others, clearly seeks to extend the results of classical mechanics to the quantum mechanical regime. Some of the impetus to pursue the semiclassical approach may derive from the fact that the quantum mechanical expression for the escape rate of a particle from a metastable state in a quantum well can be factored into an attempt frequency, and a transmission probability per attempt [41]. This picture of escape from a metastable state allows one to view the escape process as the motion of a particle back and forth between the classical turning points, with a small probability of transmission at each arrival at a turning point. When it is possible, as in this case, to view a quantum mechanical result in a semiclassical way, the semiclassical analogy often aids in forming an intuitively appealing understanding of the quantum mechanical process. There does not appear, however, to be any *a priori* justification for direct extension of classical concepts to the quantum mechanical regime.

In summary, attempts to identify a characteristic time for tunneling have been highly controversial, and difficult to verify experimentally. It would seem that the main problem in the theories is their inability to make the connection to experimentally verifiable quantities. Experimental techniques available for the measurement of tunneling times will be described in Section 1.3.1, and the results of time-resolved photoluminesce studies will be given in later chapters of this thesis.

1.2.4 Strained-Layer Superlattices

This section introduces the subject of strained II-VI superlattices, including their potential applications, and serves as background for the Raman scattering studies of CdTe/ZnTe superlattices that will be introduced in Section 1.4, and described in Chapter 5. Originally proposed by Esaki and Tsu [42] in 1970, superlattices have attracted a great deal of interest because of the ability to tailor the electrical and optical properties in ways not available with conventional bulk semiconductors. A superlattice consists of many thin layers of one semiconductor interleaved with thin layers of another semiconductor. A CdTe/ZnTe superlattice is schematically illustrated in Fig. 1.4. The alternating layer structure is typically repeated for many periods, to form a structure that is on the order of a micron thick, with individual layers carefully controlled in composition and thickness. The superlattice is grown on a thick substrate, and normally some form of buffer layer or layers is grown between the substrate and the superlattice. The buffer layer can serve several purposes: its most important function is to provide a clean, abrupt surface upon which to grow the superlattice. The buffer layer can also serve to force dislocations from the substrate to bend parallel to the surface of the buffer layer, and not propagate into the overlying film, thus providing a more perfect surface on which to grow the superlattice. The buffer may, in certain circumstances, be able to affect the lattice constant of the superlattice

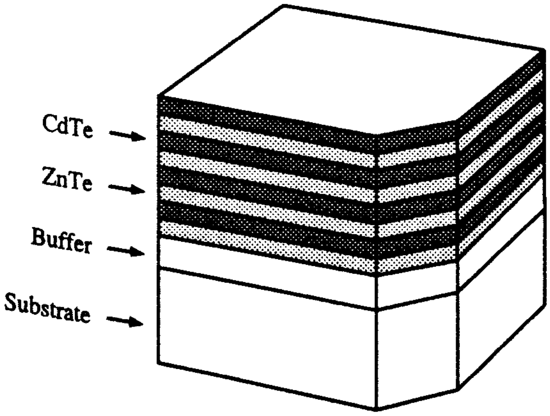

Figure 1.4: Schematic diagram of a CdTe/ZnTe superlattice. The superlattice consists of many repeated thin layers of CdTe and ZnTe, grown on top of a buffer layer which is deposited on a relatively thick substrate.

that is subsequently grown. In this case, the buffer layer is seen as a template for subsequent growth of the superlattice.

Superlattices were first studied in lattice-matched systems. However, as mentioned in Section 1.2.1, there has been great progress in the epitaxial growth of strained-layer structures. In 1983, Osbourn [43] suggested the growth of strained-layer superlattices, in which the lattice constants of the two materials are not exactly equal. The CdTe/ZnTe superlattice illustrated in Fig. 1.4 is a strained-layer superlattice; the lattice mismatch between CdTe and ZnTe is 6%. The greater variety of materials available once the constraint of close lattice match is removed allows growth of a large number of new heterostructures. Normally in such superlattices, it is desirable that the lattice mismatch be accomodated by elastic strain of the superlattice layers. Then, in addition to the increased variety of materials available, strain effects can be manipulated to produce changes in the electronic and optical properties that cannot be effected by other means, e.g., the strain-induced shifts and splittings of the electronic levels in a superlattice. This has recently been proposed [1] as a means of producing infrared detectors for the 8-12 μm region with InAs/$Ga_xIn_{1-x}Sb$ superlattices. In these superlattices, the strain allows the bandgap of the superlattice to be decreased while still allowing strong optical absorption [1]. Another example of the unique possibilities available with strain are the nonlinear optical properties of strained superlattices grown in the [111] direction. The strain fields in these superlattices result in electric fields in the superlattice layers through the piezoelectric effect, and are predicted to result in very strong nonlinear optical effects [2].

II-VI strained-layer superlattices are of interest for use as visible light emitters in the blue-green portion of the visible spectrum [44]. Although direct bandgap II-VI semiconductors with bandgaps in this spectral region exist, *p-n* junctions for light emitters have not been successfully fabricated. The main reason for this lack of success is due to the difficulties in doping wide-bandgap II-VI semiconductors. Although it is possible to dope these materials, there are none with wide bandgaps in which it is possible to dope both *n*-type and *p*-type to high densities [44]. The interest in II-VI superlattices is based on the fact that some materials can be doped heavily *n*-type, and some *p*-type. By combining a heterojunction of two materials, one of which can be doped *n*-type and one *p*-type, it has been proposed that it would be possible to make a *p-n* junction. CdTe and ZnTe are one such pair, where ZnTe can only be doped *p*-type, and CdTe can be doped *n*-type or *p*-type. Although the resulting superlattices have bandgaps in the red, they represent a system in which to study the issues that will be important in other wider-bandgap superlattices.

In strained superlattices, the lattice mismatch between the layers can be accomodated either by elastic strain or by the formation of strain-relieving defects. It is normally desired, for device quality and uniformity, that the lattice mismatch be accomodated entirely by uniform elastic strain. Such a structure is said to be coherently strained. One of the central problems in the study of strained superlattices is the determination of the extent to which lattice mismatch can be accommodated by strain of the layers. It has been observed in the growth of individual thin films on lattice-mismatched substrates that for film thicknesses below a value known as the critical thickness, lattice mismatch can be accomodated by elastic strain without the formation of significant densities of defects. Beyond this critical thickness, the effect of increasing film thickness is the formation of dislocations.

The same ideas of critical thickness that are applicable to growth of thin films also apply to strained layer superlattices, but the situation is slightly more complicated. In superlattices, there is a critical layer thickness, beyond which misfits will be formed at the interface between individual layers of the superlattice. The situations possible for the accomodation of mismatch between superlattice layers are schematically illustrated in Fig. 1.5. The unstrained bulk materials are shown in Fig. 1.5(a). In the superlattice, the mismatch may be accomodated entirely by elastic strain, as shown in (b), with the formation of a tetragonal unit cell. If the strain energies are too large, the situation in (c) results, in which misfit dislocations relieve the strain.

In superlattices, even for individual layer thicknesses below the critical layer thickness limit, there is another critical thickness related to the total thickness of the superlattice. If the superlattice has a free-standing lattice constant in the plane of the layers that is different from that of the buffer layer, and the total superlattice thickness is too great, dislocations will be formed at the interface between the superlattice and the buffer layer, and in the first superlattice layers. Below this critical superlattice thickness, the superlattice will adopt a lattice constant equal to that of the buffer on which it is grown. The two possible situations

(a) Unstrained bulk materials

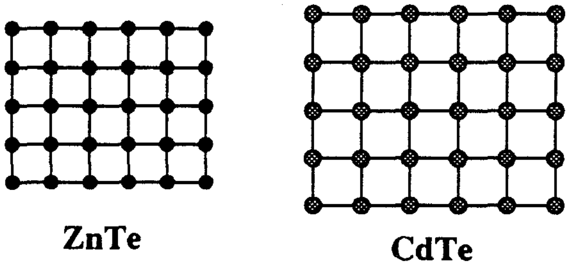

(b) Coherently strained layers

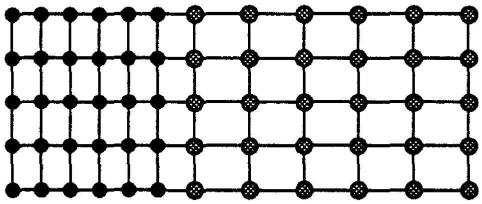

(c) Unstrained layers, with misfits

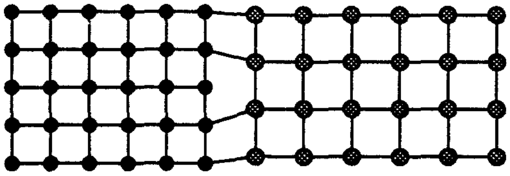

Figure 1.5: Schematic illustration of accomodation of lattice mismatch in superlattice layers. (a) The unstrained bulk materials. (b) Coherently strained layers, in which lattice mismatch is accomodated by elastic strain. (c) Unstrained layers, with misfit dislocations at the interface. The difference between the lattice constants of the two materials has been exaggerated for clarity.

for total superlattice thicknesses, i.e., below and above the critical thickness, are illustrated in Figs. 1.6 (a) and (b), respectively. The superlattice shown in Fig. 1.6(a) is coherently strained to the buffer layer. In the case illustrated in Fig. 1.6(b), a network of dislocations has relieved the strain near the buffer layer, and the superlattice has adopted an in-plane lattice constant different from that of the substrate. Experimental studies of a number of materials systems have indicated that the portion of the superlattice beyond the dislocation network can adopt a uniform lattice constant that minimizes the strain energy of the superlattice. This configuration is referred to as a free-standing superlattice, because the superlattice adopts a lattice constant that is essentially independent of the buffer layer on which it is grown.

The experimental techniques used to resolve these issues related to the accomodation of lattice mismatch will briefly be described in Section 1.4. Progress in the characterization of strained layer superlattices will be essential in the development of the growth techniques for such systems, and will be important in the eventual use of strained-layer superlattices in practical applications.

1.3 Experimental Studies of Tunneling Times

In this section we will introduce the subject of experimental studies of tunneling times. Section 1.3.1 is devoted to a brief review of the experimental techniques available for such studies. The following sections then describe the three problems related to tunneling times in GaAs/AlAs double-barrier heterostructures studied in this thesis. Section 1.3.2 introduces the time-resolved photoluminescence measurements of tunneling times in undoped double-barrier heterostructures that will be presented in Chapter 2. Section 1.3.3 discusses the use of continuous wave (CW) photoluminescence in the study of the effect of the X-point on the escape

(a) superlattice coherently strained to buffer

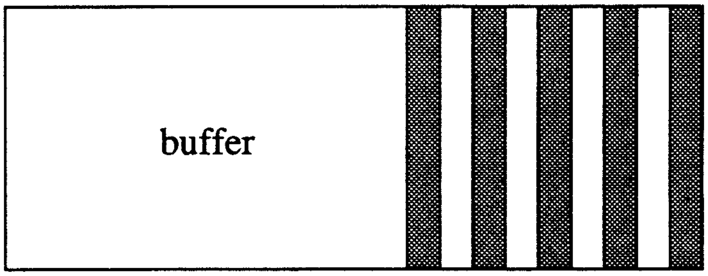

(b) free-standing superlattice

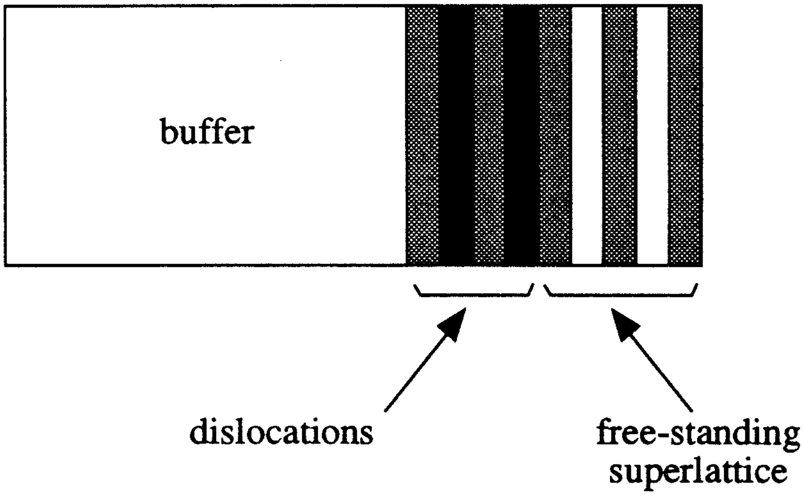

Figure 1.6: Superlattices with total thickness below and above the critical thickness. (a) Below critical thickness the superlattice is coherently strained to the buffer layer. (b) Beyond the critical thickness, a network of dislocations forms at the buffer layer-superlattice interface, and the superlattice adopts a free-standing lattice constant (independent of the buffer layer). Superlattice layers near the interface with the buffer are dislocated to accomodate the lattice mismatch.

of electrons from the quantum well, serving as an introduction to the work that will be described in Chapter 3. Finally Section 1.3.4 introduces the use of time-resolved photoluminescence and time-resolved correlation photocurrent studies of biased double-barrier heterostructures, which will be described in Chapter 4.

1.3.1 Techniques for Studies of Tunneling Times

In this section we will give an overview of the experimental techniques that can be used for studies of tunneling times. The techniques to be discussed are mostly based on the use of ultrafast optical pulses from mode-locked lasers. Generation of these optical pulses will not be discussed here, but will be described in Appendix A. The techniques based on optical methods are divided into three main categories: electrooptic sampling, photoluminescence, and photocurrent. At the end of this section, low-frequency electrical studies applied to the measurement of tunneling times are described, and finally there is a brief mention of other techniques that have been proposed, but have not yet been demonstrated for the study of tunneling times.

The first experimental technique to be described is that of electrooptic sampling. This technique, pioneered by Valdmanis et al. [45], takes advantage of the electrooptic effect, in which an electric field in certain materials affects the index of refraction. In this technique, an electrical device such as a double-barrier heterostructure is mounted in a stripline environment, where at least part of the stripline is fabricated on an electrooptic substrate. Ultrafast electrical pulses, generated by illumination of a photoconductive circuit element [46, 47], can be introduced onto the stripline and allowed to interact with the device. The signals propagating at later times can be determined by measuring the polarization change of a suitably delayed optical pulse transmitted through the electrooptic material next to the stripline conductor. Since the change of polarization is proportional to the electric field, the voltage on the stripline can be determined as a function of time by varying the delay of the sampling pulse with respect to the pulse used to generate the initial electrical pulse. This technique has been applied to the study of GaAs/AlAs double-barrier heterostructures by Whitaker and coworkers [48], and more recently by Diamond et al. [49]. These studies require the devices to be in a stripline environment, where they are susceptible to stray capacitances and other effects unrelated to tunneling. As such, they represent appropriate measurements of devices intended for practical application, but may not be the best way to measure the ultimate speed of the tunneling process.

The second main technique to be described is that of photoluminescence (PL), which can be divided into three different approaches: conventional continuous wave (CW) PL, direct time-resolved PL, and photoluminescence excitation correlation spectroscopy (PECS). Photoluminescence is the study of the photons emitted by recombining electron-hole pairs that are created by photoexcitation. The ability to use PL to obtain information regarding the electron and hole populations derives from the fact that free-carrier photoluminescence is proportional to the density of electrons and holes, i.e.,

$$I_{PL}(t) = B\,n(t)\,p(t) \tag{1.1}$$

where B is a constant, characteristic of the material. In CW photoluminescence, a CW laser is used to excite electron-hole pairs above the bandgap. The carriers created quickly thermalize to the lowest electron and hole states. These carriers can then recombine and emit photons, which are detected and integrated over time. If the carriers can also tunnel to other states not detected in the PL experiment, then the densities of the recombining carriers are reduced, and so is the PL signal. Thus, the intensity of the CW PL signal is a measure of the tunneling decay times, or in general, the nonradiative decay times, relative to the recombination time. This technique as applied to the study of the effect of indirect levels in the AlAs barriers of GaAs/AlAs double-barrier heterostructures will be introduced in Section 1.3.3, and the results of such a study will be described in Chapter 3.

The second main photoluminescence technique requires the use of ultrafast pulses from a mode-locked laser. Since the PL signal is described by Eq. 1.1 above, the decay of the populations can be probed if the photoluminescence signal can be monitored as a function of time. In such experiments, a single ultrafast optical pulse is used to excite electron-hole pairs on a time scale short with respect to the tunneling process of interest. Then the PL signal is directly monitored by a streak camera [50], microchannel plate photomultiplier tube [51], parametric upconversion [52], or Kerr effect gating [53]. These techniques have been applied to the study of tunneling by Deveaud [54], Tsuchiya [55], and others. The direct detection technique suffers from the problem, apparent in Eq. 1.1, that it is the product of the electron and hole densities that governs the evolution of the PL signal. Therefore, if the PL signal decays, it is impossible to discern which population decrease was responsible for the decay, and thus which tunneling time is being observed. If the responses of the populations $n(t)$ and $p(t)$ are dominated by tunneling, with exponential decay times τ_e and τ_h, respectively, then the PL signal of Eq. 1.1 is seen to decay according to

$$I_{PL}(t) = B\, n_0\, p_0 \, \exp\left[-t\left(\frac{1}{\tau_e}+\frac{1}{\tau_h}\right)\right]$$

where n_0 and p_0 are the initial carrier densities created by photoexcitation, and are presumably equal. The above equation clearly shows that it is the reduced time $(1/\tau_e + 1/\tau_h)^{-1}$ that is observed. This inability to distinguish between the decay of electron and hole carrier densities led to misinterpretation of early studies of tunneling in GaAs/AlAs double-barrier heterostructures. The experimental observations that revealed this oversight are described in Chapter 2 of this thesis, and required the use of the PECS technique that will be described next.

The third photoluminescence technique available in addition to the CW and direct time-resolved techniques already described is photoluminescence excitation correlation spectroscopy (PECS). This technique, originated by von der Linde [56], will be described in detail in Section 2.2. Here we will give only a very brief description of the principle. PECS is a form of pump-probe technique, in which the response to photoexcitation by two optical pulses, delayed with respect to one another by time γ, is measured using synchronous detection techniques. The PL signal detected in this experiment depends on the delay γ, and is given by

$$I_{PL}^{\mathrm{PECS}}(t) = a\left[\exp\left(-\frac{|\gamma|}{\tau_e}\right) + \exp\left(-\frac{|\gamma|}{\tau_h}\right)\right] \tag{2}$$

The power of the PECS technique is evident in the above equation: the signal is the sum of two equal amplitude exponentials, containing the two individually recoverable time constants. If, for example, the hole time τ_h is much longer than the delay times γ accessed experimentally, then the signal will be proportional to $1 + \exp(-|\gamma|/\tau_e)$. This technique allowed the measurements of both electron and hole tunneling escape times described in Chapter 2.

The third main experimental technique for the direct determination of tunneling times involves time-resolved measurements of photocurrents. Conventional time-resolved photocurrent techniques are similar to the direct time-resolved PL techniques described above. In a time-resolved photocurrent experiment, an ultrafast optical pulse excites electron-hole pairs, and the subsequent behavior of the photocurrent signal is measured as a function of time. This technique has been applied to the study of tunneling times [57, 58], but has been limited to times on the order of nanoseconds. A new time-resolved photocurrent technique analogous to the PECS photoluminescence described above will be presented in Chapter 4. Using photoexcitation by two optical pulses, and recovering the time-averaged photocurrent as a function of relative delay γ, measurements of times related to the tunneling of photoexcited carriers may be observable. This techique is very new, and the details of its interpretation are still quite uncertain. However, it holds promise as a technique for study of structures not amenable to study with other techniques such as photoluminescence.

We will now discuss a very different group of experimental techniques for the study of tunneling times, based upon low frequency electrical measurements of tunneling currents. Instead of direct measurement of tunneling times, these techniques rely on the use of time scales for processes unrelated to tunneling, such as the plasma frequency, as a sort of clock for the study of tunneling. Although somewhat indirect, they represent an important approach to the experimental study of tunneling times. Because of space limitations, these techniques, represented by the work of Guéret [59, 60] and Esteve [61] will not all be described in detail. One representative experiment, that of Ref. [60] will be described, and the interested reader is referred to Refs. [59] and [61] for discussions of the other approaches. Guéret [60] studied single-barrier tunneling in a wide range of GaAs/$\mathrm{Al}_x\mathrm{Ga}_{1-x}$As/GaAs single barriers. For thin barriers, the measured tunneling current could be accurately calculated by a theory neglecting any image charge effects from the n-type electrodes. For thicker barriers, however, significant deviations from this theory were observed, and were attributed to dynamic rearrangement of the electron plasma in the electrodes during the course of tunneling. The crossover between the two regions was found to be characterized by the product $\omega_{\mathrm{P}}\tau_{\mathrm{BL}} \approx 3$, where ω_{P} is the plasma frequency for the electron density in the electrodes, and τ_{BL} is the Büttiker-Landauer traversal time described in Section 1.2.3. In this experiment, the inverse of the plasma frequency, a known quantity, is used as a reference against which to measure the tunneling time. Other similar approaches have used the cyclotron frequency for an electron in a magnetic field [59], and the propagation delay along a stripline [61]. Although these low frequency techniques provide valuable information regarding tunneling times, they are quite indirect, and rely upon theories describing the effect upon tunneling of other unrelated processes. In view of the great variety of contradictory theories concerning the simple question of the characteristic time for tunneling, it would seem somewhat risky to rely on these more complicated theories to provide evidence on the subject of tunneling times.

Finally, we will briefly discuss some techniques that have not yet been demonstrated, but that hold potential for application to the study of tunneling times. Cutler et al. have proposed the use of a scanning tunneling microscope to measure a tunneling time [62]. Another technique that could be applied to measurements of tunneling times is active-layer photomixing [63]. Developed for study of the frequency response of laser diodes, the photomixing technique relies on the interference of two CW lasers to provide a perturbation of the electron-hole density in a semiconductor at the difference frequency $\delta\omega = \omega_1 - \omega_2$. If the lasers are relatively close in frequency, and stable, difference frequencies in the GHz to THz range can be obtained. It may be possible to use such a technique to study the devices described in Chapter 4, in which optical excitation can be used in devices that show negative differential resisistance. The DC photocurrent may show features as a function of the difference frequency related to the response time of the device. Finally, the technique of phase-space absorption quenching [64], based on the decrease of absorption caused by Fermi-filling of electron and hole bands, may be useful for future studies of tunneling times.

In summary, there are several experimental techniques that can be used for studies of tunneling times. The technique of electrooptic sampling has the advantage of being quite direct, but is sensitive to all of the considerations such as stray capacitances, etc., that limit the speed of a tunneling device, in addition to the tunneling time of interest. Photoluminescence techniques, including CW, direct time-resolved, and the two-beam technique of photoluminescence excitation correlation spectroscopy (PECS), can be used, and PECS measures the decay of both electron and hole populations. Time-resolved photocurrent techniques can be used, including a recently developed extension of the PECS photoluminescence technique to the study of photocurrents. Finally, low frequency measurements of tunneling currents in single barriers and Josephson junctions have been used to make indirect measurements of tunneling times. Other experimental techniques, using scanning tunneling microscopes, active layer photomixing, and phase space absorption quenching may lead to development of new methods by which to measure tunneling times.

1.3.2 Tunneling Time Measurements in Undoped Double-Barrier Heterostructures

The first measurements of tunneling escape times in GaAs/AlAs double-barrier heterostructures were performed by Tsuchiya et al. using direct time-resolved photoluminescence [55]. The samples studied were a series of undoped GaAs/AlAs/GaAs/AlAs/GaAs heterostructures in which the final GaAs cap layer thickness was 300 Å.

This work was followed by our study, to be described in Chapter 2, of similar samples using the photoluminescence excitation correlation (PECS) technique. The experimental measurements of the electron and hole escape times obtained constitute one of the most important results presented in this thesis. The tunneling escape times for electrons and holes were found to be very similar, and are plotted in Fig. 1.7 as a function of the AlAs barrier thickness. The exponential dependence of the observed decay time on barrier thickness for barriers ranging from 16 to 34 Å is indicative of tunneling escape, which occurs on a time scale as short as 12 ps in the fastest sample measured. The experimental techniques used, and the interpretation of these results, will be presented in Chapter 2.

1.3.3 X-point Escape of Electrons

Many of the tunneling properties of heterostructures can be understood simply by characterizing each of the constituent materials by a potential energy and an effective mass. However, in certain situations it is important to account for a more detailed picture of the band structure of the materials. One such situation is related to the indirect nature of the AlAs material used as the barrier material in many double-barrier heterostructure devices. The minimum energy for electrons in the conduction band in AlAs occurs not at the zone center, but in the [001] direction at or near the edge of the Brillouin zone. This point in the zone, known as the X-point, is thought to be important in the valley currents in GaAs/AlAs double-barrier heterostructures [65], and limits room temperature peak-to-valley current ratios to a maximum of approximately 5:1. Chapter 3 describes a study of the effect of the X-point in such devices. A series of GaAs/AlAs/GaAs/AlAs/-GaAs heterostructures with varying well thickness was studied. For wide wells, the quantum well state lies lower in energy than the X-point levels in the barriers. By decreasing the well thickness, and thereby increasing the confinement energy, the quantum well state can be raised in energy until it is above the X-point levels in the barriers. By studying CW photoluminescence in these structures, evidence for rapid escape of electrons via the X-point was obtained. This study will be described in detail in Chapter 3.

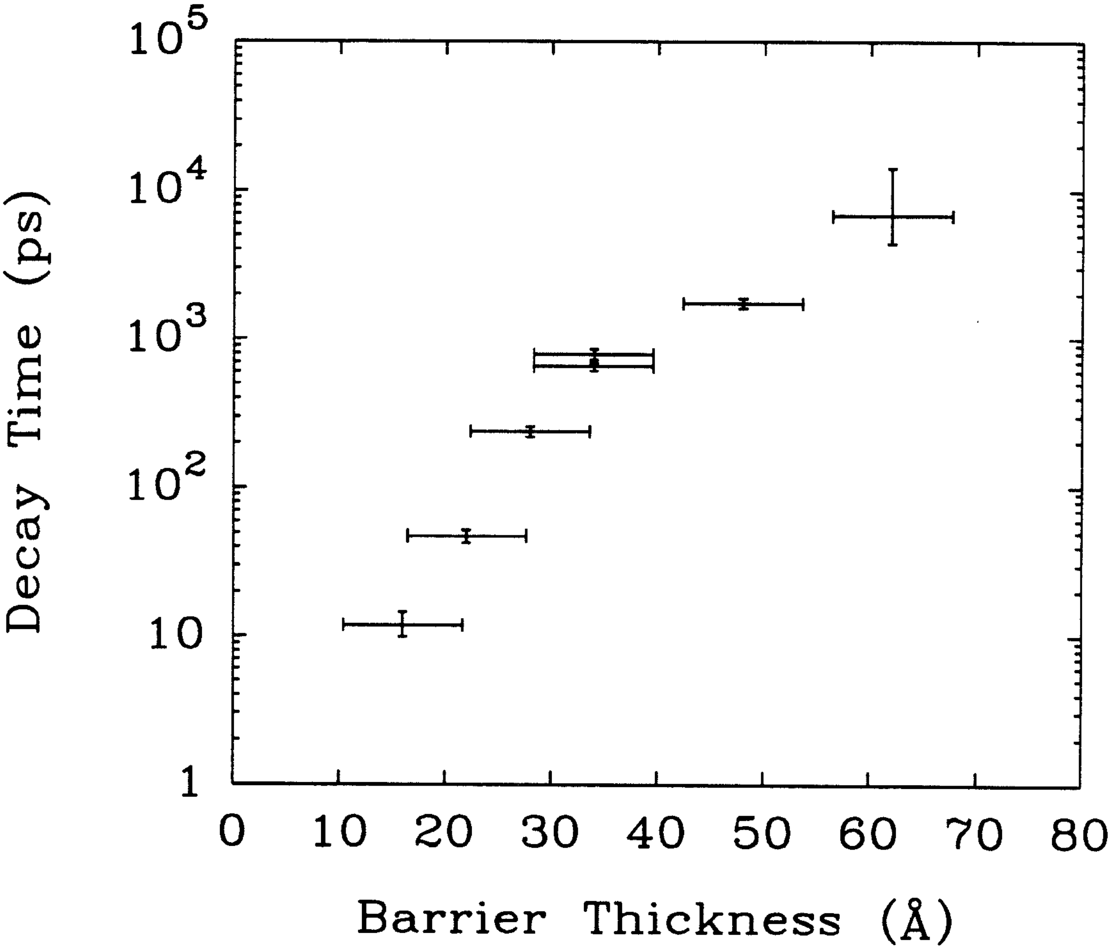

Figure 1.7: Experimentally observed tunneling escape time in GaAs/AlAs/-GaAs/AlAs/GaAs heterostructures. The escape time for electrons and heavy holes is very similar, and is plotted as a function of the barrier thickness.

1.3.4 Tunneling in Biased Structures

The time-resolved studies of tunneling described in Sections 1.3.2 and 1.3.3 were performed in the absence of electric fields in the devices. Since the double-barrier devices are electrically biased during operation, it is desirable to make measurements of tunneling times in the presence of electric fields. Norris et al. [66] have used direct time-resolved photoluminescence in biased heterostructures, in which their device was embedded in a $p-i-n$ structure. Although this allowed the application of an electric field, the device studied did not show negative differential resistance. The only studies of tunneling times in working negative differential resistance devices were made using electrooptic sampling [48, 49].

The work described in Chapter 4 concerns studies of operational double-barrier heterostructures. Structures were fabricated with thin electrodes on the surface side of the device, and either thin gold contacts, or annular contacts were made. The devices showed negative differential resistance, while simultaneously allowing photoexcitation of the quantum well and observation of the photoluminescence from the quantum well. These devices were studied, using the PECS time-resolved photoluminescence technique. Evidence from the photoluminescence measurements indicated that study of photocurrents in these devices using techniques analagous to the PECS PL technique could prove interesting. Results of these studies will be described in Chapter 4.

1.4 Raman Scattering Studies of Strained-Layer Superlattices

As described in Section 1.2.4, one of the central issues in the study of strained-layer superlattices is the determination of the extent to which lattice mismatch is accomodated by elastic strain. This section begins with a brief description of experimental techniques that can be used to determine strain, and then describes the use of Raman scattering for this purpose in the study of strained-layer superlattices.

Several techniques can be used to make experimental determinations of strain in superlattices, each having different advantages. One of the simplest techniques is that of photoluminescence (PL), which gives information about the lowest electronic levels in the superlattices, which are sensitive to strain. Unfortunately, the interpretation of PL data is complicated by the fact that the electronic energies are also affected by confinement, and the extent of confinement is strongly affected by the values of the band offset* between the two materials composing the superlattice. Unfortunately the values of band offsets are difficult to measure, and are not known very precisely. An additional complication in PL is that the effects of strain and confinement can produce opposite effects of similar magnitude, and it can be impossible with certain choices of sample parameters to determine the difference between strained and unstrained structures. Another powerful technique that has been used to determine the accomodation of strain is x-ray scattering. This technique can measure the lattice constant of the superlattice to great accuracy. An experimental complication is that x-ray scattering probes a depth on the order of $10\,\mu\text{m}$. Since typical superlattice and buffer layer thicknesses are on the order of a few microns, signals from all of the buffer layers and the substrate are observed, which can complicate the interpretation of x-ray data.

A complementary technique for the determination of strain in superlattices, and the one used for the CdTe/ZnTe superlattices studied in this thesis, is Raman

---

*The change in the energy of the valence band edge in traversing a heterointerface of one material with another is known as the valence band offset.

scattering. First predicted in 1923 by Smekal, and observed by Sir C.V. Raman in 1928, Raman scattering is the inelastic scattering of photons by excitations in the material being studied. Experimentally, photons, typically from a laser, are incident upon the sample to be studied, and the scattered light is collected and spectrally resolved. In addition to a very large signal at the exciting laser energy, scattered photons with energies equal to the exciting laser energy plus or minus the energy of the excitation being studied can be seen, corresponding to the absorption (anti-Stokes process) or emission (Stokes process) of a quantum of the excitation. Higher order processes are also possible, in which several potentially different excitations can be simultaneously excited or absorbed. In semiconductor superlattices, the excitations most often studied possible include electronic, and vibrational (phonon) modes.

In the study described in Chapter 5, the energies of the longitudinal optical phonons in the superlattices will be studied. Fig. 1.8 shows a typical Raman scattering scan for a CdTe/ZnTe superlattice. The intensity of the scattered light is shown as a function of the energy loss from the exciting laser. Because the energy shifts from the exciting laser are typically quite small, the energy loss in Raman studies have historically been shown in units of wavenumbers, or inverse centimeters, a convention that will be followed in this thesis.[†] The scan shown in Fig. 1.8 shows three main phonon features near 200, 400, and 600 cm^{-1}, corresponding to one, two, and three phonon scattering. The structure of the phonon peaks indicates that more than one particular phonon is involved in the process. The laser energy for this scan was just above the bandgap of the superlattice, and the rising edge at the highest energy losses seen in Fig. 1.8 is the beginning of the photoluminescence signal, which is much larger than the

---

[†] The wavenumber k for a photon of wavelength λ is defined as $k = 1/\lambda$. The conversion to energy units is $1\,\mathrm{cm}^{-1} \approx 0.124\,\mathrm{meV}$.

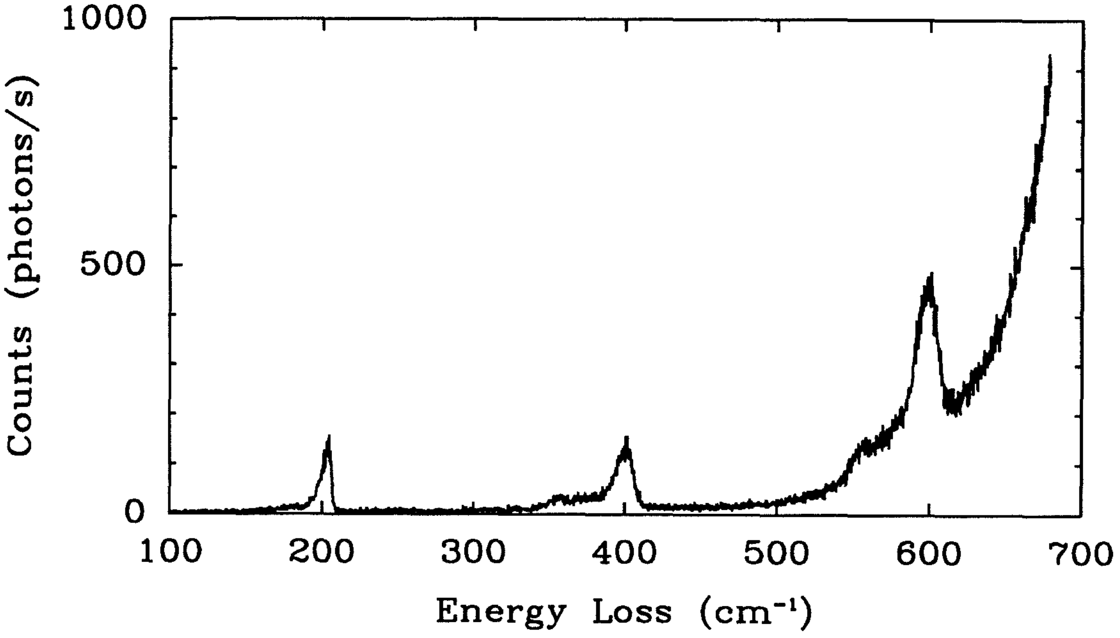

Figure 1.8: Typical Raman scattering spectrum at 5K for a CdTe/ZnTe superlattice with 26 Å CdTe and 32 Å ZnTe layers, collected in the backscattering geometry. Scattering from one, two, or three phonons can be seen, near 200, 400, and 600 cm^{-1}, respectively. Structure in the various phonon peaks indicates that several different phonons are involved. The rising edge at high energy loss is the onset of the photoluminescence signal, visible because the laser energy for this scan was just above the bandgap.

Raman signal. Because the signals observed in Raman scattering are very weak, and must be detected with energy resolution on the order of 0.1 meV at energies on the order of 1.5 eV in the presence of huge signals from scattered laser light, the experimental difficulties in completing these studies are considerable. The experimental considerations for such experiments will be described in Section 5.3.

In order to use measurements of phonon energies to determine strain in superlattices, it is necessary to consider the effect of strain upon the phonon energies. This topic will be considered in detail in Section 5.5, where calculations of the phonon energies in CdTe/ZnTe superlattices will be described.

1.5 Outline of Thesis

Chapters 2, 3, and 4, describe experimental studies of tunneling times in GaAs/AlAs double-barrier heterostructures. Chapter 2 describes a study, using time-resolved photoluminescence, of the times required for carriers confined in the quantum well of GaAs/AlAs/GaAs/AlAs/GaAs heterostructures to escape by tunneling through the AlAs barriers. The theoretical analysis of the two-beam photoluminescence excitation correlation spectroscopy (PECS) technique used in these measurements is discussed, incorporating numerical solutions that extend previous analyses of limiting cases to a much more general situation, more appropriate to the experimental conditions. The experimental study of the dependence of the tunneling escape times for electrons and holes upon the thickness of the AlAs barriers is then described. The surprising experimental result that heavy holes escape much more rapidly than initially expected is explained in terms of the mixing of light- and heavy-hole bands in the quantum well, important for the understanding of experiments necessarily conducted at finite temperature and with finite photoexcited carrier densities.

Chapter 3 describes a study of the effect of indirect X-point levels on the escape of electrons from the quantum well. A series of undoped double-barrier heterostructures with varying quantum well widths was studied using conventional photoluminescence. The results of a study of the dependence of the photoluminescence intensity upon the position of the quantum well energy level relative to the X-point levels in the barriers is described, and used to determine the effect of the X-point levels on the escape of electrons.

Chapter 4 describes the study of time-resolved photoluminescence and photocurrents in biased double-barrier heterostructures. A description is given of the preparation of devices that show negative differential resistance, while simultaneously allowing the photoexcitation of carriers in the quantum well and collection of the photoluminescence. Results of photoluminescence decay studies of these structures while under bias are shown, indicating that investigations of the photocurrents flowing in these biased devices could prove interesting. A technique for time-resolved photocurrent, analagous to the PECS time-resolved photoluminescence technique, is described. Time-resolved photocurrent results for three double-barrier heterostructures are presented.

Chapter 5 addresses the accomodation of lattice mismatch in strained CdTe/-ZnTe superlattices, and describes a resonance Raman scattering study of four superlattices. The dependence of the observed phonon energies upon the composition of the superlattice is investigated. The experimental results are compared with various theories of the accomodation of lattice mismatch in this system, and used to determine the distribution of strain in the superlattice layers.

Appendix A contains a description of the colliding pulse mode-locked (CPM) dye laser used in the time-resolved experiments described in this thesis. Modifications to the laser undertaken during the course of this work are described, along with descriptions of the design considerations and motivations for these changes. Routine operation and characterization of the performance of the laser is also described.

References

[1] D.L. Smith and C. Mailhiot, *J. Appl. Phys.* **62**, 2545 (1987).

[2] D.L. Smith and C. Mailhiot, *Phys. Rev. Lett.* **58**, 1264 (1987).

[3] R.H. Miles, T.C. McGill, P.P. Chow, D.C. Johnson, R.J. Hauenstein, C.W. Nieh, and M.D. Strathman, *Appl. Phys. Lett.* **52**, 916 (1988).

[4] S.E. Fischer, R.G. Waters, D. Fekete, J.M. Ballantyne, Y.C. Chen, and B.A. Soltz, *Appl. Phys. Lett.* **54**, 1862 (1989).

[5] L. Esaki, *Phys. Rev.* **109**, 603 (1958).

[6] C.A. Burrus, *Proceedings of the IRE* **48**, 2024 (1960).

[7] E. Altshuler, in *Infrared and Millimeter Waves, Vol. 9*, K.J. Button, ed. (Academic, New York, 1983), Chapter 4.

[8] J.W.M. Baars, in *Infrared and Millimeter Waves, Vol. 9*, K.J. Button, ed. (Academic, New York, 1983), Chapter 5.

[9] P.L. Richards and L.T. Greenberg, in *Infrared and Millimeter Waves, Vol. 6*, K.J. Button, ed. (Academic, New York, 1982), Chapter 3.

[10] N. Erickson, *1990 IEEE MTT-S International Microwave Symposium Digest, Vol. III*, 1301 (1990).

[11] R. Tsu and L. Esaki, *Appl. Phys. Lett.* **22**, 562 (1973).

[12] L.L. Chang, L. Esaki, and R. Tsu, *Appl. Phys. Lett.* **24**, 593 (1974).

[13] S.K. Diamond, E. Özbay, M.J.W. Rodwell, D.M. Bloom, Y.C. Pao, E. Wolak, and J.S. Harris, *IEEE Electron Device Lett.* **10**, 104 (1989).

[14] P. Cheng and J.S. Harris, *Appl. Phys. Lett.* **56**, 1676 (1990).

[15] E.R. Brown, T.C.L.G. Sollner, C.D. Parker, W.D. Goodhue, and C.L. Chen, *Appl. Phys. Lett.* **55**, 1777 (1989).

[16] T.C.L.G. Sollner, W.D. Goodhue, P.E. Tannenwald, C.D. Parker, and D.D. Peck, *Appl. Phys. Lett.* **43**, 588 (1983).

[17] R. Kapre, A. Madhukar, K. Kaviani, S. Guha, and K.C. Rajkumar, *Appl. Phys. Lett.* **56**, 922 (1990).

[18] J.R. Söderström, D.H. Chow, and T.C. McGill, *IEEE Electron Device Lett.* **EDL-11**, 27 (1990).

[19] E.R. Brown, C.D. Parker, L.J. Mahoney, J.R. Söderström, and T.C. McGill, submitted to the Device Research Conference, 1990.

[20] A.R. Bonnefoi, D.H. Chow, and T.C. McGill, *Appl. Phys. Lett.* **47**, 888 (1985).

[21] F. Capasso, K. Mohammed, and A. Y. Cho, *IEEE J. Quantum Electron.* **QE-22**, 1853 (1986).

[22] T.K. Woodward, T.C. McGill, H.F. Chung, and R.D. Burnham, *IEEE Electron Device Lett.* **9**, 122 (1988).

[23] F. Capasso, S. Sen, A. Cho, and D.L. Sivco, *Appl. Phys. Lett.* **53**, 1056 (1988).

[24] M.A. Reed, W.R. Frensley, R.J. Matyi, J.N. Randall, and A.C. Seabaugh, *Appl. Phys. Lett.* **54**, 1034 (1989).

[25] C.H. Yang, Y.C. Kao, and H.D. Shih, *Appl. Phys. Lett.* **55**, 2742 (1989).

[26] S.S. Rhee, G.K. Chang, T.K. Carns, and K.L. Wang, *Appl. Phys. Lett.* **56**, 1061 (1990).

[27] E.R. Brown, C.D. Parker, and T.C.L.G. Sollner, *Appl. Phys. Lett.* **54**, 934 (1989).

[28] E.U. Condon, *Rev. Mod. Phys.* **3**, 43 (1931).

[29] M.C. Payne and J.C. Inkson, *Surf. Sci.* **159**, 485 (1985).

[30] S. Collins, D. Lowe, and J.R. Barker, *J. Phys. C (UK)* **20**, 6213 (1987).

[31] E.H. Hauge and J.A. Støvneng, *Rev. Mod. Phys.* **61**, 917 (1989).

[32] M. Büttiker and R. Landauer, *J. Phys. C (UK)* **21**, 6207 (1988).

[33] D. Lowe and S. Collins, *J. Phys. C (UK)* **21**, 6210 (1988).

[34] K.K. Thornber, T.C. McGill, and C.A. Mead, *J. Appl. Phys.* **38**, 2384 (1967).

[35] M. Büttiker and R. Landauer, *Phys. Rev. Lett.* **49**, 1739 (1982).

[36] R. Landauer, address at "Workshop on Quantum Devices," sponsored by the Air Force Office of Scientific Research, Atlanta, Georgia, Sept. 15-16, 1988, unpublished.

[37] M. Büttiker, private communication.

[38] T.F. Hartman, *J. Appl. Phys.* **33**, 3427 (1962).

[39] F.T. Smith, *Phys. Rev.* **118**, 349 (1960).

[40] L.A. MacColl, *Phys. Rev.* **40**, 621 (1932).

[41] D. Bohm, *Quantum Theory* (Dover, New York, 1979), p. 291, Eq. 74(a).

[42] L. Esaki and R. Tsu, *IBM J. Res. Develop.* **14**, 61 (1970).

[43] G.C. Osbourn, *Phys. Rev. B* **27**, 5126 (1983).

[44] R.H. Miles, J.O. McCaldin, and T.C. McGill, *J. Crystal Growth* **85**, 188 (1987).

[45] J.A. Valdmanis, G. Mourou, and C.W. Gabel, *Appl. Phys. Lett.* **41**, 211 (1982).

[46] D.H. Auston, *IEEE J. Quantum Electron.* **QE-24**, 221 (1988).

[47] D. Krökel, D. Grischowsky, and M.B. Ketchen, *Appl. Phys. Lett.* **54**, 1046 (1989).

[48] J.F. Whitaker, G.A. Mourou, T.C.L.G. Sollner, and W.D. Goodhue, *Appl. Phys. Lett.* **53**, 385 (1988).

[49] S.K. Diamond, E. Özbay, M.J.W. Rodwell, D.M. Bloom, Y.C. Pao, E. Wolak, and J.S. Harris, in *OSA Proceedings on Picosecond Electronics and Optoelectronics*, Vol. 4 of the OSA Proceeding Series, T.C.L.G. Sollner and D.M. Bloom, eds. (Optical Society of America, Washington, D.C., 1989), p. 101.

[50] N.H. Schiller, in *Semiconductors Probed by Ultrafast Laser Spectroscopy, Vol. II*, R.R. Alfano, ed. (Academic, New York, 1984), Chap. 26.

[51] H. Kume, K. Koyama, K. Nakatsugawa, S. Suzuki, and D. Fatlowitz, *Appl. Optics* **27**, 1170 (1988).

[52] J. Shah, *IEEE J. Quantum Electron.* **QE-24**, 276 (1988).

[53] Y. Aoyagi, Y. Segawa, and S. Namba, in *Semiconductors Probed by Ultrafast Laser Spectroscopy, Vol. I*, R.R. Alfano, ed. (Academic, New York, 1984), Chap. 10.

[54] B. Deveaud, J. Shah, T.C. Damen, B. Lambert, and A. Regreny, *Phys. Rev. Lett.* **58**, 2582 (1987).

[55] M. Tsuchiya, T. Matsusue, and H. Sakaki, *Phys. Rev. Lett.* **59**, 2356 (1987).

[56] D. von der Linde, J. Kuhl, and E. Rosengart, *J. Lumin* **24/25**, 675 (1981).

[57] S. Tarucha and K. Ploog, *Phys. Rev. B* **39**, 5353 (1989).

[58] H. Schneider, K. von Klitzing, and K. Ploog, *Europhys. Lett.* **8**, 575 (1989).

[59] P. Guéret, A. Baratoff, and E. Marclay, *Europhys. Lett.* **3**, 367 (1987).

[60] P. Guéret, E. Marclay, and H. Meier, *Appl. Phys. Lett.* **53**, 1617 (1988).

[61] D. Esteve, J.M. Martinis, C. Urbina, E. Turlot, M.H. Devoret, H. Grabert, and S. Linkwitz, *Physica Scripta* **T29**, 121 (1989).

[62] P.H. Cutler, T.E. Feuchtwang, T.T. Tsong, H. Nguyen, and A.A. Lucas, *Phys. Rev. B* **35**, 7774 (1987).

[63] M.A. Newkirk and K.J. Vahala, *Appl. Phys. Lett.* **55**, 939 (1989).

[64] J.M. Weisenfeld, M.S. Heutmaker, I. Bar-Joseph, D.S. Chemla, T.Y.Chang, C.A. Burrus, and J.S. Perino, *Appl. Phys. Lett.* **55**, 1109 (1989).

[65] L.F. Luo, R. Beresford, W.I. Wang, and E.E. Mendez, *Appl. Phys. Lett.* **24**, 2133 (1989).

[66] T.B. Norris, X.J. Song, W.J. Schaff, L.F. Eastman, G. Wicks, and G.A. Mourou, *Appl. Phys. Lett.* **54**, 60 (1989).

Chapter 2

Tunneling Time Measurements in Undoped Double-Barrier Heterostructures

2.1 Introduction

2.1.1 Background

As mentioned in Chapter 1, the electrical properties of the double-barrier heterostructure, and in particular the properties at high frequencies, have been of great interest since its proposal by Tsu and Esaki [1]. The desire to characterize the high-frequency behavior of the double-barrier heterostructure stems from interest in its use as an oscillator [2, 3, 4] and as a switching element [5, 6]. However, the time associated with tunneling has been the subject of many years of discussion [7]. Recently there have been several experimental studies of the temporal response of double barrier heterostructures. Whitaker and coworkers [8] and Diamond et al. [9] have used electrooptic sampling measurements to study single tunnel devices. Tsuchiya et al. [10] used direct time-resolved detection of the photoluminescence from carriers in the quasi-bound states in the quantum wells of undoped double-barrier heterostructures. They studied the decay of the photoluminescence from carriers in the quantum well, and, by assuming that escape of heavy holes was negligible, claimed to measure the electron population in the quantum well as a function of the barrier thickness. In this chapter we describe time-resolved photoluminescence studies of undoped GaAs/AlAs/GaAs/-AlAs/GaAs double-barrier heterostructures using the two-beam technique of photoluminescence excitation correlation spectroscopy (PECS). Using this different technique, we have extended the experiments of Ref. [10], which were limited to times greater than 60 ps, to significantly shorter times. In addition, our experimental results indicate that the analysis of the experimental data of Ref. [10], which ignored the effect of hole tunneling, is incomplete, and we discuss a new model of the tunneling of holes in confined structures.

2.1.2 Summary of Results

We report a study of the decay of photoexcited carriers in GaAs/AlAs/GaAs/-AlAs/GaAs double-barrier heterostructures, using photoluminescence excitation correlation spectroscopy (PECS). An analysis of the PECS experimental technique is presented using numerical integration of the rate equations governing the PECS signals. This extends previous analyses of the experimental signals, which were limited to certain special cases, to a more general class of problems. The tunneling time for electrons to escape from the lowest quasi-bound state in the quantum wells of double-barrier heterostructures with barriers between 16 and 62 Å has been measured at 80 K. The decay time for samples with barrier thicknesses from 16 Å (≈12 ps) to 34 Å (≈800 ps) depends exponentially on barrier thickness, in reasonable agreement with calculations of electron tunneling time derived from the energy width of the quasi-bound state resonance. Electron and heavy-hole carrier densities are observed to decay at the same rate, in contrast to resonance-width calculations that indicate that heavy-hole tunneling times should be much longer than those for electrons. The rapid escape of heavy holes can be explained by considering the effects of mixing of light- and heavy-hole bands in the quantum well confined hole states. We also studied an undoped double-barrier heterostructure with superlattice barriers, and observed a decay time of 350±60 ps at 80 K. Finally we studied a double barrier with pure AlAs barriers and a narrower quantum well, in which two time constants could be extracted from the time-resolved data.

2.1.3 Outline of Chapter

The photoluminescence excitation correlation technique used for time-resolved studies of photoluminescence is described in Section 2.2, which also includes a description of the experimental setup, and numerical analysis of the experimental signals. The samples studied are described in Section 2.3. Section 2.4 describes experimental results at 80 K and as a function of temperature from 80 to 5 K. The experimental results are discussed in Section 2.5. Section 2.6 compares the present work with results from other workers using complementary techniques. Finally, conclusions are summarized in Section 2.7.

2.2 Time-Resolved Luminescence Technique

2.2.1 Background

The time-resolved luminescence technique used in this chapter depends upon nonlinearity in the photoluminescence process as a mechanism to generate an integrated photoluminescence signal, in response to excitation by two optical pulses, that depends upon the delay between the two pulses. This technique was developed by several groups, who took advantage of different nonlinearities to achieve similar ends. Mahr and coworkers [11, 12] took advantage of absorption saturation in organic dyes. Using the bimolecular recombination of photogenerated carriers, Rosen et al. [13] and von der Linde et al. [14] independently developed the technique that has been variously referred to as population mixing, picosecond excitation correlation, or photoluminescence excitation correlation spectroscopy, the term that we shall use. This technique, which is quite simple experimentally, measures a correlation function related to the evolution of the photoluminescence, rather than the exact temporal response of the photoluminescence emission. Various workers have used this technique for studies of hot carrier relaxation and cooling [14], recombination in p-type GaAs [13], spatial diffusion profiles [15], lifetimes near defects in GaAs substrates [16], and nonradiative decay times in intentionally radiation-damaged GaAs [17]. Similar experimental techniques have been used for transmission measurements, and allowed demonstrations of quantum beats in large organic molecules [18, 19].

The photoluminescence excitation correlation spectroscopy technique has been used in the present work for studies of tunneling escape from double-barrier heterostructures. The most complete analysis of this technique to date was by Johnson et al. [16], who derived analytical expressions for the experimentally observed signals in certain limiting cases. They found that, for the case where radiative recombination dominates the population evolution, the experimentally observed correlation signal is zero, and also derived analytical expressions for the situation where nonradiative recombination dominates. In Section 2.2.3 we will present a more general analysis that reduces to the results of Johnson et al. [16] for limiting cases, but allows numerical calculations of the signals in cases where both radiative and nonradiative decay processes are important in the evolution of the carrier densities.

2.2.2 Experimental Setup

The experimental setup is shown in Fig. 2.1. A dispersion compensated colliding pulse mode-locked (CPM) ring dye laser is used to generate a train of pulses 200 to 300 fs full width at half maximum (FWHM), at a repetition frequency of 120 MHz. The operation of the laser, alignment procedures, and routine maintenance are described in Appendix A. The laser output is centered at 6200 Å, corresponding to an energy of 2eV, and has a spectral width of approximately 20 to 50 Å FWHM, depending upon the pulse width. One of the two output pulse trains from the CPM laser is equally divided into two separate beams which are independently chopped at $f_1 = 1600$ and $f_2 = 2000$ Hz, and delayed with respect to one another by time γ ($-500 \leq \gamma \leq 500\,\text{ps}$). Metal-coated reflective retroreflectors (Newport BBR) were used in the two arms, one of which was mounted on a Klinger stepper motor that allowed motion of approximately 30 cm. After chopping and relative delay, the two beams are recombined and focused to a 25 μm diameter spot on the surface of the sample. The typical average power used was 0.5 mW per beam after chopping. The photoluminescence is spectrally resolved with a double pass spectrometer, and then detected by a GaAs pho-

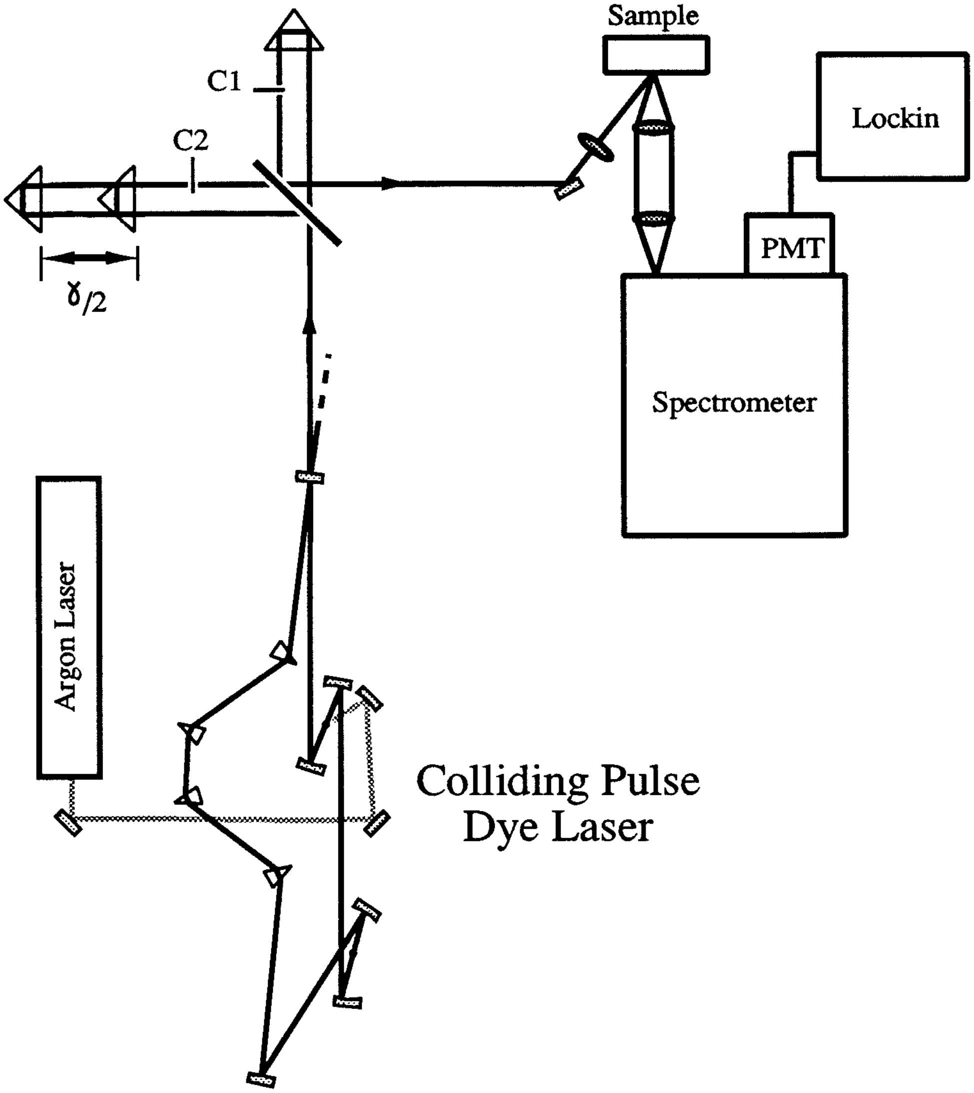

Figure 2.1: Experimental setup for time-resolved photoluminescence. The source of ultrafast optical pulses is the dispersion-compensated colliding pulse mode-locked (CPM) dye laser. The laser output is split into two beams of equal amplitude, which are mechanically chopped by C1 and C2, and then recombined and focused on the sample. Photoluminescence is imaged from the sample into a spectrometer, and detected with a GaAs photomultiplier tube (PMT), and a lock-in amplifier.

tomultiplier tube (PMT). After amplification, the PMT signal is synchronously detected by a lock-in amplifier at either the fundamental frequency f_1 or the sum frequency $f_{\rm sum} = f_1 + f_2$. It has recently been suggested [20] that detection using two lock-in amplifiers, connected in series, and referenced separately to f_1 and f_2, has improved noise reduction properties compared to the scheme used in the present work, where a reference signal generated directly at $f_{\rm sum}$ is used for a single lock-in. This possibility was not investigated in the present work. All data recording, control, and display functions were performed with a Hewlett Packard HP9836 computer. All of the results reported here were taken with the sample mounted in a helium immersion dewar, at a temperature between 80 and 5 K.

In order to guarantee reliable results, the interferometer must be carefully aligned to ensure that no walk-off (movement perpendicular to the direction of the beam) of the variably delayed beam occurs when the delay is changed. A misalignment of the interferometer is evident in data collected for positive and negative delays γ. The symmetry of the experimental apparatus requires the photoluminescence scans with delay to be symmetrical about zero delay, and any departure from this behavior is evidence of some asymmetry in the setup, which is usually related to the interferometer alignment. Therefore, we always present scans taken for both positive and negative delay, and these scans are expected to be symmetrical with respect to zero delay. Although active stabilization methods have been used for this purpose [21], it was found to be sufficient to use the following procedure to align the beam splitter and the retroreflector mounted on the stepper motor. With the CPM laser running, the retroreflector is moved to the end of its travel closest to the beam splitter. The retroreflector is then moved in the two directions perpendicular to the motion of the stepper motor until the laser spot is exactly in the center of the retroreflector, at the corner of the three reflective surfaces. This condition can be very accurately determined by placing the chopper C2 in the path of the beam, and viewing the interference pattern caused by the reflection of the laser beam, which is symmetric when properly aligned. Then the retroflector is moved to the opposite end of its travel on the stepper, and the beam splitter is again adjusted so that the laser beam hits exactly the center of the retroflector. The above procedure is repeated until the beam is correctly positioned at both ends of the stepper motor travel. Then the retroflector is translated approximately 0.5 cm so that the laser beam strikes flat areas, and not the edges, of the reflective surfaces in the retroreflector. This procedure ensures that the laser beam and the motion of the stepper motor are collinear, thus eliminating any beam walkoff as the delay is varied. It was also found with certain configurations of the CPM cavity that the output beam diverged sufficiently that the differing path length in the interferometer resulted in differing spot sizes. This was corrected by a pair of lenses just outside the CPM laser that collimated the beam.

2.2.3 Theory

The use of photoluminescence as a probe of the tunneling escape rates for carriers photoexcited in the quantum well of a double-barrier heterostructure, originated by Tsuchiya et al. [10], relies on photoexcitation by a short optical pulse. Whereas Tsuchiya et al. [10], used direct detection of the photoluminescence with a streak camera, in the present work we have used the photoluminescence excitation correlation spectroscopy (PECS) technique for time-resolved measurements. In this section we will present an analysis of the PECS technique that is more general than that obtained by previous workers [16], and present numerical calculations of the expected experimental signals for situations similar to those studied experimentally in the following sections.

In Fig. 2.2, we present a schematic diagram of the carrier processes in the quantum well that are relevant during the experiment. The conduction and valence bands are shown as a function of position, and the lowest electron and hole energy levels in the quantum well are indicated by dashed lines. Because of the higher heavy hole effective mass, the lowest hole level in the quantum well is a heavy hole state. The processes of excitation of electron-hole pairs by the incoming laser, tunneling of electrons and holes from the quantum well, and the radiative recombination of carriers between the lowest electron and heavy-hole states within the well are all shown in Fig. 2.2. It is the luminescence from the recombination of electrons and heavy holes in the lowest quantum well states that is detected in the experimental measurements of tunneling times.

In our experiments, the photoexcitation energy of the CPM laser is 2eV, which is considerably higher than the 1.6 to 1.8 eV quantum well transition observed in photoluminescence in the structures studied. However, recent estimates of the times for thermalization of electrons between subbands in $\mathrm{GaAs/Al_xGa_{1-x}As}$ multiple quantum wells have given times less than 200 fs [22]. This is consistent with the fact that we do not observe photoluminescence from the excited state transitions. We will therefore assume the thermalization of both electrons and holes to the lowest subband to be fast compared to the times of interest here, so that the effect of photoexcitation by an optical pulse is to instantaneously increase the carrier densities in the lowest electron and heavy hole quantum well states. The effects of the excess excitation energy on the carrier distribution functions, and in particular upon the carrier temperature, will be discussed in Section 2.5.

Measurements of the tunneling escape times for electrons and heavy holes are derived from the variation of the photoluminescence signal I_{sum}, detected at the sum chopping frequency, with delay γ. The sum-frequency signal is monitored at

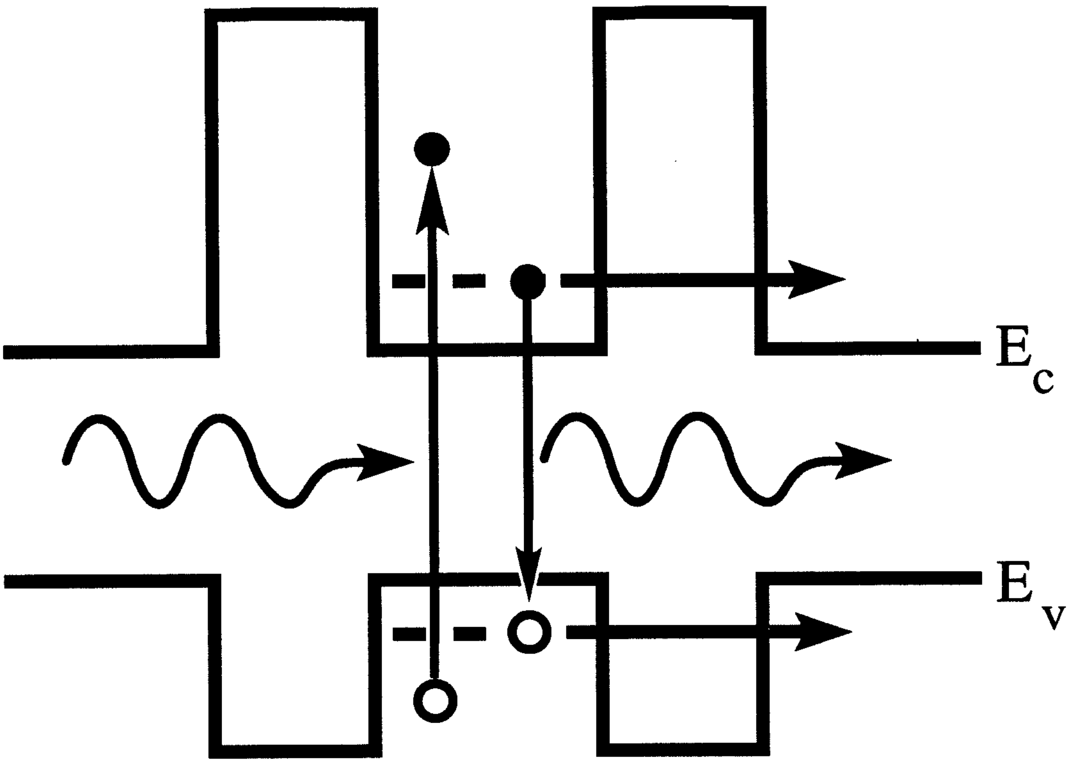

Figure 2.2: Schematic diagram of relevant carrier processes occurring in the double-barrier samples during photoluminescence. The conduction and valence band edges are shown as a function of position. Also shown are photoexcitation of electron-hole pairs by the laser, tunneling of electrons and holes out of the well, and recombination of carriers confined in the lowest quasi-bound electron and heavy-hole states in the quantum well.

a wavelength corresponding to the lowest confined electron to heavy-hole transition. If the lowest-energy confined electron and heavy-hole carrier densities are n and p, respectively, then the photoluminescence detected by the photomultiplier tube is $I_{\mathrm{PL}} \propto \int np\,dt$, where the integration is over times long compared to the tunneling processes of interest here, but short compared to the chopping periods. Since the laser excitation is periodic with period $\mathrm{T}_{\mathrm{rep}}$ it is natural to consider the sum-frequency component of the photoluminescence, $\mathrm{I}_{\mathrm{sum}}(\gamma)$, in terms of the integrated photoluminescence detected in one period $\mathrm{T}_{\mathrm{rep}}$. Assuming that each optical pulse creates an equal density g of electron and holes, the chopped optical generation function is given by

$$G_{\mathrm{chop}}(t,\gamma) = g \sum_{m=-\infty}^{+\infty} [S_{f_1}(t)\delta(t - m\mathrm{T}_{\mathrm{rep}}) + S_{f_2}(t)\delta(t - \gamma - m\mathrm{T}_{\mathrm{rep}})],$$

where $S_{f_1}(t)$ and $S_{f_2}(t)$ are unit amplitude square waves at the chopping frequencies f_1 and f_2, respectively, $\delta(t)$ is the Dirac-delta function, and γ is the relative delay between the two arms of the interferometer. Because of the chopping, during the experiment the sample is exposed to zero, one, or two optical pulse trains at various times, depending upon the instantaneous values of $S_{f_1}(t)$ and $S_{f_2}(t)$. We will assume that the populations, and thus the photoluminescence signal, achieve a steady state value in a time short compared to the chopping periods. Then the sum-frequency signal, $I_{\mathrm{sum}}(\gamma)$, can be simply expressed in terms of the integrated photoluminescence detected in these three cases of exposure to zero, one, or two unchopped pulse trains. The integrated photoluminescence intensity detected in one period $\mathrm{T}_{\mathrm{rep}}$ is proportional to $\int_0^{\mathrm{T}_{\mathrm{rep}}} np\,dt$. For excitation by the unchopped one-pulse-train optical generation function

$$G_1(t) = g \sum_{m=-\infty}^{+\infty} \delta(t - m\mathrm{T}_{\mathrm{rep}}),$$

the luminescence is defined to be I_1, which is obviously independent of delay

γ, since there is only one pulse train. Similarly, $I_2(\gamma)$ is the integrated photoluminescence intensity corresponding to the unchopped two-pulse-train optical generation function

$$G_2(t,\gamma) = g \sum_{m=-\infty}^{+\infty} [\delta(t - m\mathrm{T}_{\mathrm{rep}}) + \delta(t - \gamma - m\mathrm{T}_{\mathrm{rep}})].$$

By considering the component of the photoluminescence response at the sum chopping frequency, it can be shown that $\mathrm{I}_{\mathrm{sum}}(\gamma)$ is simply given by

$$\mathrm{I}_{\mathrm{sum}}(\gamma) \propto [I_2(\gamma) - 2I_1]. \tag{2.1}$$

Eq. 2.1 is very general, depending only on the nature of the synchronous detection, and the assumption that the populations reach steady state quickly compared to the chopping periods. This simple relation allows the calculation of the sum-frequency signal in any case in which the populations $n(t)$ and $p(t)$ are known. It can be seen from Eq. 2.1 that $\mathrm{I}_{\mathrm{sum}}$ reflects the departure from linearity of the response of the photoluminescence with excitation intensity, because it measures the difference between the photoluminescence detected during excitation by two pulses, and twice the luminescence detected during excitation by one pulse.

For the present case, considering radiative recombination and tunneling, the evolution of the electron and hole populations in the quantum well can be described by simple rate equations,

$$\frac{dn}{dt} = G(t,\gamma) - \frac{n}{\tau_e} - Bnp \tag{2.2}$$

$$\frac{dp}{dt} = G(t,\gamma) - \frac{p}{\tau_{\mathrm{hh}}} - Bnp. \tag{2.3}$$

In Eqs. 2.2 and 2.3, B is a constant related to the radiative recombination rate [23], and $G(t,\gamma)$ is the appropriate optical generation function. The two times τ_e and τ_{hh} are the tunneling escape times for the electrons and heavy holes, respectively. Eqs. 2.2 and 2.3 can be solved numerically for the case $G(t,\gamma) = G_1(t)$

to obtain $I_1 = \int_0^{\mathrm{T_{rep}}} np\,dt$, and similarly for $G(t,\gamma) = G_2(t,\gamma)$ to obtain $I_2(\gamma)$. $\mathrm{I_{sum}}(\gamma)$ can then be found using Eq. 2.1. The advantage of this approach over that used in previous analyses [16] of this experimental technique is that the nonlinearity in the rate equations can be handled easily, and it is not necessary to make assumptions regarding the radiative or nonradiative nature of the population evolution. This analysis can easily be extended to other experimental situations where, for example, the populations of excitons or other levels are important.

Eqs. 2.1-2.3 can also be solved analytically in certain simple cases [16]. If the electron and hole population evolutions are dominated by tunneling, the responses to a single optical pulse are $n_i(t)$ and $p_i(t)$, the population responses to two optical pulses are independent, and $n_i(\mathrm{T_{rep}})$ and $p_i(\mathrm{T_{rep}})$ are small compared to g, the sum-frequency signal is proportional to the cross correlation [16]

$$I_{\mathrm{sum}}(\gamma) \;\propto\; \int_0^{\mathrm{T_{rep}}} \Big[n_i(t)p_i(t-\gamma) + n_i(t-\gamma)p_i(t)\Big]\,dt. \tag{2.4}$$

This expression, which is responsible for the name "correlation spectroscopy," shows that the sum-frequency signal is due to the recombination of electrons created by the first pulse with holes created by the second pulse, and vice versa. The first term corresponds to recombination of the electrons created by the first pulse at time $t = 0$, with holes created by the pulse at $t = \gamma$. The second term is due to recombination of the electrons created by the pulse at time $t = \gamma$, with holes created by the pulse at time $t = 0$. The fact that the sum-frequency signal is composed of two terms is a major advantage of this technique, because it allows access to information regarding both the electron and hole decay times, τ_e and τ_{hh}, as will be shown next. This distinguishes the PECS technique from direct, time-resolved detection of the photoluminescence. Use of the PECS technique enabled the measurements presented in this chapter, which were the first to obtain information regarding the escape of both electrons and heavy holes.

In the tunneling-dominated case, *i.e.*, when the evolutions of the electron and hole populations are dominated by tunneling, the electron and heavy-hole densities decay exponentially with time constants τ_e and τ_{hh}, respectively. In this case, substitution into Eq. 2.4 shows that the sum-frequency signal is proportional to the sum of two exponentials of equal amplitude,

$$I_{sum}(\gamma) \propto \left[\exp\left(-|\gamma|/\tau_e\right) + \exp\left(-|\gamma|/\tau_{hh}\right)\right]. \qquad (2.5)$$

In the radiative recombination dominated case, i.e., when the population evolution is not significantly affected by tunneling, the assumptions leading to Eqs. 2.4 and 2.5 are not valid. In this case, the sum-frequency component of the photoluminescence is zero [16]. This is because when radiative recombination dominates the population evolution, every photon absorbed produces a photon out. Thus photoluminescence intensity is linearly dependent upon the photoexcitation intensity, and the sum-frequency component of the photoluminescence is zero, according to Eq. 2.1.

To determine the applicability of Eq. 2.5 to the intermediate region between the radiative-recombination-dominated and tunneling-dominated cases, Eqs. 2.1-2.3 have been numerically integrated for various values of τ_e, τ_{hh}, and B. In Fig. 2.3 we show as solid lines the sum-frequency photoluminescence signal as a function of delay calculated by numerically integrating Eqs. 2.1-2.3. Also shown in Fig. 2.3 as dashed lines are curves calculated from the simple result of Eq. 2.5. The curves shown in Fig. 2.3 were calculated for experimentally realistic parameters: the electron tunneling escape time τ_e was 100 ps, and the heavy-hole tunneling escape time τ_{hh} was 1000 ps. The excitation density per optical pulse g is 10^{11}cm^{-2}, and the repetition period of the laser T_{rep} is 8 ns. Matsusue et al. [23] have measured the radiative recombination constant B in 90 Å GaAs quan-

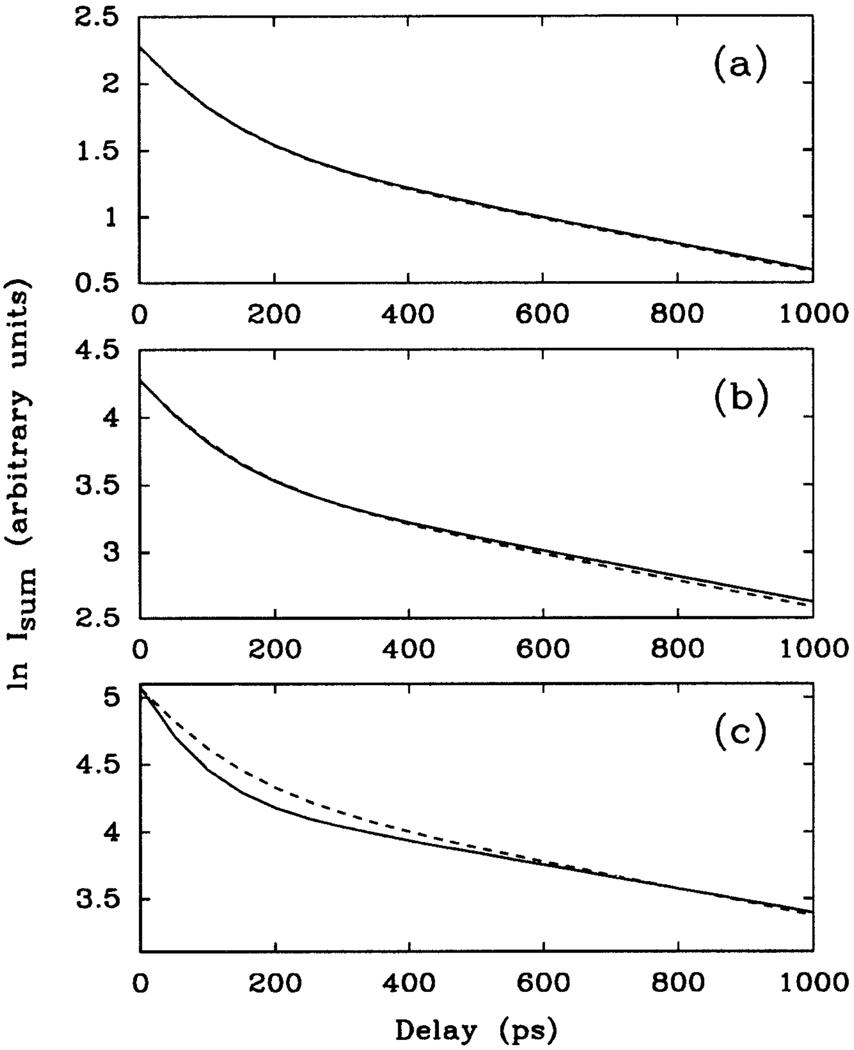

Figure 2.3: Calculated sum-frequency delay scans for three values of B, the radiative recombination constant. (a) $B = 10^{-3}\text{cm}^2/\text{s}$, the value from Ref. [23] at 80 K, (b) $B = 10^{-2}\text{cm}^2/\text{s}$, (c) $B = 10^{-1}\text{cm}^2/\text{s}$. The solid line shows the signal calculated by integrating the rate equations, and the dashed line shows the simple expression given in Eq. 2.5. It can be seen that the simple expression from Eq. 2.5 is very accurate in all three cases. The electron and heavy-hole tunneling decay times τ_e and τ_{hh} are 100 and 1000 ps, respectively, the excitation density per optical pulse g is 10^{11}cm^{-2}, and the repetition period of the laser T_{rep} is 8 ns.

tum wells, and found a value of 10^{-3}cm^2/s at 80 K, and we show in Fig. 2.3(a) the behavior for this value of B. In Figs. 2.3(b) and (c), we show the same calculation for progressively more radiative-recombination-dominated cases, where the values of B were 10^{-2} and 10^{-1}cm^2/s, respectively. Comparing the exactly integrated curves shown as solid lines, and the simple expression, shown as dashed lines, in Fig. 2.3, it can be seen that the simple expression is very accurate even in the extreme case shown in Fig. 2.3(c), where the radiative recombination process dominates the evolution of the carrier densities.

The case of extreme recombination-dominated population evolution was also studied, where the tunneling escape times were much longer than the radiative recombination time. It was found that that the sum-frequency signal calcuated for this case is independent of delay. Thus in the case where tunneling becomes negligible, we still do not expect to see $I_{\text{sum}}(\gamma)$ decay with the radiative lifetime. In this case, where the tunneling escape times are very long, some other process such as nonradiative recombination may become important, and the rate equations 2.2 and 2.3 will have to be modified accordingly.

In summary, we have numerically solved for the behavior of the sum-frequency signal detected in the PECS experiment as a function of delay for realistic experimental conditions. Our results indicate that the simple expression of Eq. 2.5 is valid in the cases studied, and we will use this equation as the basis for interpreting our data. We also pointed out that in the case where tunneling becomes negligible, the sum-frequency signal does not decay with the radiative recombination lifetime, and this technique is therefore insensitive to the exact magnitude of the radiative recombination time.

2.3 Samples

Double-barrier heterostructures were grown on (100) GaAs substrates by molecular beam epitaxy in a Perkin-Elmer 430 system at 600 °C. All layers were nominally undoped with an estimated residual carbon acceptor concentration of $10^{14}\mathrm{cm}^{-3}$. Three sample series were studied, labelled A, B, and C, and sample parameters are summarized in Table 2.1. Sample series A, with a constant quantum well width of 58 Å and pure AlAs barriers of varying thicknesses, consisted of 7 samples with barrier thicknesses ranging from 16 to 62 Å. All samples in this series were grown on the following buffer layers: 0.5 μm of GaAs, a superlattice buffer layer consisting of 5 periods of (50 Å $\mathrm{Al_{0.35}Ga_{0.65}As}$, 500 Å GaAs), and a 0.7 μm layer of GaAs. This was to provide a high quality layer on which to grow the double-barrier heterostructure; the final GaAs layer eliminates any optical effects from the superlattice. Then a symmetrical GaAs/AlAs/GaAs/AlAs/GaAs double-barrier heterostructure was grown, with a well thickness of 58 Å, and a final GaAs layer thickness of 300 Å, which served as a cap. Seven samples were studied, with bulk growth rate information predicting barrier thicknesses of 16, 22, 28, 34, 34, 48, and 62 Å. High resolution transmission electron microscopy confirmed the barrier thicknesses of the 16 Å sample and one of the 34 Å samples, within an uncertainty of 2 monolayers. We estimate an absolute uncertainty in barrier thickness of ±2 monolayers for all of the samples, although control of the relative barrier thickness between samples appears to be better than 1 monolayer. The single sample B1 had undoped superlattice barriers, and corresponded to the doped structure with a peak-to-valley current ratio of 21.7:1 at 77 K [24], one of the highest values ever reported for a pure GaAs/AlAs heterostructure tunnel device. This sample was grown on a 0.5 μm undoped GaAs buffer grown directly on the GaAs substrate, and had a GaAs well of width 49 Å. The superlattice

Sample	Growth Number	Well Width (Å)	Barrier Thickness (Å)
A1	III-069	58	16
A2	III-064	58	22
A3	III-062	58	28
A4	III-059	58	34
A5	III-066	58	34
A6	III-070	58	48
A7	III-063	58	62
B1	III-088	49	(see text)
C1	III-329	45	37

Table 2.1: Parameters for the samples studied. Series A, consisting of seven samples, all had constant well thickness and varying AlAs barrier thickness. Sample B1 had superlattice barriers which were each composed of three 8.5 Å AlAs layers, separated by two 8.5 Å GaAs layers. Sample C1 was similar to sample A4, but had a narrower 45 Å quantum well.

barriers were each composed of three 8.5 Å AlAs layers, separated by two 8.5 Å GaAs layers. Again, the final layer was a 300 Å GaAs cap. The final sample, C1, was similar to sample A4, but had a narrower quantum well width of 45 Å, which increased the confinement energy of states in the well. This sample was grown directly on a 0.5 μm GaAs buffer layer.

2.4 Results

2.4.1 Time-resolved Measurements at 80 K

In Fig. 2.4, we present typical photoluminescence spectra taken at 80 K at the fundamental and sum chopping frequencies, for the 28 Å barrier sample A3. The spectrum at the fundamental frequency consists of a single feature centered at 7650 Å. The wavelength of the feature in the fundamental frequency spectrum is in reasonable agreement with the calculated position of 7730 Å for the transition from the lowest electron subband to the lowest heavy-hole subband in a 58 Å quantum well. The width of the fundamental frequency photoluminescence is consistent with broadening by monolayer fluctuations of the quantum well width, which indicates the samples are of high quality. The peak of the corresponding feature in the sum-frequency spectrum is shifted slightly to longer wavelengths; the reason for this shift is not clear. The sum-frequency peak is lower in amplitude by a factor of 0.28 compared to the peak in the fundamental frequency photoluminescence. This compares well with the tunneling-dominated case, where the ratio of the sum-frequency signal to the fundamental signal is expected to be 0.27:1 [16].

In Fig. 2.5, we present several semilogarithmic plots of typical peak photoluminescence intensity at the sum chopping frequency, as a function of the time

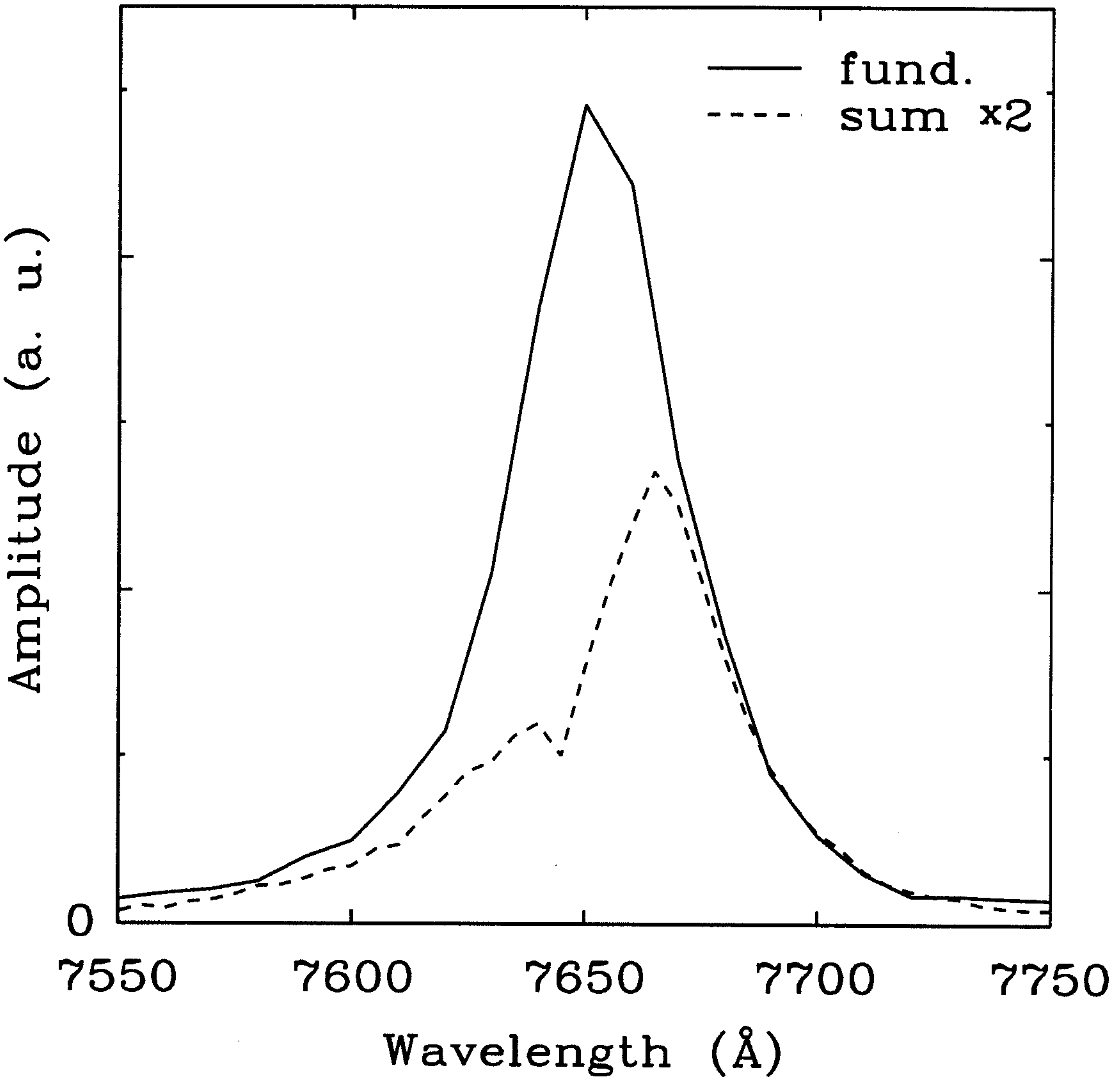

Figure 2.4: Typical correlation photoluminescence spectra for 28 Å barrier sample A3 at 80 K. Shown are luminescence signals at the fundamental chopping frequency (solid line) and the sum-frequency (dashed line). Both scans were taken with delay $\gamma = 0$. The sum-frequency spectrum has been multiplied by 2.

delay γ between the two pulses, taken at 80 K. All three scans show a coherence peak at exactly zero delay, which is due to the optical interference of the two incident pulses on the sample, in combination with the nonlinearity of the photoluminescence with pump intensity. Instabilities in the interferometer, due to vibrations, prevent stable fringes from being formed on the sample when the two pulses overlap in time, and result in fluctuations of the intensity from zero to twice the incident average intensity. Because luminescence is a nonlinear function of the excitation intensity, this results in a greater photoluminescence signal. The width of this coherent artifact, if resolved, was confirmed to be equal to the autocorrelation width of the laser pulses, and serves both as a measure of the pulse width at the sample, and also as a convenient and precise alignment of the zero of the relative delay in the interferometer. However, the coherence peak is completely unrelated to the decay of the electron and heavy hole populations. The scan shown in Fig. 2.5(a) for sample A3, which has 28 Å barriers, was taken at a wavelength of 7665 Å, the peak of the sum-frequency photoluminescence spectrum shown in Fig. 2.4. This delay scan consists of the coherence peak at zero delay discussed above, with wings extending to much longer times. The wings in the sum-frequency delay scan shown in Fig. 2.5(a) show a dependence upon delay well described by a single exponential, over range of more than 2 in the logarithm of the amplitude. Fits to this sum-frequency delay data using a single exponential are shown as dashed lines in Fig. 2.5(a), where the negative and positive delay portions of the scans were fitted separately, and the two time constants fitted are combined to yield a best fit value for the decay time. For the 28 Å barrier sample A3 shown in Fig. 2.5(a), this single decay time was 236 ± 20 ps. In Fig. 2.5(b), we show the decay scan for the 22 Å barrier sample, A2, again taken at the peak of the sum-frequency photoluminescence spectrum. The decay is again fitted quite well by a single exponential, although the increased tunneling rates in this sam-

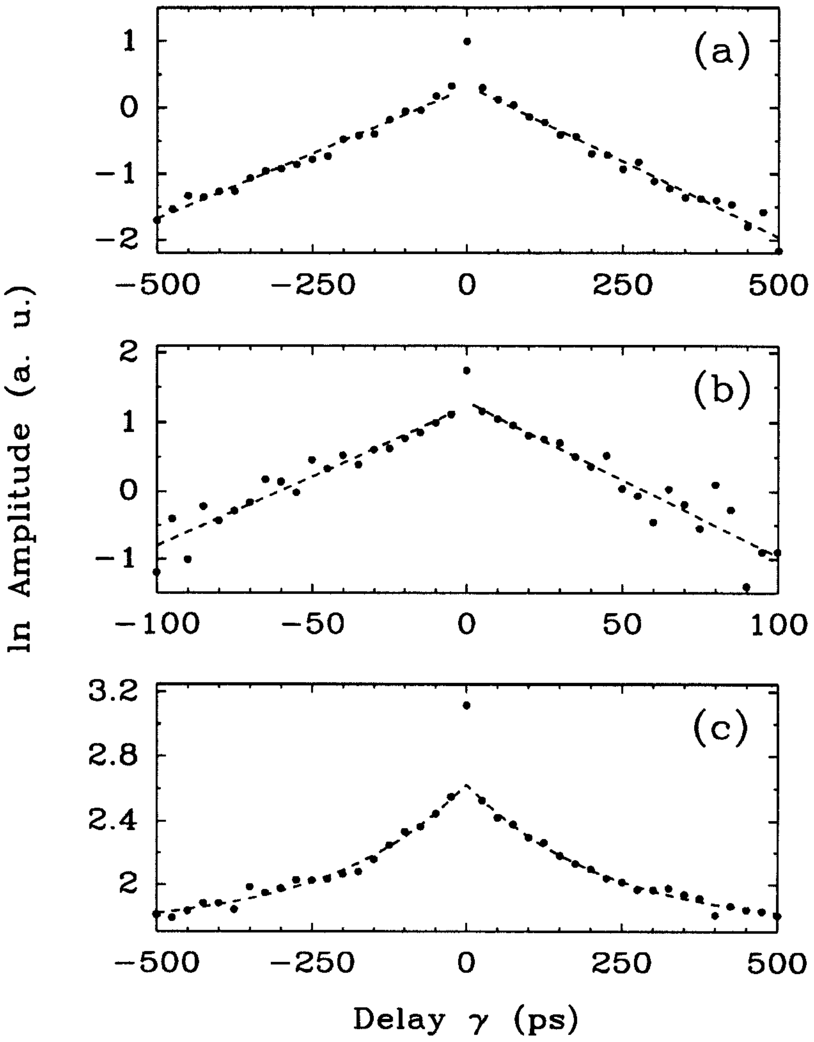

Figure 2.5: Semilogarithmic plots of the variation of the sum-frequency luminescence signal with delay γ at 80 K. All three scans show the coherent artifact at $\gamma = 0$ due to interference of the two optical pulses. (a) Sample A3 (28 Å barriers) is described well by a single decay time of 236 ± 20 ps, derived from the fits indicated by dashed lines to the negative and positive portions of the scan. (b) Sample A2 (22 Å barriers) is described by a single decay time of 47 ± 5 ps. (c) Sample C1, which has a narrower quantum well, shows double exponential behavior, and the fit shown by a dashed line gives time constants of 150 and 3500 ps. Note the differing time scales for the three plots.

ple reduce the photoluminescence intensity and result in poorer signal-to-noise in the data shown. The single decay time for this scan was 47 ± 5 ps, based on the fits shown as dashed lines. Finally, in Fig. 2.5(c), we show the decay scan for sample C1, which had a narrower 45 Å quantum well, taken at the peak of the sum-frequency photoluminescence, which was at 7375 Å. The decay in this sample is not well described by a single exponential. We show in the same figure a dashed line, which is a best-fit of the sum of two exponentials with equal amplitude, the functional form expected according to Eq. 2.5. The double exponential fits the data very well, and gives time constants of 130 and 3500 ps. Although the data are not shown, the superlattice-barrier structure sample C1 showed single exponential decay at 80 K, with a time constant of 350±60 ps.

2.4.2 Dependence upon Barrier Thickness

The samples in series A described above were studied under similar conditions, and all showed delay scans that could be fitted well by a single exponential decay. In Fig. 2.6, we have plotted the exponential decay time at 80 K. The decay time depends exponentially on barrier thickness for barriers up to approximately 34 Å. Over this range of exponential dependence, the decay time varies by two orders of magnitude, ranging from a time of approximately 12 ps at 16 Å, to approximately 800 ps at 34 Å. The two samples A4 and A5 that are nominally identical show very similar decay times, indicating excellent sample reproducibility. Given the rapid variation of the decay times with barrier thickness seen in Fig. 2.6, this indicates that the barrier thickness repeatability between samples is considerably better than the ±2 monolayer uncertainty estimated in the absolute barrier thickness. For barriers thicker than 34 Å, the decay time seems to approach a value that is independent of the barrier thickness. This is probably due to some some

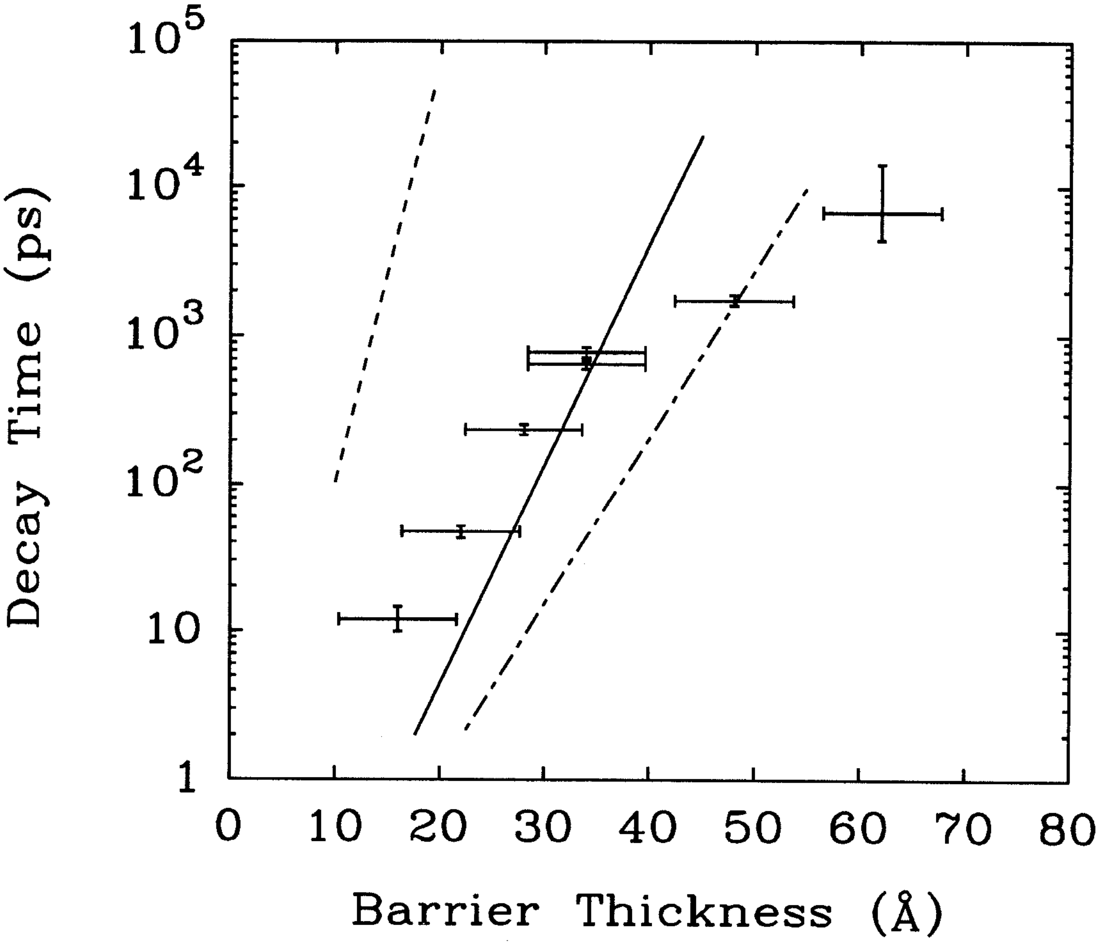

Figure 2.6: Measured decay times at 80 K as a function of barrier thickness for sample series A, where the quantum well thickness is 58 Å. The data points are the measured decay times, with error bars on the thickness based on absolute uncertainty in the barrier thickness, and error bars on the decay times from uncertainties in the fits to the delay scans. The solid, dashed, and dot-dashed lines are the electron, heavy-hole, and light-hole tunneling times, respectively, calculated from the widths of the lowest-energy transmission resonances.

nonradiative process unrelated to tunneling that becomes more important as the barriers become thicker and the tunneling escape rates decrease. Due to the 120 MHz repetition rate of the excitation pulses, and the limited −500 to 500 ps range for the delay, γ, there is an upper limit on the order of 2 ns to the decay times that can be measured accurately with our technique. Consequently, the result for the sample with a barrier thickness of 62 Å should be viewed with some caution. Our measurements extend the previous work of Tsuchiya et al. [10] to significantly shorter times, and our measured decay times are about a factor of 4 longer than those of Tsuchiya et al. [10].

2.4.3 Temperature-Dependent Measurements

The dependence of decay time upon temperature was studied for the 28 Å sample A3, at temperatures from 80 to 5 K. The laser power for this experiment was reduced to an average power per beam of 0.3 mW before chopping, and one measurement was taken at 5 K at an average power per beam of 0.16 mW. The laser pulsewidth for these measurements was 300 fs FWHM. Over this range the sum-frequency signal dependence on delay was exponential, with a single decay time, and the decay time increased slightly with decreasing temperature.

2.5 Discussion

The exponential dependence of the decay times seen in Fig. 2.6 for barrier thicknesses between 16 and 34 Å is characteristic of a decay time related to tunneling. To allow comparison with theory, in Fig. 2.6 we have also plotted the theoretical times for electrons, heavy holes, and light holes to tunnel out of the quantum well, calculated using the energy widths of the transmission resonances and the uncertainty principle. The solid, dashed, and dot-dashed lines are the calculated electron, heavy-hole, and light-hole tunneling times, respectively. From Ref. [25], the time for a particle to tunnel out of a quasi-bound state in the quantum well is related to the energy width ΔE_{FWHM} of the corresponding resonance in the transmission probability by $\tau = \hbar / \Delta E_{FWHM}$. The transmission probability is calculated using the transfer matrix approach of Kane [26], modified to account for the different effective masses of the particle in the quantum well and in the barrier.

For electrons, we have considered only Γ-point barriers. It is appropriate to use a simple one-band expression for the wave vector in the well, given by $k = (2m_w^* m_e E/\hbar^2)^{1/2}$, where m_w^* is the effective mass in the GaAs well, m_e is the free electron mass, and E is the energy of the particle with respect to the GaAs band edge. However, with the pure AlAs barriers in our samples, the lowest quasi-bound electron state has an energy far from the band edge in the AlAs barriers, and the one-band model overestimates the wave vector in the barriers. Thus, we have used a two-band model [27] to calculate the electron wave vector in the barriers. The conduction band barrier height used in these calculations was 1.07 eV, corresponding to a valence band offset of 0.55 eV [28], and an AlAs band gap of 3.13 eV. The effective masses in the well and the barriers were taken to be 0.067 and 0.15, for the electrons, 0.087 and 0.15 for the light holes, and 0.62 and 0.76 for the heavy holes, respectively [29]. For the light holes, we also use a two-band model for the barrier wave vector, and for the heavy holes, we use a one-band expression to estimate the wave vector in the barriers. From the theoretical curves in Fig. 2.6, we can see that the tunneling time for electrons is much shorter than that for heavy holes, and the light-hole tunneling time is shorter than that for the electrons.

Comparing these theoretical estimates of the tunneling times with the decay times observed experimentally, we note that the decay times agree well with the calculated tunneling time of the electrons. However, if we expected Eq. 2.5 to explain the data, then we should observe two decay times, a short one near zero delay and a longer time at much longer delays. We might expect the longer decay time to be that for the heavy holes, and perhaps suspect that a much shorter decay time for the electrons is present in the curves of Figs. 2.5(a) and (b), but is not resolved experimentally. This is not the case, and there is no evidence of a faster decay in more detailed scans at smaller delays. In addition, the direct time-resolved photoluminescence data of Tsuchiya et al. [10] show significant photoluminescence intensity at time delays similar to ours, which shows that both the electron and heavy hole densities are still significant after the decay times we measured. Therefore, we conclude that the delay scans we show in Fig. 2.5 are correctly described by Eq. 2.5, but that the electrons and heavy holes escape from the quantum well by tunneling at very similar rates. The tunneling escape times for both electrons and heavy holes are thus given by the decay times shown in Fig. 2.6. The simply-calculated heavy-hole tunneling escape times shown by the dashed line in Fig. 2.6 differ from the experimentally observed heavy hole tunneling escape times by a large factor, which varies from approximately 100 for 16 Å barriers to more than 10^5 for 34 Å barriers. This surprising experimental observation provides an answer to the problem of charge accumulation due to a buildup of holes in the quantum well. If rapidly escaping electrons were to leave the photoexcited holes behind in the quantum well, a net positive charge would accumulate in the well. With the estimated density of approximately 10^{11}cm^{-2} carriers created per pulse, and a laser repetition time T_{rep} of 8 ns, the simply-calculated heavy-hole times shown in Fig. 2.6 would predict enormous accumulations of carriers. Such an accumulation of positive charge would greatly affect the photoluminescence linewidth, and no such broadening is observed. Thus the rapid escape of heavy holes that is experimentally observed resolves the problem of the escape of photoexcited holes, and the hole accumulation that would accompany slow escape of the holes.

This surprising observation of the rapid escape of heavy holes could qualitatively be explained by several phenomena. The most obvious possibility is the effect of accumulated holes on the band profile. An accumulation of heavy holes would result in band bending that would tend to reduce the escape rate for electrons, and increase the escape rate for holes. However, simple estimates of the magnitude of this effect indicate that it is too weak to change the heavy-hole tunneling escape times by the many orders of magnitude required to explain the experimental data. Similarly, transport of accumulated heavy holes due to diffusion in the plane of the quantum well is insufficient to reduce the heavy hole densities by the huge factors required. A physically reasonable explanation for the rapid escape of heavy holes has recently been developed by Yu, Jackson, and McGill [30]. They considered the mixing of the light-hole and heavy-hole bands due to confinement in the quantum well, in order to estimate an average heavy hole tunneling escape time. A simple picture of holes in confined systems shows that heavy- and light-hole subbands are created by confinement in the quantum well, and that their confinement energies can be calculated simply by considering the valence band offset and the appropriate effective masses in the well and the barrier regions. While this approach correctly predicts the maxima of the valence subbands, it neglects the free-particle behavior of the holes in the plane of the quantum well. In Fig. 2.7 we show the valence bands in the quantum well as a function of parallel wavevector $\vec{k}_{||}$, calculated using the 4-band Kohn-Luttinger model [31] of the valence bands, in the spherical approximation. The nonparabolicity of the subbands with increasing parallel wavevector results from interaction between the various subbands. The result of the interaction is that the wavefunctions at nonzero parallel wavevector $\vec{k}_{||}$ for the band labelled "hh1,"

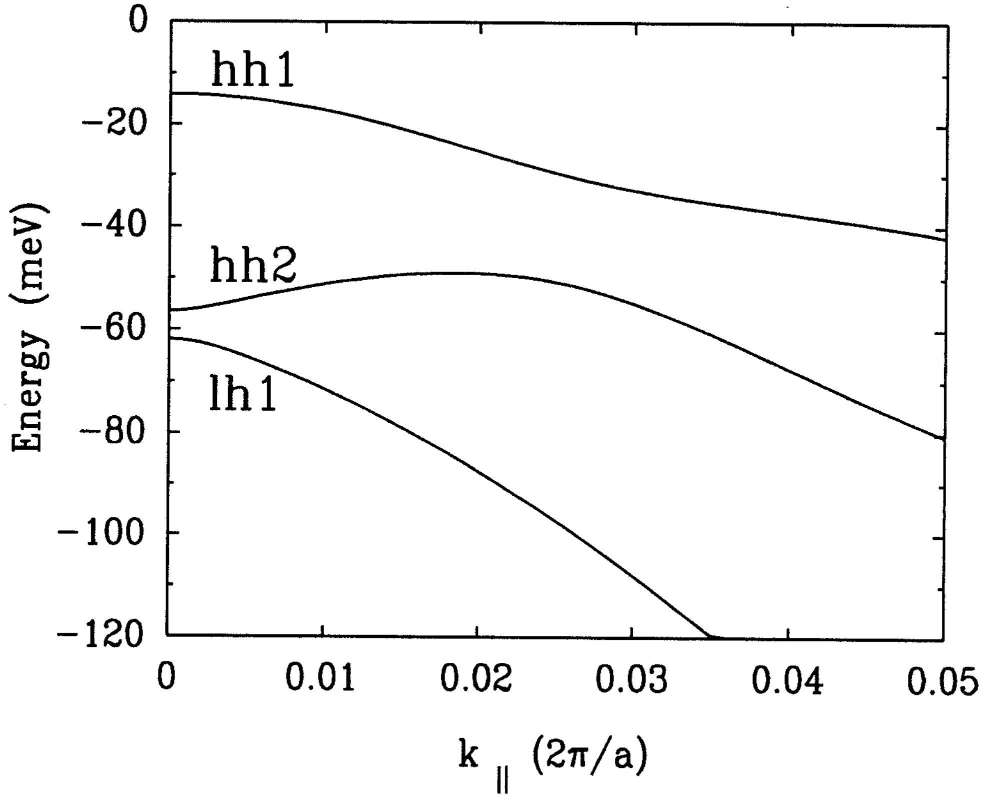

Figure 2.7: Valence subband dispersion in the plane of the quantum well layers, calculated with the Kohn-Luttinger model. Nonparabolicity of the subbands is due to interation among the bands, which results in mixed heavy-hole and light-hole components of the bands for nonzero $\vec{k}_{||}$. After Ref. [30].

and identified as the lowest "heavy-hole-like" subband, consist of components of both light-hole and heavy-hole character.

For any finite population of holes, the lowest heavy-hole-like subband hh1 will be filled to some nonzero parallel wavevector, and therefore holes with nonzero parallel wavevector will have mixed light-hole and heavy-hole character. The wavefunction $|\Psi(\vec{k}_{||})>$ at a particular $\vec{k}_{||}$ can be decomposed as a sum of the zone-center wavefunctions $|\phi_0^{(i)}>$ as

$$|\Psi(\vec{k}_{||})> = \sum_i \alpha_i(\vec{k}_{||})\, |\phi_0^{(i)}>, \tag{2.6}$$

where the sum over i denotes sum over light- and heavy-hole bands, as well as the sum over subband indices. The values of the coefficients $\alpha_i(\vec{k}_{||})$ are calculated using the Kohn-Luttinger model for the valence bands. To estimate the effect that this mixing has on the heavy hole tunneling escape time, Yu et al. [30] calculated an average heavy hole escape time by averaging the escape rates over the entire hole distribution, which was characterized by a total density, and a temperature. The escape rate for a given parallel wavevector was calculated by combining the weighted rates for the constituent wavefunctions from

$$1/\tau(\vec{k}_{||}) \ = \ \sum_i \alpha_i(\vec{k}_{||})\, [1/\tau_0^{(i)}], \tag{2.7}$$

where $[1/\tau_0^{(i)}]$ is the escape rate for the i'th zone-center hole level, calculated using the simple transmission resonance approach described earlier. An average heavy hole tunneling escape time was calculated by averaging Eq. 2.7 over parallel wavevector, assuming a hole distribution characterized by Fermi-Dirac statistics, and a particular total heavy hole density and temperature.

The results of calculations of the average heavy hole tunneling escape time using this approach are shown in Fig. 2.8 for the samples A1 through A5 that showed clear evidence that the decay was dominated by tunneling escape. The

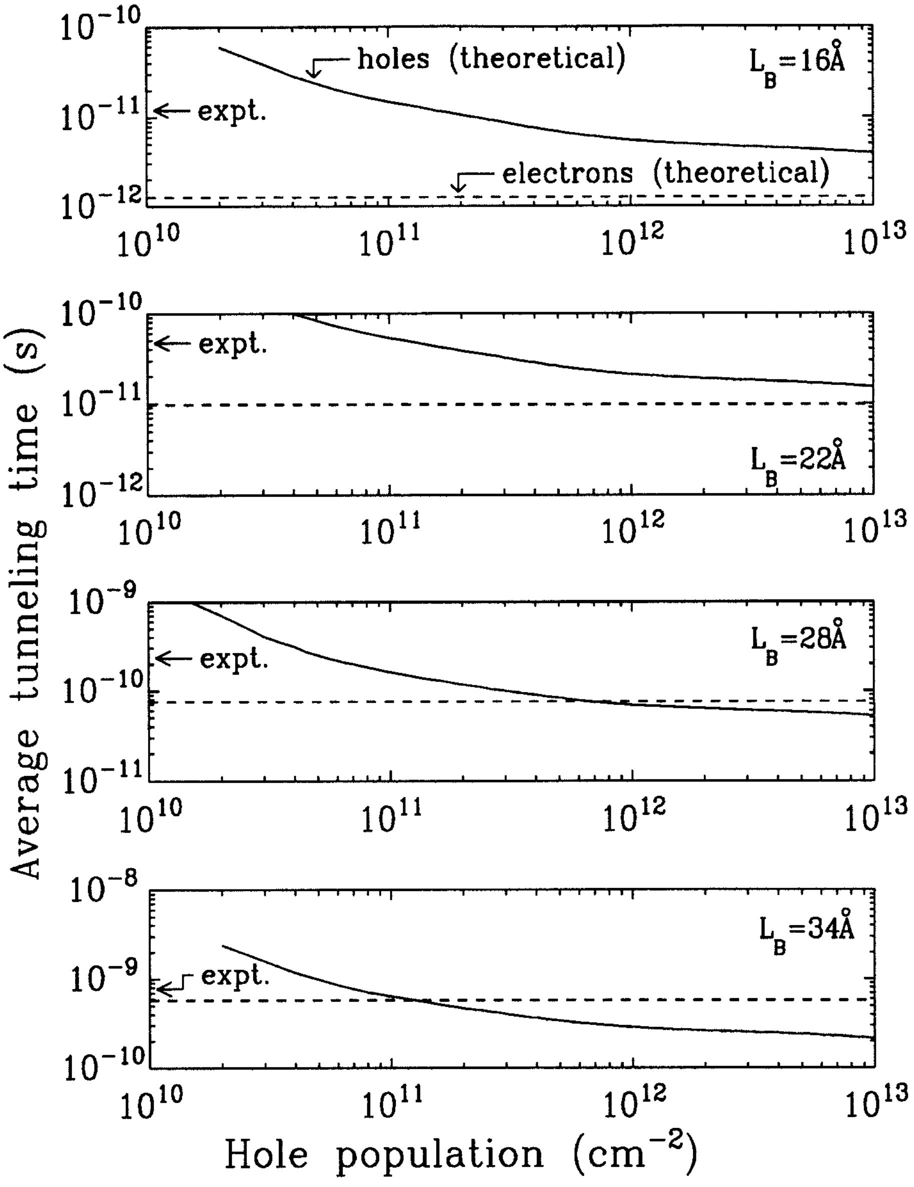

Figure 2.8: Calculated average heavy hole tunneling escape times, for samples A1, A2, A3, and A4, which had barrier thicknesses of 16, 22, 28, and 34 Å, respectively. The average tunneling escape time is shown as a solid line, as a function of the total heavy hole subband occupation density. Also shown for comparison are the calculated electron escape times, shown as dashed lines, and the experimentally observed decay times, which are indicated by the arrows. The estimated heavy hole density in the experiment is approximately 10^{11}cm^{-2}. After Ref. [30].

results shown in Fig. 2.8 were calculated assuming a temperature of 80 K. From Fig. 2.8 it can be seen that the heavy hole escape time decreases with increasing hole density, as the heavy hole band becomes filled to larger parallel wavevector, where mixing with the light hole bands is more important. Because the light hole escape is much faster than the heavy hole escape, the result is a significant decrease in the tunneling escape time, even though the magnitude of the light hole component of the wavefunction is only a few percent. The estimated densities of electrons and heavy holes produced by each optical pulse in our experiment are of the order of $10^{11}\mathrm{cm}^{-2}$. To allow comparison, we also show in Fig. 2.8 the calculated electron escape times, shown as dashed lines, and the experimentally observed decay times, which are indicated by the arrows.

Comparing the results in Fig. 2.8, we can see that for the experimentally estimated excitation density of approximately $10^{11}\mathrm{cm}^{-2}$, the calculated heavy hole, calculated electron, and experimentally observed decay times are all within an order of magnitude of each other. The success of this simple model is striking in view of the fact that it contains no adjustable parameters, and explains the overestimate by a factor of 100 to 10^5 of the heavy hole tunneling escape times obtained from the simple transmission resonance calculation.

As the hole band-mixing effect is expected to be less pronounced for lower temperatures, and lower carrier densities, the results described in Section 2.4.3 might be expected to show the long lifetime of the zone-center heavy holes. The failure to observe the long zone-center heavy hole tunneling time may be attributable to the large excess energy per photoexcited carrier created by the CPM laser excitation at 2 eV. This results in carriers that have initial temperatures well in excess of the lattice temperature, which dominates any effect of changing the sample temperature. However, the observation of the long zone-center heavy hole tunneling time should be possible using a tunable pulsed laser source, operated at an energy sufficiently close to the photoluminescence bandgap that the photoexcited carriers are created with low excess energy. The delay scan shown in Fig. 2.5(c) shows double exponential decay, which may be due to the fact that the sample, C1, has a wider photoluminescence gap due to the increased confinement of electrons and holes in this structure. The excess energy with which the carriers are created is therefore less, which may explain why the two times are observed.

2.6 Comparison with Results in Other Systems

The results of our measurements of tunneling escape times in GaAs/AlAs/-GaAs/AlAs/GaAs double-barrier heterostructures are complementary to other time-resolved studies of double-barrier devices using techniques such as electro-optic sampling or the use of these devices in oscillator circuits. In addition, there have been investigations of tunneling in other structures, such as double quantum wells, using time-resolved photoluminescence. In this section, the results of the various investigations will be compared, to summarize the state of the field at the time of writing.

Tsuchiya et al. [10] were the first to use photoluminescence to study tunneling escape from double-barrier heterostructures. The devices they studied were very similar to those studied in the present work. As mentioned previously, the times we measure at 80 K are a factor of approximately four longer than those found by Tuchiya et al. [10]. However, in Ref. [10] it was assumed that the heavy hole escape was negligible, and that the direct time-resolved photoluminescence decay was only due to escape of electrons from the quantum well. In view of the present work, this assumption is not valid. If, as we found, the escape of electrons and heavy holes occurs at the same rate, then the photoluminescence decay times measured in Ref. [10] should be multiplied by a factor of 2 to obtain the electron and heavy hole escape times. The remaining discrepancy of a factor of approximately 2 between the results of the present work and that of Ref. [10] can be attributed to experimental uncertainty in the barrier thicknesses.

Whitaker et al. were the first to use electrooptic sampling to study GaAs/-AlAs/GaAs/AlAs/GaAs double-barrier heterostructures [8]. They studied a device with a 45 Å quantum well and 15 Å barriers, and obtained a large-signal switching time of 2 ps, although they only measured the transition time in one direction. In a similar study of a double barrier with a 45 Å quantum well and 17 Å barriers, Diamond et al. [9] measured a switching time of 8 ± 2 ps. The difference between the two measurements by electrooptic sampling has not been accounted for, but may be attributable to uncertainties in sample parameters. For the 16 Å barrier sample A1 studied in the present work, a tunneling time of 12 ± 3 ps was obtained. The well width in sample A1 is 58 Å, which is estimated to increase the tunneling escape time for electrons by a factor of 2 compared to an identical sample with a well width of 45 Å. Therefore, we can estimate from the present work that the tunneling escape time in a sample with 16 Å barriers and a 45 Å quantum well would be 6 ps. Thus the time-resolved photoluminescence results in the present work are in reasonable agreement with the electro-optic sampling measurements of Refs. [8] and [9].

Brown et al. [3, 32] have fabricated oscillator circuits using GaAs/AlAs/-GaAs/AlAs/GaAs double barrier heterostructures mounted in waveguides. They observed oscillation at up to 200 GHz for structures with a 45 Å quantum well and 17 Å barriers, and oscillation at up to 420 GHz with 11 Å barriers. The oscillation frequencies for the 17 and 11 Å barrier samples of 200 and 420 GHz correspond to periods of 5 and 2.4 ps, respectively. These times compare well with the times of 6 and 3 ps estimated from the time-resolved photoluminescence measurements in the present work. The exact relationship of the maximum oscillation frequency to the tunneling escape time is not completely clear, however. Brown et al. [33] have suggested a model for the effect of the quasi-bound state lifetime upon the oscillation power that they claim yields quantitative agreement with experiment, using the lifetimes calculated as in Fig. 2.6. However, as can be seen from Fig. 2.6, the calculated electron escape time is faster than the observed decay time by a factor of approximately 10 for the thin barrier samples used in the high-frequency oscillators. This discrepancy between the tunneling times used to accurately predict maximum oscillation power and those measured by photoluminescence has not yet been explained.

Finally, there have been measurements of tunneling in double quantum well structures, using time-resolved photoluminescence [34, 35, 36, 37]. These structures consist of two quantum wells, of differing well widths, separated by barrier layers. Bastard et al. [35] have studied the transfer of photoexcited electrons and holes from one quantum well to another, using a variable electric field to vary the alignment of the confined states in the two wells. They observed resonances in the tunneling due to crossings of the heavy hole level in the narrower quantum well with both the heavy hole and the light hole levels in the wider well. They have suggested that the effects of light and heavy hole mixing are important in the hole transfer in the double quantum well systems. The results of Bastard et al. [35] are in qualitative agreement with the results of the present work, and suggest that the phenomenon of light- and heavy-hole mixing is important in a general class of tunneling problems, as one would expect. However, the results of Ref. [35] have recently been contradicted by Shah et al. [36], who claim that they did not observe any evidence of heavy hole tunneling upon alignment with light hole levels. This result, which directly contradicts the observations of Ref. [35], could be due to a difference in the experimental electron and heavy hole carrier densities. As pointed out by Yu et al. [30] the strength of the light- and heavy-hole mixing is dependent upon the density of heavy holes, and becomes unimportant for sufficiently low carrier densities. Further work on this subject will be required to determine the cause of the discrepancy. Finally we point out that Nido et al. [37] observed hole tunneling times in double quantum well structures that were intermediate to calculations of heavy- and light-hole tunneling times, which is in qualitative agreement with the results of the present work.

2.7 Conclusions

In summary, the tunneling times for electrons and heavy holes to escape from the lowest quasi-bound state in the quantum wells of GaAs/AlAs/GaAs/AlAs/-GaAs double-barrier heterostructures have been measured using photoluminescence excitation correlation spectroscopy (PECS). The electrons and heavy holes are observed to escape at the same rate, at rates similar to the calculated electron escape times, but many orders of magnitude faster than the calculated heavy hole times. The rapid escape of heavy holes can be explained by considering the mixing between light- and heavy-hole bands in the quantum well, which results in much more rapid escape of heavy holes from the quantum well. A detailed understanding of the escape of the photo-excited holes from the quantum well is important to understand the results of all of the measurements reported to date that are based on optical excitation.

References

[1] R. Tsu and L. Esaki, *Appl. Phys. Lett.* **22**, 562 (1973).

[2] T.C.L.G. Sollner, W.D. Goodhue, P.E. Tannenwald, C.D. Parker, and D.D. Peck, *Appl. Phys. Lett.* **43**, 588 (1983).

[3] E.R. Brown, T.C.L.G. Sollner, C.D. Parker, W.D. Goodhue, and C.L. Chen, *Appl. Phys. Lett.* **55**, 1777 (1989).

[4] E.R. Brown, C.D. Parker, L.J. Mahoney, J.R. Söderström, and T.C. McGill, submitted to the Device Research Conference, Santa Barbara, 1990.

[5] T.K. Woodward, T.C. McGill, H.F. Chung, and R.D. Burnham, *IEEE Electron Device Lett.* **9**, 122 (1988).

[6] F. Capasso, K. Mohammed, and A.Y. Cho, *IEEE J. Quantum Electron.* **QE-22**, 1853 (1986).

[7] See Section 1.2.3 of this thesis and references therein.

[8] J.F. Whitaker, G.A. Mourou, T.C.L.G. Sollner, and W.D. Goodhue, *Appl. Phys. Lett.* **53**, 385 (1988).

[9] S.K. Diamond, E. Özbay, M.J.W. Rodwell, D.M. Bloom, Y.C. Pao, E. Wolak, and J.S. Harris, in *OSA Proceedings on Picosecond Electronics and*

Optoelectronics, Vol. 4 of the OSA Proceeding Series, T.C.L.G. Sollner and D.M. Bloom, eds. (Optical Society of America, Washington, D.C., 1989), p. 101.

[10] M. Tsuchiya, T. Matsusue, and H. Sakaki, *Phys. Rev. Lett.* **59**, 2356 (1987).

[11] H. Mahr, A.G. Sagan, C.P. Hemenway, and N.J. Frigo, *Chemical Phys. Lett.* **79**, 503 (1981).

[12] H. Mahr and A.G. Sagan, *Optics Comm.* **39**, 269 (1981).

[13] D. Rosen, A.G. Doukas, Y. Budansky, A. Katz, and R.R. Alfano, *Appl. Phys. Lett.* **39**, 935 (1981).

[14] D. von der Linde, J. Kuhl, and E. Rosengart, *J. Lumin.* **24/25**, 675 (1981).

[15] A. Olsson, D.J. Erskine, Z.Y. Xu, A. Schremer, and C.L. Tang, *Appl. Phys. Lett.* **41**, 659 (1982).

[16] M.B. Johnson, T.C. McGill, and A.T. Hunter, *J. Appl. Phys.* **63**, 2077 (1988).

[17] M.B. Johnson, T.C. McGill, and N.G. Paulter, *Appl. Phys. Lett.* **54**, 2424 (1989).

[18] C.L. Tang, F.W. Wise, M.J. Rosker, and I.A. Walmsley, *IBM J. Res. Develop.* **33**, 447 (1989).

[19] M.J Rosker, Ph.D. thesis, Cornell University, Ithaca, New York, 1987.

[20] D.C. Edelstein, private communication; D.C. Edelstein, Ph.D. thesis, Cornell University, Ithaca, New York, 1990.

[21] C. Doland, W.B. Jackson, and A. Andersson, in *Ultrafast Phenomena V, Proceedings of the Fifth OSA Topical Meeting*, Vol. 46 in the Springer Series in Chemical Physics, G.R. Fleming and A.E. Siegman, eds. (Springer Verlag, Berlin, 1986), p. 86.

[22] K.-K. Choi, B.F. Levine, C.G. Bethea, J. Walker, and R.J. Malik, *Appl. Phys. Lett.* **50**, 1814 (1987).

[23] T. Matsusue and H. Sakaki, *Appl. Phys. Lett.* **50**, 1429 (1987).

[24] C.I. Huang, M.J. Paulus, C.A. Bozada, S.C. Dudley, K.R. Evans, C.E. Stutz, R.L. Jones, and M.E. Cheney, *Appl. Phys. Lett.* **51**, 121 (1987).

[25] N. Harada and S. Kuroda, *Jpn. J. Appl. Phys. Pt. 2* **25**, L871 (1986).

[26] E.O. Kane,"Basic Concepts of Tunneling," in *Tunneling Phenomena in Solids*, E. Burstein and S. Lundqvist, eds. (Plenum, New York, 1969) p. 1.

[27] E.O. Kane, "The $\mathbf{k} \cdot \mathbf{p}$ Method," in *Physics of III-V Compounds, Vol. 1*, A.C. Beer and R.K. Willardson, eds. (Academic, New York, 1966), p. 75.

[28] J. Batey and S.L. Wright, *J. Appl. Phys.* **59**, 200 (1986).

[29] S. Adachi, *J. Appl. Phys.* **58**, R1 (1985).

[30] E.T. Yu, M.K. Jackson, and T.C. McGill, *Appl. Phys. Lett.* **55**, 744 (1989).

[31] J.M. Luttinger and W. Kohn, *Phys. Rev.* **97**, 869 (1955).

[32] E.R. Brown, W.D. Goodhue, and T.C.L.G. Sollner, *J. Appl. Phys.* **64**, 1519 (1988).

[33] E.R. Brown, C.D. Parker, and T.C.L.G. Sollner, *Appl. Phys. Lett.* **54**, 934 (1989).

[34] H.W. Liu, R. Ferreira, G. Bastard, C. Delalande, J.F. Palmier, and B. Etienne, *Appl. Phys. Lett.* **54**, 2082 (1989).

[35] G. Bastard, C. Delalande, R. Ferreira, and H.W. Liu, *J. Lumin.* **44**, 247 (1989).

[36] J. Shah, K. Leo, J.P. Gordon, T.C. Damen, D.A.B. Miller, J.E. Cunningham, and C.W. Tu, talk **K-19-6** at the Meeting of the American Physical Society, Anaheim, March 12-16, 1990.

[37] M. Nido, M.G.W. Alexander, W.W. Rühle, T. Schweizer, and K. Köhler, *Appl. Phys. Lett.* **56**, 355 (1990).

Chapter 3

X-point Escape of Electrons from the Quantum Well of a Double-Barrier Heterostructure

3.1 Introduction

3.1.1 Background

In this chapter we will consider the effect of the indirect conduction band minima in AlAs upon the escape of photoexcited electrons from the quantum well of a double-barrier heterostructure. At a GaAs/AlAs interface the valence band edge in GaAs is approximately 0.55 eV higher than the valence band edge in AlAs [1]. In both materials, the valence band maximum occurs at the Brillouin zone center, which is referred to as the Γ-point. The low temperature direct bandgaps of 1.52 and 3.13 eV for GaAs and AlAs, respectively [2], place the Γ-point conduction band edge in the GaAs approximately 1.07 eV below that in AlAs. Since this confines electrons to the GaAs layers, the lowest energy electron states in GaAs/AlAs heterostructures will normally be derived mainly from the bulk GaAs Γ-point wavefunctions. This justifies use of a simple effective mass model of the GaAs bulk conduction band structure in calculations of heterostructure properties. However, the appropriate model in a heterostructure for the bulk AlAs is not as obvious; the band structure of bulk AlAs is indirect. The AlAs conduction band has multiple minima, located at the X-point, which is a point on the edge of the Brillouin zone in the (001) and equivalent directions. Despite the fact that AlAs is an indirect material, much of the work on tunneling in the GaAs/AlAs material system has ignored the indirect nature of AlAs, characterizing the conduction band only by the zone center (Γ-point) effective mass and potential energy [3]. This approach has been successful in describing many of the physical effects observed in heterostructures fabricated with the GaAs/AlAs system, particularly when the effects of confinement on the electrons are not great [3]. However, the X-point conduction band minima play an important or dominant role in several heterostructures. We will discuss examples of some of these devices in the following paragraph.

The first example of a structure in which the X-point conduction band minima are important is the short period GaAs/AlAs superlattice, a structure that has been extensively studied both theoretically [4]-[7] and experimentally [8]-[14] as a possible alternative to $Al_xGa_{1-x}As$ alloys. In these short period superlattices, localization of the electrons at the Γ-point in the GaAs layers can cause confinement energies large enough to result in interaction with the AlAs X-point, and it is possible, with sufficient confinement, to obtain a superlattice whose lowest conduction band states are derived mainly from the AlAs X-point [5]. Another structure in which the indirect nature of AlAs is important is the double quantum well, where the X-point levels can contribute to nonresonant tunneling from one well to another [15]. In GaAs/AlAs double-barrier heterostructures it has been suggested [16] that the valley current is determined by currents through the X-point levels in the AlAs barriers. In the tunnel emitter bipolar transistor, the process of injection of hot electrons through a thick AlAs emitter barrier is central to operation of the device [17]. The importance of the X-point levels in the emitter barrier of such structures has not been discussed, and could be very significant to the injection process for electrons. There has also been experimental evidence of X-point related resonances in the current-voltage characteristics of double-barrier [18, 19, 20] and single-barrier [21, 22] devices.

From the examples discussed above, it is clear that there are a wide variety of devices in which the indirect X-point conduction band minima of AlAs are important, particularly in electron tunneling through AlAs barriers. Studies of the escape of photoexcited carriers in GaAs/AlAs/GaAs/AlAs/GaAs double-barrier heterostructures such as those described in Ref. [23] and Chapter 2 of this thesis, have shown that photoluminescence is a powerful technique for studies of tunneling. In these previous studies, however, the confinement of the quantum well states was not sufficient to enable interaction with the X-point levels in the AlAs layers. In contrast, in the work described in this chapter, we have used photoluminescence to study structures in which the interaction of electrons escaping from the quantum well with the X-point levels in the barriers is important. To illustrate the structures studied, we show in Fig. 3.1 the conduction band diagrams for two representative undoped GaAs/AlAs/GaAs/AlAs/GaAs heterostructures. The Γ-point and X-point conduction band edges are shown as a function of position as the solid, and light gray lines, respectively. The Γ-point profile is the familiar double barrier potential, whereas for the X-point the inversion of the relative band offset leads to the double well potential for the conduction band edge. The energies of the lowest Γ-point level, localized in the GaAs quantum well, and the lowest X-point levels, localized in the two AlAs barriers, are schematically

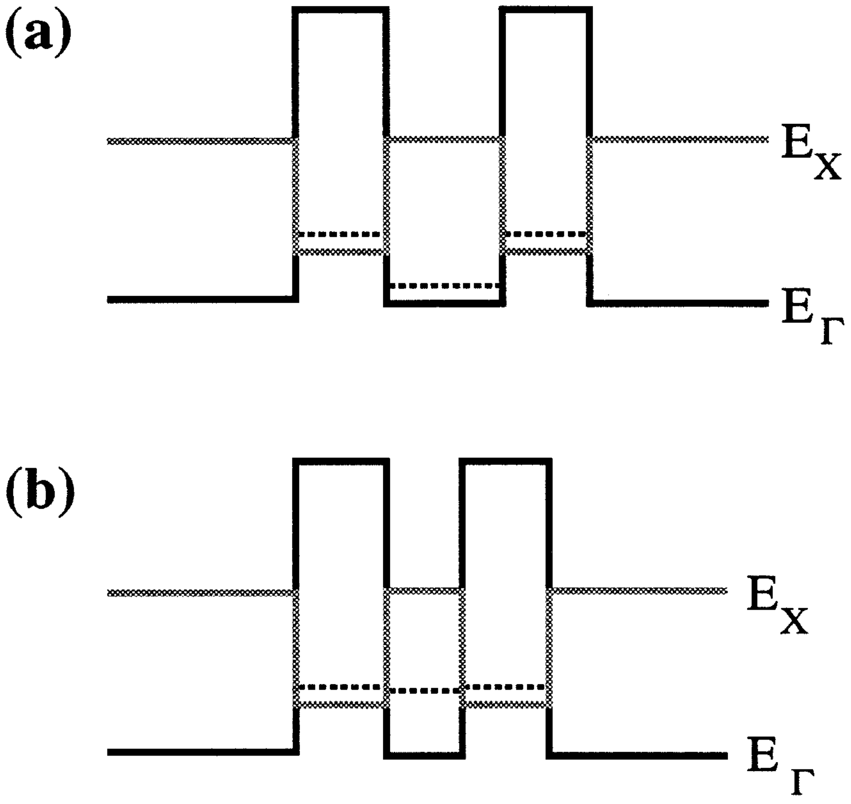

Figure 3.1: Conduction band edges at the Γ-point (dark line) and X-point (gray line) versus position for two GaAs/AlAs/GaAs/AlAs/GaAs double-barrier heterostructures with differing quantum well widths. The position in energy of the lowest Γ-point and X-point states are schematically shown with dashed lines. (a) Wide quantum well, where the Γ-point state in the quantum well lies below the energy of the X-point levels in the barriers. (b) Narrow quantum well, where Γ-point and X-point states are at comparable energies.

shown as dashed lines. In Fig. 3.1(a) we show the band diagram for a structure with a fairly wide quantum well. In this structure, the confinement of the Γ-point levels in the GaAs is insufficient to allow interaction with the X-point levels in the barriers. However, if the quantum well width is decreased, as shown in Fig. 3.1(b), the confinement energy for the Γ-point level in the GaAs quantum well is increased. In the case illustrated in Fig. 3.1(b), the confinement raises the Γ-point state in the quantum well to an energy nearly equal to that of the X-point levels in the barriers.

The effect of the X-point levels on the escape process for electrons initially created in the Γ-point states in the quantum well could be considerable, and could lead to novel behavior during escape. To illustrate this, we show in Fig. 3.2 calculations using the one-band Wannier orbital model (OBWOM) [5], of the escape of electrons initially localized in the the quantum well, for two different GaAs/AlAs/GaAs/AlAs/GaAs double-barrier heterostructures. The one-band Wannier orbital model describes the conduction band structure of both the GaAs and AlAs materials with a single orbital per unit cell, considering overlap of orbitals over distances of several unit cells. This model allows a realistic while computationally efficient calculation of the conduction band structure, including the behavior at the X-point [5]. The calculations presented in Fig. 3.2 show two examples of the evolution of the probability density integrated over the quantum well region, for an electron wavefunction initially localized in the GaAs quantum well. In Fig. 3.2(a) we show the behavior for a structure with a 15 monolayer GaAs quantum well, and 10 monolayer AlAs barriers. This structure corresponds to the situation illustrated in Fig. 3.1(a), where the effect of the X-point levels is small. The decay of the initial wavefunction localized in the well can be described by a simple exponential. The time constant for the decay corresponds to the quasi-bound state lifetime, which can be calculated [24] from the energy

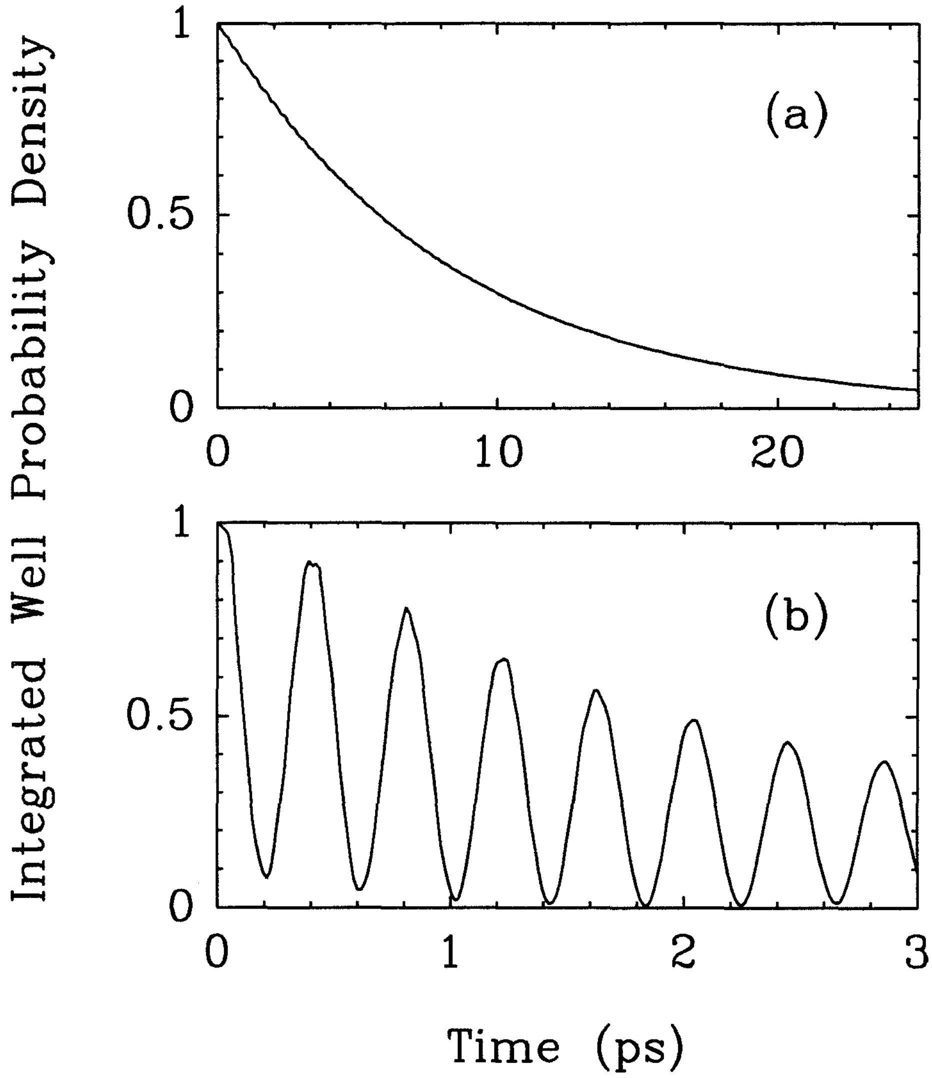

Figure 3.2: Calculated decay of the probability density, integrated over the quantum well region, for an electron initially localized in the quantum well of two different GaAs/AlAs/GaAs/AlAs/GaAs heterostructures. (a) 15 monolayer quantum well, 10 monolayer barriers. The evolution is described by a simple exponential, with a time constant corresponding to the quasi-bound state lifetime. (b) 12 monolayer quantum well, 10 monolayer barriers. In this case interaction with the X-point levels causes oscillations in the probability density during decay of the quasi-bound state.

width of the transmission resonance, $\Delta E_{\rm FWHM}$, using the uncertainty relation $\tau = \hbar/\Delta E_{\rm FWHM}$, as described in Section 2.5. In Fig. 3.2(b) we show a similar calculation for a structure with a 12 monolayer GaAs quantum well, and 10 monolayer AlAs barriers. In this structure, the X-point and Γ-point levels are close in energy, and the evolution is very different. The decay of the probability density in the quantum well shows oscillations during the decay process, due to coupling between the Γ-point levels in the GaAs quantum well, and the X-point levels in the AlAs barriers. This example shows that the interaction between the X-point levels and the Γ-point levels in the double-barrier heterostructure can lead to qualitatively different phenomena from the case where the X-point levels are much higher in energy than the Γ-point levels.

In this chapter we describe an experimental study of the effect of the X-point levels localized in the AlAs barriers upon the escape of electrons photoexcited in the quantum well. In a series of GaAs/AlAs/GaAs/AlAs/GaAs double-barrier heterostructures with varying well thicknesses, we have been able to study the transition from the situation illustrated in Fig. 3.1(a), where the effect of the X-point levels is small, to the case in Fig. 3.1(b), where the X-point levels are important.

3.1.2 Summary of Results

We have used photoluminescence to study a series of GaAs/AlAs/GaAs/-AlAs/GaAs double-barrier heterostructures. We report the first observation in these structures of photoluminescence from the recombination of electrons at X-point levels localized in the AlAs barriers, with heavy holes localized in the GaAs quantum well. The integrated photoluminescence intensity from levels localized in the GaAs quantum well decreases dramatically as the Γ-point confinement energy is increased. This decrease is attributed to rapid escape of electrons from the quantum well via X-point states in the AlAs barriers.

3.1.3 Outline of Chapter

In Section 3.2, we describe the sample parameters, details of the sample preparation, and the photoluminescence experimental techniques. In Section 3.3 we present the experimental results, and discuss their interpretation. A summary of our conclusions is given in Section 3.4.

3.2 Experimental Techniques

Samples were grown at 600°C by molecular beam epitaxy (MBE) in a Perkin Elmer 430 system, on (100) GaAs substrates. After growth of a $0.5\,\mu$m GaAs layer, the symmetrical GaAs/AlAs/GaAs/AlAs/GaAs double-barrier heterostructure was grown. The thickness of the final GaAs cap layer was 300 Å. Nominal layer thicknesses, based on bulk growth rate measurements, are shown in Table 3.1 for the 9 samples studied. The GaAs growth rate was determined for each sample by measurement of the total film thickness. The AlAs growth rate was calibrated using reflection high energy electron diffraction (RHEED) oscillations. The nominal quantum well thickness ranges from 9.4 to 20.6 monolayers, and the barrier thicknesses were maintained constant at 13.0 monolayers for all of the samples except for sample 9, in which the barriers were nominally 11.9 monolayers thick. All layers were undoped, with an estimated residual carbon acceptor concentration of $10^{14}\,\mathrm{cm}^{-3}$.

During the course of this work, it was found that details of the MBE growth techniques used were important to the photoluminescence characteristics of the devices. Initial devices were grown with 1 minute growth interrupts at each

Sample No.	Growth No.	Well (ML)	Barrier (ML)	Peak (meV)	FWHM (meV)	Assignment
1	III-342	9.4	13.0	1776	8	X
				1853	20	Γ
2	III-332	10.7	13.0	1757	6	X
				1800	17	Γ
3	III-335	11.8	13.0	1751	6	X
				1779	12	Γ
4	III-331	12.7	13.0	1774	12	Γ-X
5	III-339	13.1	13.0	1724	8	Γ
6	III-341	14.0	13.0	1711	7	Γ
7	III-329	15.8	13.0	1690	6	Γ
8	III-336	16.8	13.0	1667	5	Γ
9	III-059	20.6	11.9	1625	5	Γ

Table 3.1: Sample parameters, observed photoluminescence peak energies at 5 K, and assignment of observed peaks. The nominal layer thicknesses shown for the GaAs quantum well were determined from bulk growth rates determined from measurements of the total film thickness for each sample. The AlAs layer thicknesses were obtained from growth rates calibrated using RHEED oscillations. The assignment of the peaks to transitions involving Γ-point or X-point electron levels is discussed in the text.

interface, in an As overpressure. Studies of these structures, showed photoluminescence spectra with two peaks. The two peaks, separated by approximately 8 meV, were consistent with excitonic luminescence, and luminescence involving impurities. The lower energy peak was found to saturate with increasing pump intensity, appearing in some cases only as a weak shoulder. The saturation, spectral dependence, and energy separation from the exciton peak are all consistent with previous reports of recombination involving impurities in GaAs quantum wells [26]. The origin of the impurity-related level was correlated to the use of growth interrupts, which is consistent with the recent conclusions of Köhrbrück et al. [25]. The nonradiative center has not been identified, but may be related to carbon, as suggested in Ref. [26], or oxygen [27]. Accordingly, for all of the samples described in the present work, growth interrupts were not used. The procedure used to outgas the Al source material after loading into the MBE was also found to be very important to the photoluminescence efficiency of the samples. When the Al source material is replaced, it is subsequently outgassed at 1130°C for 6 hours (corresponding to growth of approximately 8 μm of AlAs). This procedure allows growth of devices with high photoluminescence efficiency. However, it was found that the photoluminescence efficency was severely degraded when using an Al source that had been outgassed, exposed to atmosphere, and subsequently outgassed as described above. Further outgassing for 4 hours at a higher temperature of 1170°C was necessary, corresponding to growth of approximately 12 μm of AlAs, before double-barrier heterostructures with high photoluminescence efficiency could be grown. The increased requirement for outgassing in the latter case is attributed to the increased surface area of the Al source material, due to wetting of the effusion cell crucible.

CW photoluminescence experiments were performed at 5 K, in a helium immersion dewar with sapphire windows. The 5145 Å line from an argon laser was used for photoexcitation, and luminescence was dispersed with a double-pass spectrometer and detected with a GaAs photomultiplier tube and photon-counting electronics.

3.3 Results and Discussion

In Fig. 3.3 we show typical photoluminescence spectra, taken at 5 K, for three representative samples. Fig. 3.3(a) shows the spectrum for sample 7, which has a nominal quantum well width of 15.8 monolayers. A single, narrow peak, centered at 1690 meV, with a FWHM of 6 meV, is observed. Shown in Fig. 3.3(b) is the spectrum for sample 5, which has a quantum well width of 13.1 monolayers. The photoluminescence from this sample also shows a single peak, now centered at 1724 meV, with a width of 8 meV. The spectrum for sample 1, which has the narrowest quantum well width of 9.4 monolayers, is shown in Fig. 3.3(c). This spectrum shows two peaks of comparable intensity. The peak at 1776 meV has a FWHM of 8 meV, whereas the peak at 1853 meV has a FWHM of 20 meV. The intensities of the photoluminescence signals shown in Fig. 3.3 differ considerably, decreasing rapidly with decreasing well width. The spectrum shown in Fig. 3.3(c) is very weak, and extraneous signals from the sapphire dewar windows at 1790 and 1786 meV obscure the photoluminescence from the double-barrier sample. The gap in the spectrum shown in Fig. 3.3(c) is due to this interference. The background seen in Fig. 3.3(c) is due to hot-carrier luminescence from the undoped GaAs cap and buffer layers. Other samples show spectra similar to one of the three cases shown in Fig. 3.3. A summary of the peak energies and widths seen in photoluminescence is given in Table 3.1. For samples 1 to 3, two peaks in the photoluminescence are observed, whereas for samples 4 through 9 only single peaks are seen. It can be seen from Table 3.1 that the lower energy peaks

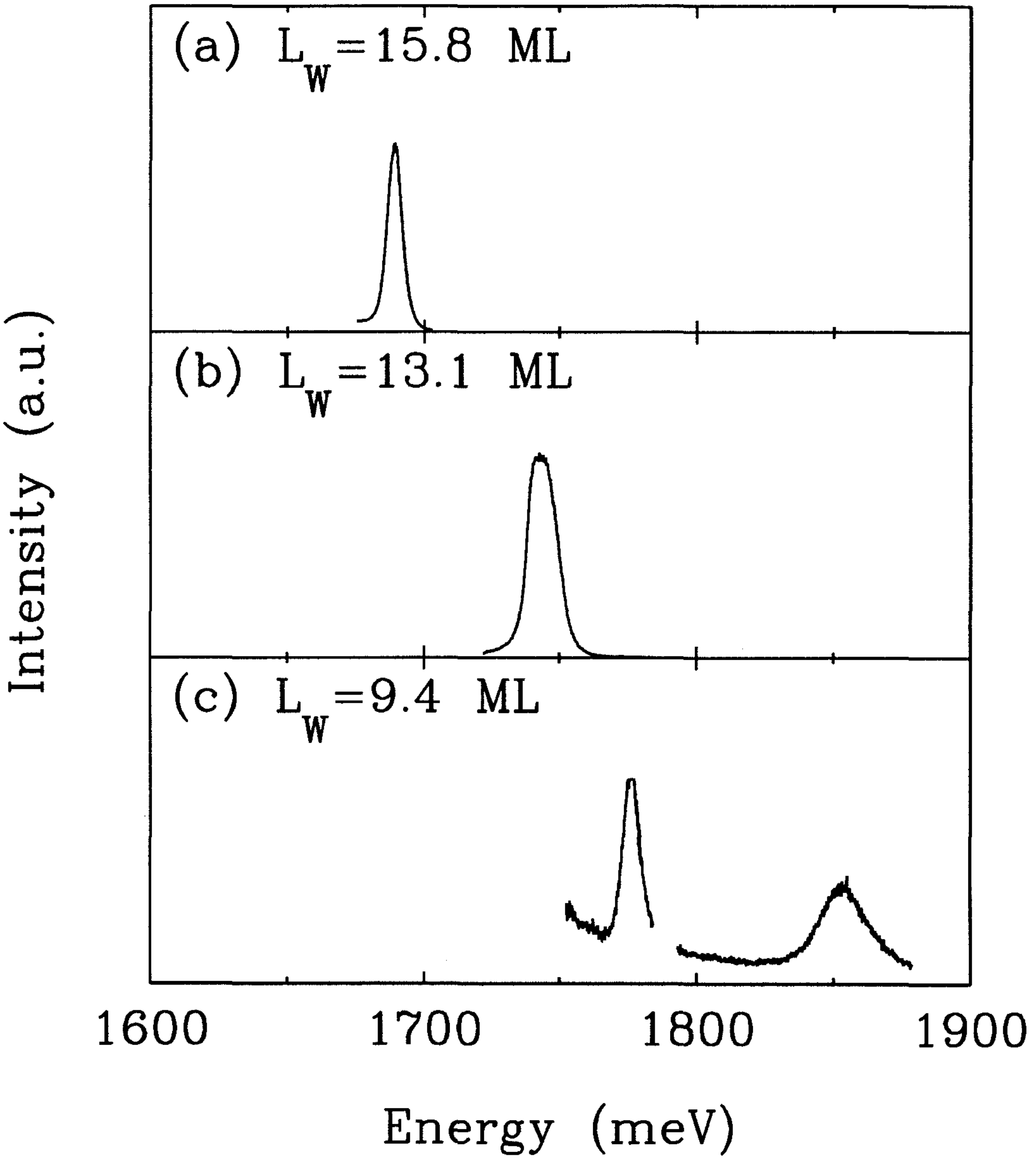

Figure 3.3: Typical photoluminescence spectra at 5 K. (a) Sample 7, with quantum well thickness L_W=15.8 monolayer. (b) Sample 5, L_W=13.1 monolayer. (c) Sample 1, L_W=9.4 monolayers. Interference from impurities in the sapphire dewar windows prevents observation of the photoluminescence at approximately 1788 meV, and is responsible for the gap in the spectrum shown in (c).

observed in samples 1-3 are all a factor of approximately 2.5 narrower than the higher energy peaks in the same samples.

In Fig. 3.4(a) we plot the energies of the peaks in the photoluminescence spectra, as a function of the quantum well thickness. The appearance of a second peak for quantum well widths less than approximately 12.7 monolayers suggests the importance of another electron or hole state in the photoluminescence. To allow comparison of the experimental results with theory, in Fig. 3.4(b) we show the energies for conduction band to lowest heavy hole (hh_1) transitions, calculated using the one-band Wannier orbital model (OBWOM). The Γ-point conduction band edge in the GaAs was adjusted to lie 190 meV below the X-point band edge in AlAs for these calculations, to obtain agreement with the experimentally observed crossover point seen in Fig. 3.4(a). This value of 190 meV agrees well with the value of 160 meV found in Ref. [28]. Energies of the lowest Γ-point ($\Gamma_1 hh_1$), lowest X-point ($X_1 hh_1$), and first excited X-point ($X_2 hh_1$) transitions to the lowest heavy hole state are labelled. Transitions involving electron states with significant (greater than 5% of the total) probability density in the quantum well are indicated in Fig. 3.4(b) by "×" symbols, and those involving significant density in the barriers by "+" symbols. Mixed states with significant probability density in both the well and the barriers are denoted by both symbols.

The origin of the observed peaks can be understood by comparing the experimental data of Fig. 3.4(a) with the calculated energies shown in Fig. 3.4(b). For samples 5 through 9, which have quantum wells wider than 12.7 monolayers, the luminescence is consistent with the $\Gamma_1 hh_1$ recombination, involving electrons and holes both localized in the quantum well. The linewidths of the peaks in these samples, given in Table 3.1, are consistent with monolayer fluctuations in the quantum well width. The higher energy peaks in samples 1 to 3, which have quantum wells narrower than 12.7 monolayers, are also consistent with $\Gamma_1 hh_1$ re-

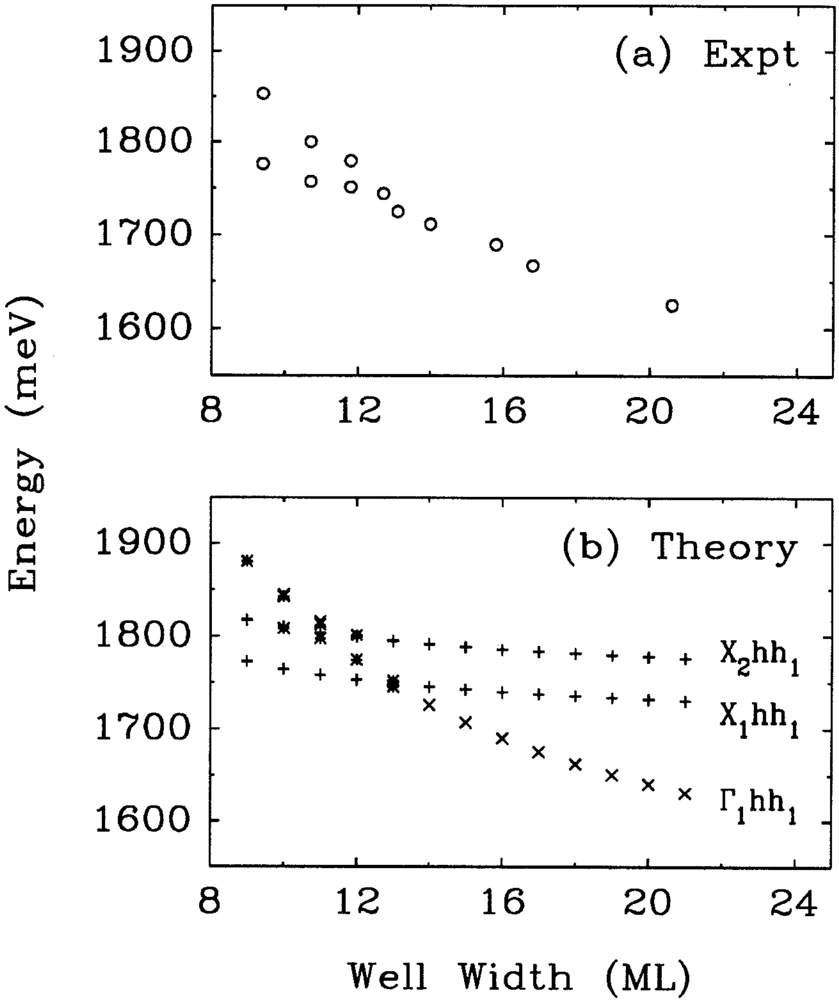

Figure 3.4: (a) Photoluminescence peak energies at 5 K. The lower energy peaks observed for L_W<12.7 monolayers are due to recombination of electrons localized at X-point levels in the AlAs with heavy holes localized in Γ-point states in the GaAs quantum well. (b) Calculated energies of the lowest Γ-point state Γ_1, lowest X-point state X_1, and first excited X-point state X_2 to lowest heavy hole (hh_1) transitions. Transitions involving electron states with significant (greater than 5%) probability density in the quantum well are shown by "×" symbols, and states with significant density in the barriers by "+" symbols.

combination, with a linewidth consistent with monolayer fluctuations in quantum well width. The lower energy peaks seen in Fig. 3.4(a) for $L_W<12.7$ monolayers are consistent with the X_1hh_1 transitions, which involve electrons at X-point levels in the AlAs barriers and heavy holes in the GaAs quantum well. The rising energy of the X-point peaks with decreasing well width is due to increasing confinement of the heavy holes. The identification of the lower energy peaks for narrow well widths with X-point-related luminescence is supported by the widths of the photoluminescence peaks shown in Table 3.1. The photoluminescence peaks observed for the X-point levels are narrower than those involving Γ-point levels. This is due to the reduced impact of monolayer fluctuations in the AlAs barrier thickness on the confinement energy of the X-point levels, which is much smaller than the confinement energy of the Γ-point levels. The X-point-related luminescence is the first observation, in GaAs/AlAs/GaAs/AlAs/GaAs double-barrier heterostructures, of recombination that is indirect in real space and momentum. The X-point levels involved in this recombination are quasi-bound states, in contrast with the X-point levels observed in indirect recombination in GaAs/AlAs short period superlattices [8]-[14]. The X-point levels in the superlattices are the lowest energy electron states, and the observation of luminescence from these levels is indicative of the long lifetime for electrons localized in X-point states. In contrast, the X-point levels in our structures correspond to quasi-bound states in the AlAs barriers, and would not be expected to have a lifetime long enough to enable significant recombination with Γ-point heavy hole levels in the GaAs quantum well. Observation of the weak luminescence from these levels suggests that electrons localized at the X-point levels in the AlAs barriers have some Γ-point character, although a radiative recombination involving emission of a phonon is an alternative explanation. Sample 4, which is situated at the crossover of the Γ and X-point electron levels may show mixed Γ-X character.

The peak assignments for all of the samples are summarized in Table 3.1.

In Fig. 3.5 we show the integrated photoluminescence intensity at 5 K for all of the samples, observed under identical conditions with a pump intensity of 800 W/cm^2. The intensity of the Γ-point peaks are shown in Fig. 3.5 by "×" symbols, and the X-point-related peaks by "+" symbols. The integrated intensity of the Γ-point peaks shows little variation as the quantum well thickness is decreased from 20.5 monolayers to approximately 16 monolayers, and then drops rapidly with further decrease in well width. A change in the rate of decrease of intensity with well width can be seen for the samples with L_W<12.7 monolayers. The drop in integrated intensity for narrower quantum wells is quite dramatic, with a total drop of more than 5 orders of magnitude over the entire range of well thicknesses. The intensity of the X-point peaks is less than that of the Γ-point peaks in all of the samples, but from Fig. 3.5 it can be seen that the X-point peaks become relatively more intense as the quantum well width is reduced.

The integrated photoluminescence intensity shown in Fig. 3.5 depends upon the electron and heavy hole tunneling escape times, the optical absorption, and the radiative recombination rate. In principle, all of these parameters are dependent upon the quantum well width, and could contribute to the variation of photoluminescence intensity with well width seen in Fig. 3.5; we will examine the importance of the various parameters to show why variation in the electron escape time is the most important contribution. First, we consider the absorption. With the 2.4 eV excitation energy used, several transitions between confined electron and hole states contribute to absorption. Decreasing quantum well width will result in a decrease in absorption at the exciting laser energy, because of the increasing energy of the absorption threshold. This will tend to decrease the photoluminescence intensity with decreasing quantum well width. Calculations of the direct allowed absorption processes for the range of quantum well widths

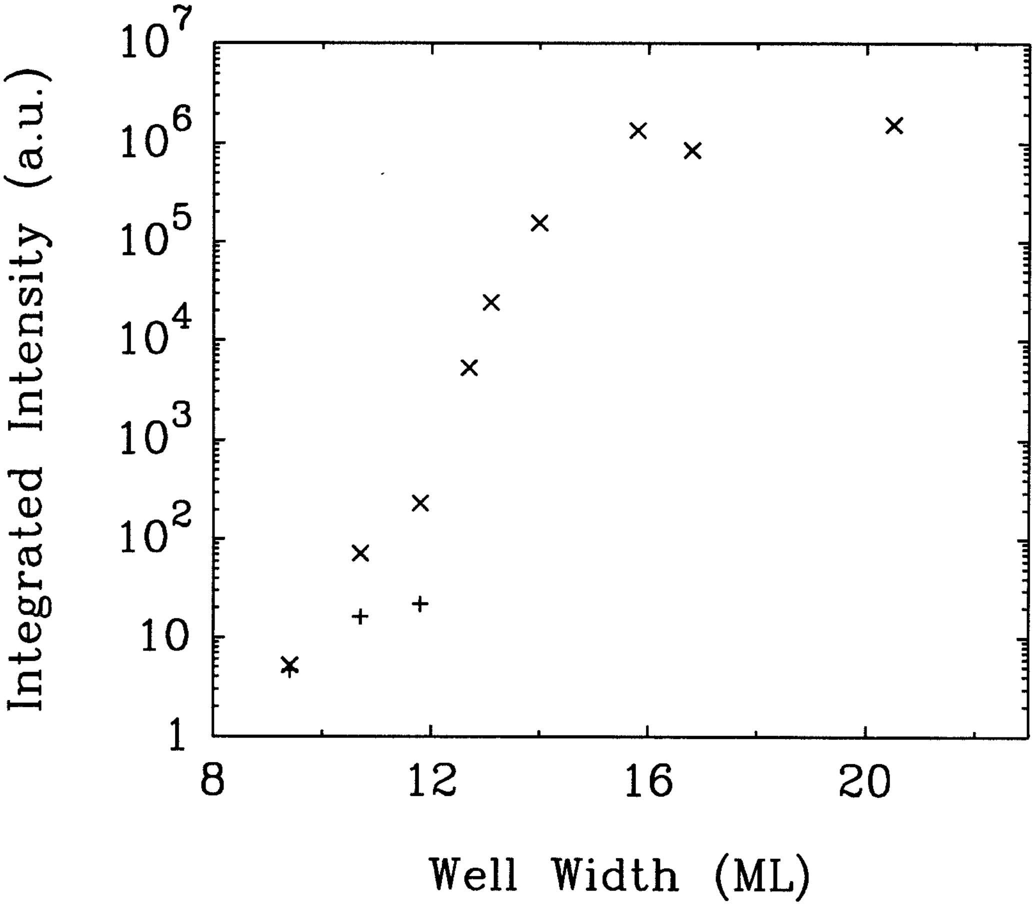

Figure 3.5: Integrated photoluminescence intensity under identical conditions, at 5 K. The intensities of the Γ-point luminescence are shown with "×" symbols, and the X-point intensities as "+" symbols. The drop in intensity with decreasing well width is attributed to rapid escape of photoexcited electrons from the quantum well, via the X-point levels in the AlAs barriers.

covered in Fig. 3.5 show that the $\Gamma_1 hh_1$ and $\Gamma_1 lh_1$ transitions are energetically allowed over the entire range of well widths. The $\Gamma_2 hh_2$ transition is allowed for $L_W > 12$ ML, and the $\Gamma_2 lh_2$ transition is allowed for $L_W > 16$ ML. Measurements of the absorption in wide GaAs quantum wells have shown that the band-to-band absorption is approximately independent of well width [29], and that the absorption contribution for a given subband does not depend strongly upon the excess energy of the incoming photon. Therefore, the dependence of absorption upon well width is due mostly to the number of allowed subbands participating in the absorption. This is not expected to affect the absorption by more than a factor of 2-4 over the range of quantum well widths considered here, and therefore is not a major effect. Next we consider the radiative transition rate. Masselink et al. [29] measured the exciton oscillator strengths in wide GaAs quantum wells, and found that the oscillator strength depends upon well width L_W approximately as $1/(L_W)^2$. Over the range of well widths considered in Fig. 3.5 this results in variation by a factor of approximately 5, which is fairly small, and would lead to increased photoluminescence intensity for narrower quantum wells. Since the observed intensity shows the opposite behavior, i.e., it decreases for narrow wells, we can conclude that the radiative recombination rate is not the dominant effect responsible for the drop in photoluminescence intensity for narrow quantum wells seen in Fig. 3.5. Therefore, the drop in photoluminescence intensity seen in Fig. 3.5 is due to the rapid escape of either electrons or heavy holes. As described in Chapter 2, the escape of heavy holes from double-barrier structures is affected by valence band mixing, and depends upon several parameters, including the barrier thickness, population, and carrier temperature. The light- and heavy-hole escape times are expected, based on a calculation of the transmission resonance width ΔE_{FWHM} and the expression $\tau = \hbar/\Delta E_{FWHM}$ (described in detail in Section 2.5) to smoothly decrease with decreasing quantum well width.

Similarly, no abrupt changes in the population, which is dependent upon the absorption, or the carrier temperature are expected with varying well width. In contrast, the behavior shown in Fig. 3.5 is not smoothly dependent upon the well width, and shows a pronounced change at a quantum well width of approximately 14 monolayers. Having estimated that the absorption, radiative recombination rate, and heavy hole tunneling escape time cannot explain the dependence of the photoluminescence intensity upon the quantum well width, we conclude that the most important contribution is the rapid escape of electrons in structures with narrow quantum wells. Comparing the crossover of Γ-point and X-point energy levels shown Fig. 3.4(a) to the photoluminescence intensity shown in Fig. 3.5, we see that the drop in photoluminescence intensity occurs at a well width of approximately 14 monolayers, which is slightly greater than the well width for crossover of Γ-point and X-point levels, which is 13 monolayers. This indicates that even before the Γ-point state lies higher in energy than the X-point state, the X-point levels influence escape from the quantum well. This may be due to thermal effects, in which carriers with excess kinetic energy escape through the X-point levels, or mixing between the Γ-point and X-point levels.

3.4 Conclusions

We have studied a series of GaAs/AlAs/GaAs/AlAs/GaAs double-barrier heterostructures with varying quantum well widths, using photoluminescence. We report the first observation in these structures, of recombination that is indirect in both momentum and real space, involving electrons localized at X-point levels in the AlAs barriers with heavy holes localized at Γ-point levels in the GaAs quantum well. This luminescence involves X-point quasi-bound states, in contrast to previous observations of indirect luminescence in GaAs/AlAs short period superlattices. Studies of the photoluminesence intensity show a dramatic drop as the quantum well width is decreased. This drop is attributed to the rapid escape of electrons from the quantum well, involving the X-point levels in the AlAs barriers.

References

[1] J. Batey and S.L. Wright, *J. Appl. Phys.* **59**, 200 (1986).

[2] *Landolt-Börnstein: Numerical Data and Functional Relationships in Science and Technology*, edited by O. Madelung and H. Weiss, Vol. III/17(a), (Springer-Verlag, Berlin, 1982), pgs. 164, 218.

[3] B. Ricco and M.Y. Azbel, *Phys. Rev. B* **29**, 1970 (1984), and references therein.

[4] J. Ihm, *Appl. Phys. Lett.* **50**, 1068 (1987).

[5] D.Z.-Y. Ting and Y.-C. Chang, *Phys. Rev. B* **36**, 4359 (1987).

[6] M.A. Gell, D. Ninno, M. Jaros, D.J. Wolford, T.F. Keuch, and J.A. Bradley, *Phys. Rev. B* **35**, 1196 (1987).

[7] Y.-T. Lu and L. Sham, *Phys. Rev. B* **40**, 5567 (1989).

[8] P. Dawson, B.A. Wilson, C.W. Tu, and R.C. Miller, *Appl. Phys. Lett.* **48**, 541 (1986).

[9] D.J. Wolford, T.F. Kuech, J.A. Bradley, M.A. Gell, D. Ninno, and M. Jaros, *J. Vac. Sci. Technol. B* **4**, 1043 (1986).

[10] E. Finkman, M.D. Sturge, and M.C. Tamargo, *Appl. Phys. Lett.* **49**, 1299 (1986).

[11] G. Danan, B. Etienne, F. Mollot, R. Planel, A.M. Jean-Louis, F. Alexandre, B. Jusserand, G. Le Roux, J.Y. Marzin, H. Savary, and B. Sermage, *Phys. Rev. B* **35**, 6207 (1987).

[12] F. Minami, K. Hirata, K. Era, T. Yao, and Y. Masumoto, *Phys. Rev. B* **36**, 2875, (1987).

[13] M.-H. Meynadier, R.E. Nahory, J.M. Worlock, M.C. Tamargo, J.L. de Miguel, and M.D. Sturge, *Phys. Rev. Lett.* **60**, 1338 (1988).

[14] K.J. Moore, P. Dawson, and C.T. Foxon, *Phys. Rev. B* **38**, 3368 (1988).

[15] M.G.W. Alexander, M. Nido, K. Reimann, W.W. Rühle, and K. Köhler, *Appl. Phys. Lett.* **55**, 2517 (1989).

[16] L.F. Luo, R. Beresford, W.I. Wang, and E.E. Mendez, *Appl. Phys. Lett.* **24**, 2133 (1989).

[17] A.F.J. Levi, R.N. Nottenburg, Y.K. Chen, and J.E. Cunningham, *Appl. Phys. Lett.* **54**, 2250 (1989).

[18] A.R. Bonnefoi, D.H. Chow, T.C. McGill, R.D. Burnham, and F.A. Ponce, *J. Vac. Sci. Technol. B* **4**, 988 (1986).

[19] A.R. Bonnefoi, T.C. McGill, and R.D. Burnham, *Phys. Rev. B* **37**, 8754 (1988).

[20] E.E. Mendez, E. Calleja, C.E.T. Gonçalves da Silva, L.L. Chang, and W.I. Wang, *Phys. Rev. B* **33**, 7368 (1986)

[21] E.E. Mendez, E. Calleja, and W.I. Wang, *Appl. Phys. Lett.* **53**, 977 (1988).

[22] R. Beresford, L.F. Luo, W.I. Wang, and E.E. Mendez, *Appl. Phys. Lett.* **55**, 1555 (1989).

[23] M. Tsuchiya, T. Matsusue, and H. Sakaki, *Phys. Rev. Lett.* **59**, 2356 (1987).

[24] N. Harada and S. Kuroda, *Jpn. J. Appl. Phys., Pt. 2,* **25**, L871 (1986).

[25] R. Köhrbrück, S. Munnix, D. Bimberg, D.E. Mars, and J.N. Miller, presented at the Seventeenth Annual Conference on the Physics and Chemistry of Semiconductor Interfaces, January 31-February 2, 1990, Clearwater, Florida.

[26] R.C. Miller, A.C. Gossard, W.T. Tsang, and O. Munteau, *Phys. Rev. B* **25**, 3871 (1982).

[27] T.F. Keuch, private communication; K. Akimoto, M. Kamada, K. Taira, M. Arai, and N. Watanabe, *J. Appl. Phys.* **59**, 2833 (1986).

[28] *Landolt-Börnstein: Numerical Data and Functional Relationships in Science and Technology,* edited by O. Madelung, Vol. III/22(a), (Springer-Verlag, Berlin, 1987), pgs. 63, 82.

[29] W.T. Masselink, P.J. Pearah, J. Klem, C.K. Peng, H. Morkoç, G.D. Sanders, and Y.-C. Chang, *Phys. Rev. B* **32**, 8027 (1985).

Chapter 4

Studies of Electrically Biased Double-Barrier Heterostructures

4.1 Introduction

4.1.1 Motivation and Background

As described in Chapter 1, the tunneling response times of double-barrier heterostructures are of interest because of the application of these structures in high-frequency circuits. While investigations such as those described in Chapter 2 yield information regarding tunneling escape times in undoped structures, the structures studied are not functional as electrical devices. Since the application of the double-barrier heterostructure is in electrical circuits where it is normally operated under significant bias, it is of interest to measure the speed of the device under electrical bias. This chapter describes studies of time-resolved photoluminescence and photocurrents in electrically biased double-barrier heterostructures.

The transient response of operational double-barrier heterostructures was first studied with electrooptic sampling [1, 2]. This approach, described in Section 1.3.1, requires the double-barrier device to be mounted in a stripline environment compatible with the propagation of high-frequency transient signals. The experimental difficulties associated with the device mounting and electrooptic sampling are compounded by the effects of parasitic capacitances and inductances associated with contacting and packaging of the device. One of the motivations for the work described in this chapter was to develop techniques that would be complementary to studies in stripline environments, and perhaps enable a fuller understanding of the effects of such parasitics on device response times.

Time-resolved photoluminescence techniques have previously been used to study tunneling times in certain electrically biased heterostructures, but the structures studied to date have been insulating structures, in which no significant current flow is involved. Norris et al. [3] have used photoluminescence decay to study the effect of electric fields on tunneling escape from GaAs quantum wells. The electrons and holes were confined to the quantum well by an infinite $Al_xGa_{1-x}As$ barrier on one side, and a relatively thin $Al_xGa_{1-x}As$ barrier on the other side, and the quantum well was embedded in a *p-i-n* diode, operated in reverse bias. Oberli and coworkers [4] and Liu et al. [5] have used time-resolved photoluminescence to study tunneling in electrically biased double quantum well structures. Since the devices used in both of the above studies were essentially insulating, the main effect of the electric field was to change the energies of electron and hole levels through the Stark effect, and to change the shape and height of the barriers through which electrons and holes were tunneling.

In contrast to previous studies of time-resolved photoluminescence in biased structures, the GaAs/AlAs/GaAs/AlAs/GaAs double-barrier heterostructures studied in the present work all show negative differential resistance, and substantial current flow. The use of photoluminescence in these structures differs from studies of undoped structures such as those described in Chapter 2, because the photogenerated electrons and holes created in the electrode regions can move through the device, and can flow into the quantum well. As will be shown in Section 4.2, the photoexcited carriers from the electrodes can dominate the observed quantum well photoluminescence. This observation motivated a study of photocurrents in the double-barrier heterostructures. In conventional time-resolved photocurrent studies, the current response to photoexcitation by an optical pulse is directly time resolved with high-frequency electronics. However, in the devices studied in the present work, the tunneling times were expected to be on the order of 200 to 1000 ps, which would be difficult to resolve with conventional electronics. A different approach to the photocurrent measurements was used, which was similar to that briefly considered by Sasaki et al. [6]. This new technique is analogous to the correlation photoluminescence technique used in Chapter 2, modified for a study of photocurrents.

4.1.2 Summary of Results

We have fabricated electrically operational double-barrier heterostructures, showing negative differential resistance while simultaneously allowing optical injection of electrons and holes in the double-barrier region. Studies of time-resolved photoluminescence in these structures show that at zero bias, results very similar to those for the undoped structures studied in Chapter 2 are recovered. However, for electrical biases sufficient to cause significant current flow in the absence of photoexcitation, the decay of the quantum well photoluminescence with delay is much less pronounced. These results can be explained by flow of photoexcited electrons or holes into the quantum well of the double-barrier device during the course of the measurement. These photocurrents, which result from the flow of photoexcited carriers, were studied using an extension of the two-beam photoluminescence excitation correlation spectroscopy (PECS) technique described in Chapter 2. In this novel experiment, photocurrents were observed at the sum chopping frequency, indicating an effect of the photogenerated electrons and holes from one optical pulse on the photocurrent due to a delayed pulse. The sum-frequency photocurrent was found to vary with the delay and with the electrical bias voltage. At certain bias voltages, the dependence of the sum-frequency photocurrent upon delay shows exponential components with time constants very similar to the tunneling times in undoped structures determined by time-resolved photoluminescence. One explanation for the observed signals suggests that this technique could be used to study the transient response of other electrical devices that are not amenable to study with time-resolved photoluminescence.

4.1.3 Outline of Chapter

Studies of time-resolved photoluminescence are described in Section 4.2, which also includes details of the device preparation. The correlation photocurrent studies are described in Section 4.3, with a description of device preparation and electrical characteristics in Section 4.3.1. The experimental setup used to make the correlation photocurrent measurements is described in Section 4.3.2; results are presented in Section 4.3.3 and discussed in Section 4.3.4. Conclusions are summarized in Section 4.4.

4.2 Time-Resolved Photoluminescence

4.2.1 Device Preparation

The device (growth number III-082) used for studies of photoluminescence decay was grown by molecular beam epitaxy at 600 °C on an n^+ GaAs (100) substrate. After growth of 0.5 μm of n^+ GaAs ($n \simeq 5 \times 10^{18}\text{cm}^{-3}$), 500 Å of GaAs lightly n-doped ($n \simeq 2 \times 10^{16}\text{cm}^{-3}$), and a 25 Å undoped GaAs spacer layer were grown. This was followed by 34 Å AlAs barrier, 58 Å GaAs well, and 34 Å AlAs barrier layers. Finally another 25 Å undoped GaAs spacer layer, 275 Å of GaAs lightly n-doped ($n \simeq 2 \times 10^{16}\text{cm}^{-3}$), and 300 Å of n^+ GaAs ($n \simeq 5 \times 10^{18}\text{cm}^{-3}$) were grown. Si was used for n-type doping. Relatively thick barriers were used so that current densities would be low, allowing use of a relatively thin n^+ top contact layer without suffering detrimental effects due to series resistance of this layer. A thin top contact layer places the double-barrier region of the device closer to the surface, which reduces attenuation of laser light into, and photoluminescence collected from, the quantum well region. A 60 Å layer of Au/Ge was deposited using an electron-beam evaporator to form the top contact. No annealing of the contacts was performed, because of the proximity of the double-barrier device to the surface. Because of the low current densities in this device, contact resistance did not pose a problem. Mesas were defined and etched using standard photolithographic techniques, and the bottom of the substrate was used as the back contact. Devices were mounted in a TO-5 header using silver paint, and wire bonds were made to the tops of the mesas.

The current-voltage characteristic at 77 K of a 250 μm diameter device is shown in Fig. 4.1 for reverse bias (negative bias of the top contact with respect to the back contact). The peak currents in devices of various sizes were found to

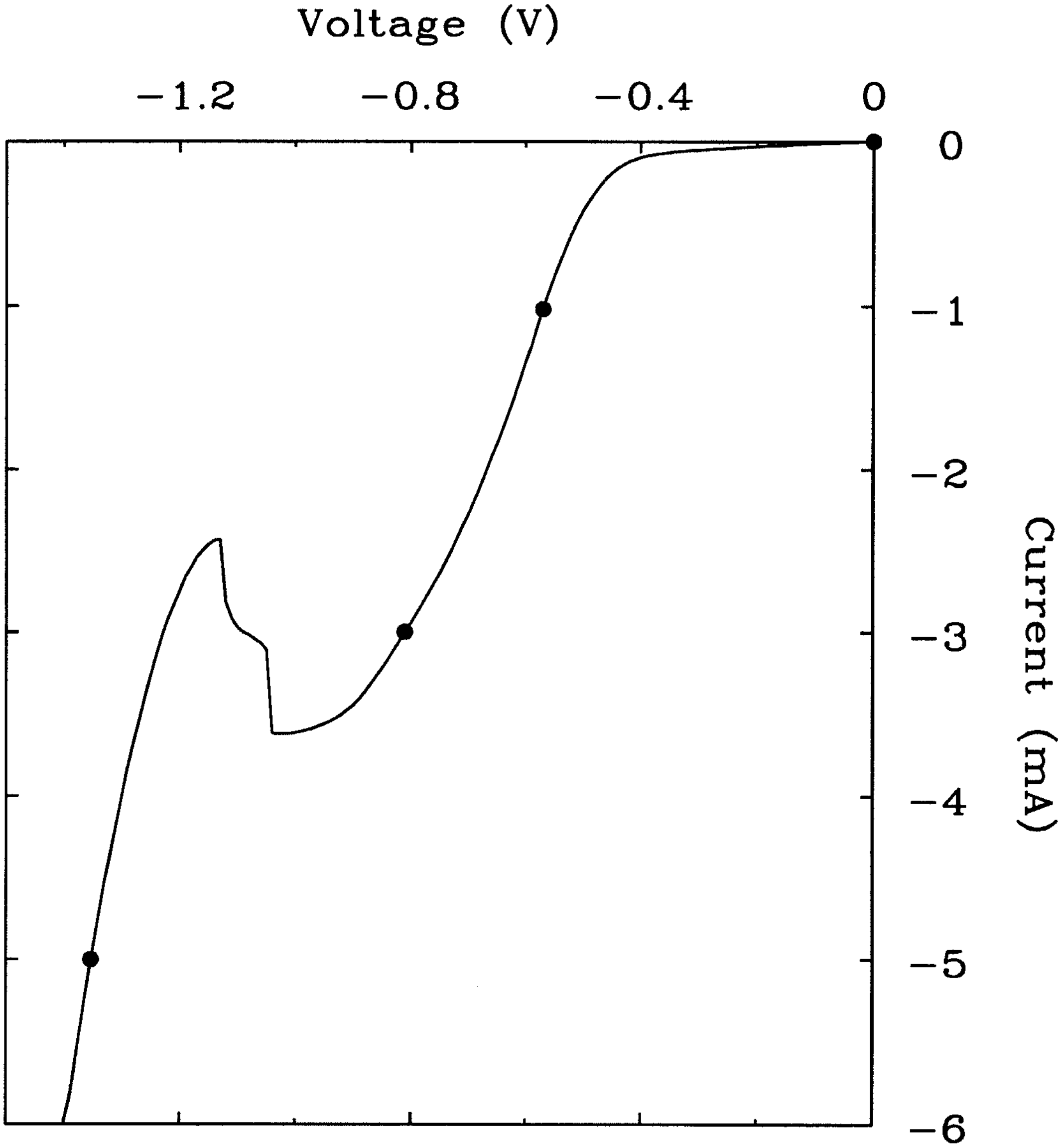

Figure 4.1: Current-voltage characteristic in reverse bias for a 250 μm diameter device, at 77 K. Negative bias corresponds to the flow of electrons into the top of the mesa. The circles mark the biases at which the photoluminescence decay scans shown in Fig. 4.3 were taken.

scale reasonably well with the mesa area, indicating that current is flowing over the whole mesa device, and not just under the wire bond. However, the wire bonding process was found to affect the series resistance of the contact, resulting in variations in the peak voltage due to differing series voltage drops across the metal-semiconductor top contact. The peak current was not affected, indicating that the differences between devices were confined to the contact regions of the devices.

4.2.2 Experimental Arrangement

To measure the photoluminescence under electrical bias, the double-barrier device mounted on a TO-5 header was placed in a helium immersion dewar, modified to allow electrical contacts to the device. The temperature was maintained at 80 K. The laser spot was focused on an area of the mesa not obscured by the wire bond, requiring the use of mesas at least 150 μm in diameter. The photoluminescence excitation correlation spectroscopy (PECS) technique described in Section 2.2 was used for time-resolved photoluminescence measurements, with the photoluminescence being collected from the top of the mesa and imaged into a spectrometer. Electrical bias was provided by either a constant-current source, a constant voltage source, or a Tektronix Model 577 curve tracer.

4.2.3 Results

Time-resolved photoluminescence data were obtained using the photoluminescence excitation correlation spectroscopy (PECS) technique described in Section 2.2. The photoluminescence spectrum at the sum chopping frequency in the region of the peak of the quantum well luminescence is shown in Fig. 4.2, for a bias current of –1 mA. The linewidth of the quantum well peak in Fig. 4.2 is

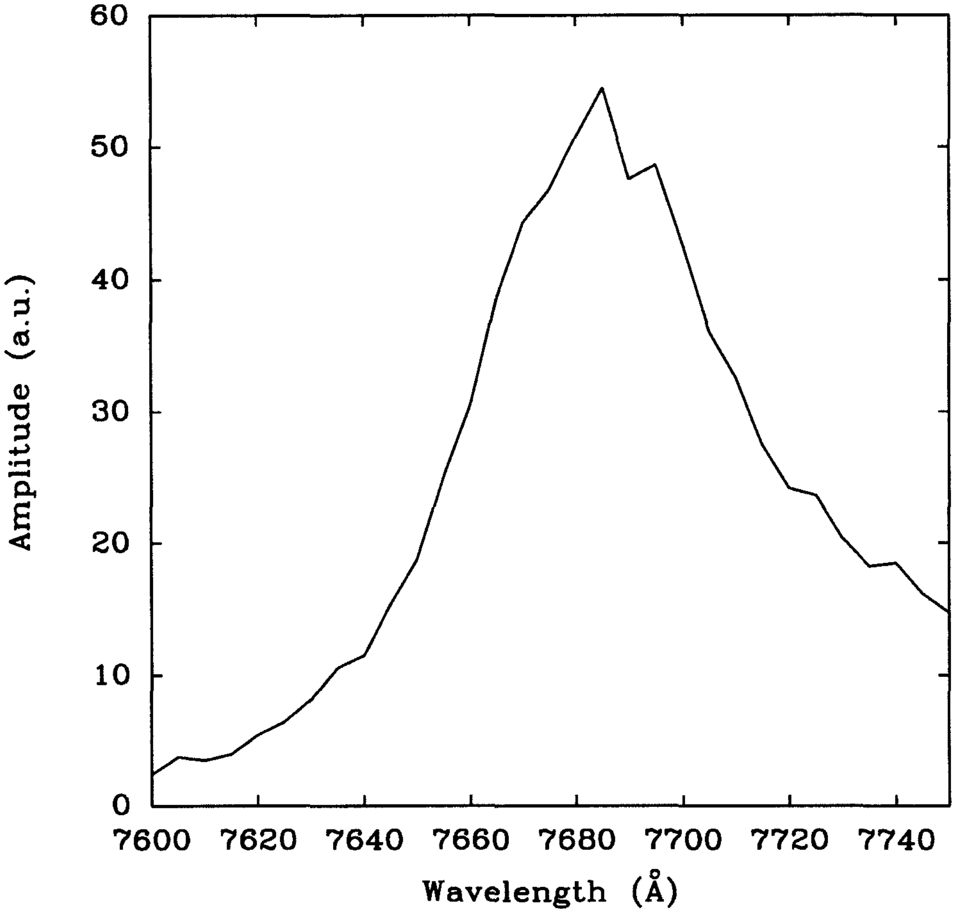

Figure 4.2: Photoluminescence spectrum from the quantum well at the sum chopping frequency, for a current of −1 mA, and at 80 K. The rising background at longer wavelengths is due to recombination from the n^+ GaAs electrode regions.

consistent with monolayer fluctuations in the quantum well thickness, and the rising background at longer wavelengths is due to recombination in the n^+ GaAs electrode regions. As expected, a Stark shift of the quantum well photoluminescence peak to longer wavelengths (i.e., a red shift) is observed as the bias across the sample is increased. The fact that a Stark shift is observed in luminescence from an area of the mesa that is not directly underneath the wire bond indicates that significant electric fields are developed across the quantum well due to the applied bias. This conclusion is consistent with the current-voltage data, which indicated that current flow is fairly uniform across the mesa area.

In Fig. 4.3 we show the dependence upon delay of the sum-frequency amplitude at an energy corresponding to the peak of the quantum well photoluminescence. A variety of bias currents were used, with Figs. 4.3(a), (b), (c), and (d) corresponding to the bias currents of 0, −1, −3, and −5 mA, respectively, which were indicated in Fig. 4.1 by circles. Sum-frequency photoluminescence delay scans were studied with varying optical powers and bias schemes. It was found that for nonzero bias and average optical powers on the order of 1 mW per beam after chopping, the variation of the sum frequency photoluminescence with delay was different depending upon whether a current source, voltage source, or curve tracer was used to provide electrical bias. This effect was found to be less severe with lower optical power; at a power of 135 μW per beam, the variation with delay was independent of the source of electrical bias. Accordingly, we present data only for low optical powers.

From Fig. 4.3(a) it can be seen that at zero bias significant decay of the photoluminescence signal is observed within the ±500 ps delay accessible experimentally. This correponds well to the expected lifetime of approximately 800 ps observed for the two undoped samples with 34 Å AlAs barriers and 58 Å quantum wells studied in Chapter 2. The decay of the photoluminescence signal at higher

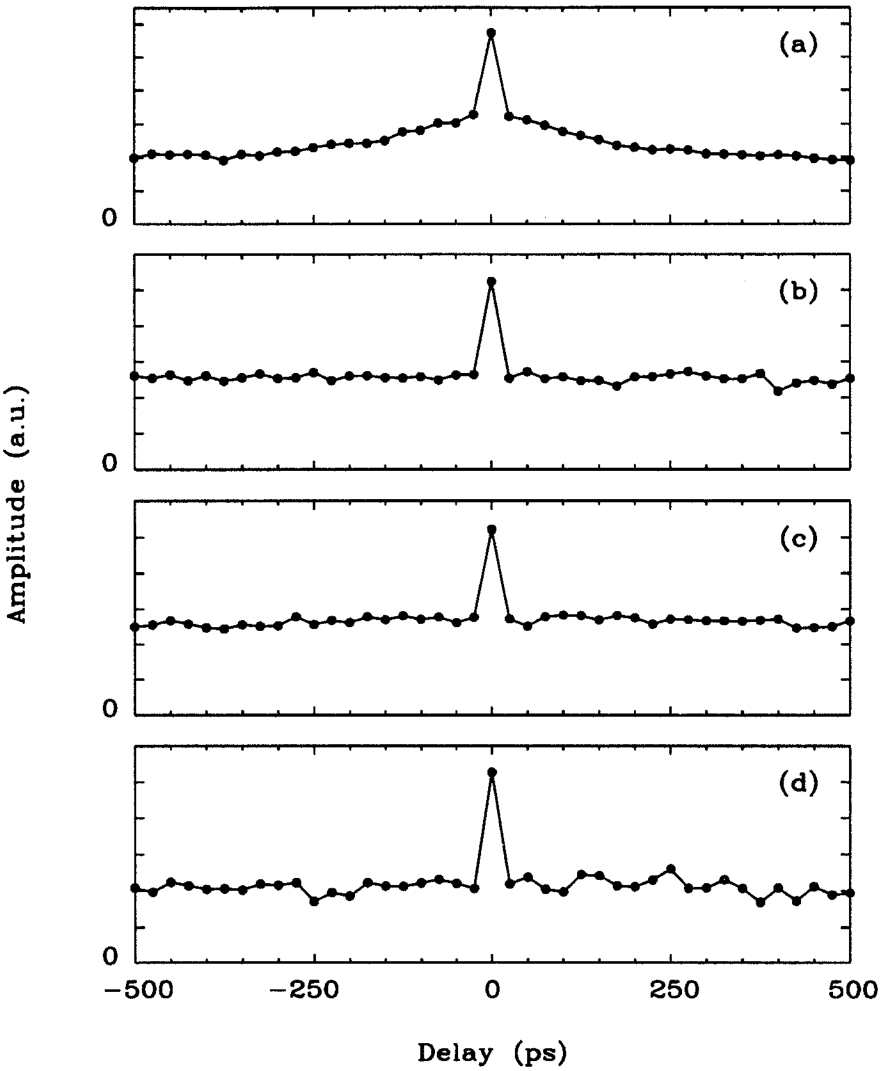

Figure 4.3: Sum-frequency photoluminescence delay scans for sample III-082, at the peak of the quantum well luminescence, at 80 K, for the various bias levels indicated in Fig. 4.1: (a) zero bias, (b) −1 mA, (c) −3 mA, (d) −5 mA. The solid line connects the experimental points to aid the eye. The decay in (a) is comparable to that observed in similar undoped structures. The decays in (b), (c), and (d) are much less over the same range, due to the influx of photoexcited carriers from the electrodes. The coherence peak at zero delay does not reflect decay of the carrier densities.

bias, shown in Figs. 4.3(b)-(d), is very different. The coherence peak at exactly zero delay, an artifact due to optical interference of the two pump pulses which was discussed in Chapter 2, is still seen in all scans. However, the behavior for nonzero delay times is quite different as seen in Figs. 4.3(b)-(d). The decay of the sum frequency signal is negligible over the ±500 ps range of delay times. This indicates that decay of the electron and hole densities in the quantum well occurs on a time scale much longer than 500 ps, in contrast to the tunneling escape lifetime of approximately 800 ps expected from measurements in the undoped structures, and seen in Fig. 4.3(a). This difference in the decay can be explained in terms of the effects of electrons and/or holes photoexcited in the electrode regions, as will be discussed in the following section.

4.2.4 Discussion

In order to understand the delay scans shown in Fig. 4.3, it is helpful to reexamine the analysis of the PECS measurement technique given in Section 2.2 for the undoped structures. In structures at zero bias, it is reasonable to assume that the flow of photoexcited carriers from the electrode region into the quantum well is insignificant, because carriers relax very quickly to the band edges, where they are energetically forbidden from tunneling into the quantum well. However, significant current flow can be obtained in the biased structure (as is the case for Figs. 4.3(b)-(d)). It is reasonable, then, to expect that photoexcited electrons and/or holes can flow from the electrodes into the quantum well. In this case, the decay of the quantum well photoluminescence would be much less rapid, as escaping carriers initially photoexcited in the quantum well are replaced by photoexcited carriers in the electrodes tunneling into the quantum well. We attribute the decreased decay of the photoluminescence from the quantum well at nonzero bias seen in Figs. 4.3(b)-(d) to the flow of photoexcited carriers from the electrodes into the quantum well. This explanation of the decreased rate of decay of the photoluminescence at nonzero bias is supported by the recent work of Vodjdani et al. [7], who studied continuous wave (CW) photoluminescence from structures very similar to the ones studied in the present work. By utilizing photoexcitation energies below and above the quantum well photoluminescence energy, they were able to photoexcite only in the electrodes, or in both the electrodes and the quantum well. For biases near the peak voltage, they observed that the intensity of the quantum well photoluminescence was the same for both excitation energies. This result suggests that the majority of the carriers contributing to the photoluminescence signal originate in the electrodes, consistent with our conclusion that carriers photoexcited in the electrodes are important in the time-resolved data for nonzero bias shown in Fig. 4.3. The idea that significant flow of photoexcited carriers occurs during the photoluminescence measurement motivated the study of photocurrents in these devices, described in the following section.

4.3 Photocurrent Measurements

4.3.1 Device Preparation and Current-Voltage Characteristics

Time-resolved photocurrents were studied in three devices with varying barrier thicknesses. The growth of the devices was identical to those described in Section 4.2.1, except that the top n^+ layer thicknesses in the present devices were all 600 Å. The n^+ layer thickness was increased to aid in distribution of current over the whole mesa area. Three devices, differing only in the thickness of the AlAs barriers, were grown: III-083 with 34 Å barriers, III-222 with 31 Å barriers, and III-221 with 28 Å barriers. The processing of the MBE wafers into devices was somewhat different from the procedure described in Section 4.2.1. In the present devices, $350\,\mu$m mesas with annular AuGe contacts were defined using liftoff photolithographic techniques. The AuGe thickness was approximately 1000 Å, and the inner and outer diameters of the annular contacts were 125 and $275\,\mu$m, respectively. As with the previous device studied by photoluminescence, no annealing of the contacts was performed, because of the proximity of the double-barrier device to the surface. Contact resistance did not pose a problem, resulting only in a series resistance which shifted the peak in the current-voltage characteristic to higher voltage. The bottom of the substrate was used as the back contact, and devices were mounted in a TO-5 header using silver paint. The large area of the annular contact allowed individual mesas to be contacted by up to three wire bonds, which was important because of the increased current density in the 28 Å-barrier sample.

The current-voltage characteristics at 77 K of the three devices are shown in Fig. 4.4 for reverse bias (negative bias of the top contact with respect to the back contact). All three devices shown in Fig. 4.4 show reasonable negative differential resistance (NDR) characteristics, and the peak current densities increase with decreasing barrier thickness. The increase in current density with decreasing barrier thickness is quantitatively in good agreement with the tunneling times measured in Chapter 2. The current densities and inverse tunneling times are expected to follow the same trend with barrier thickness because they both reflect the energy width of the quasi-bound state in the quantum well. This agreement confirms that the barrier thicknesses in the three samples vary as expected from the nominal growth parameters. It can be seen in Fig. 4.4 that the peak current shifts to higher voltages as the barriers become thinner. This trend is due to

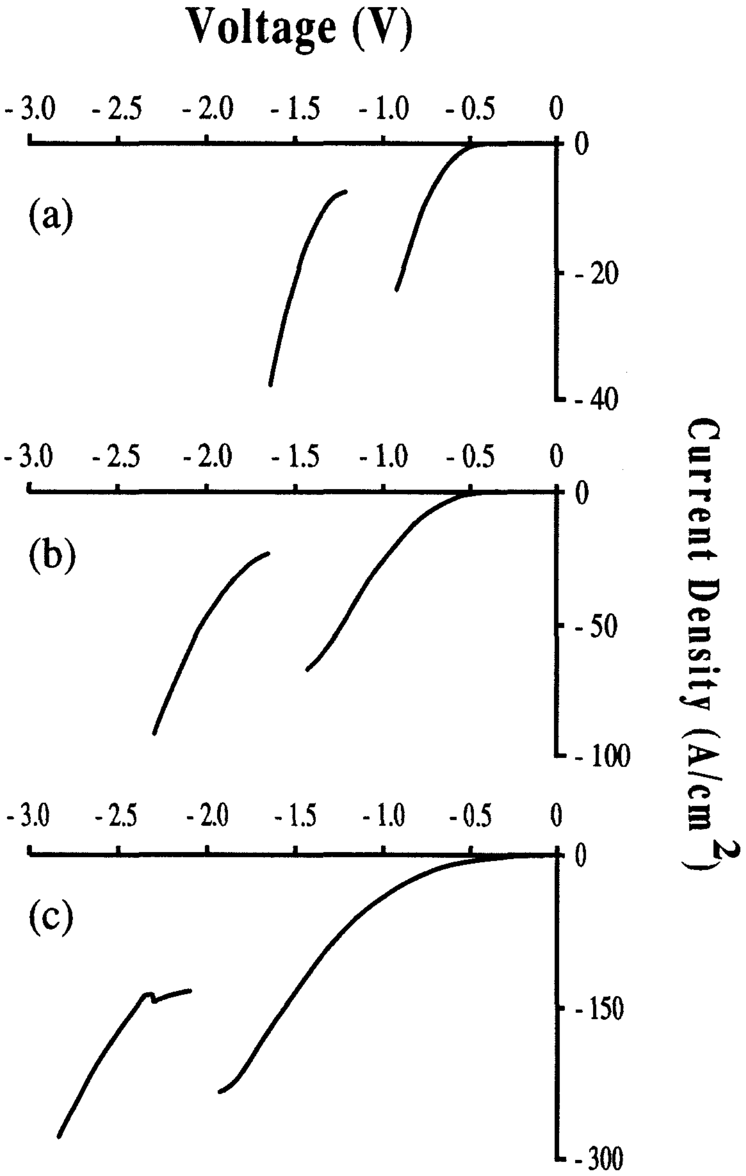

Figure 4.4: Current-voltage characteristics in reverse bias for the three devices studied, at 77 K. (a) III-083 (34 Å barriers), (b) III-222 (31 Å barriers), (c) III-221 (28 Å barriers). The peak current density increases with decreasing barrier thickness, quantitatively as expected. The effect of series resistance of the top contact can be seen, as the peak voltage shifts to progressively higher voltages. Negative bias corresponds to the flow of electrons into the top of the mesa.

series resistance in the nonannealed top contacts, which becomes increasingly important with higher current densities. To check that the current in the mesa samples with annular top contacts was flowing over the whole mesa area, variable size mesas with thick AuGe top contacts were fabricated. The peak currents in the variable size mesas scaled well with area, and the current densities in the devices with annular contacts were in good agreement with the current densities observed with variable size mesas.

4.3.2 Experimental Apparatus

The photocurrent measurements were made at 80 K, with the devices mounted in a helium immersion dewar, modified to allow electrical contacts to the device while mounted in the dewar. As in the photoluminescence excitation correlation spectroscopy (PECS) technique described in Section 2.2, the output from the colliding pulse mode-locked (CPM) dye laser was split into two pulse trains of equal amplitude. Each pulse train was mechanically chopped at a different frequency, and the beams were recombined with a variable delay time γ between them. The recombined beam was focused to a $40\,\mu$m diameter spot in the center of the mesa.

The arrangement used for the electrical biasing and photocurrent detection is shown schematically in Fig. 4.5. Electrical bias across the device was provided by a Hewlett Packard model 6115A precision constant voltage source labelled VS. The current flow to the device was measured with an Ithaco 1211 current-to-voltage preamplifier labelled PA, in series with the voltage source. Because the current-to-voltage preamplifier was limited to a current of 10 mA, and the total currents through the $350\,\mu$m mesas were as large as 400 mA, it was necessary to use a constant current source IS to bypass most of the DC current around the current-to-voltage amplifier. A Keithley 220 current source was used for

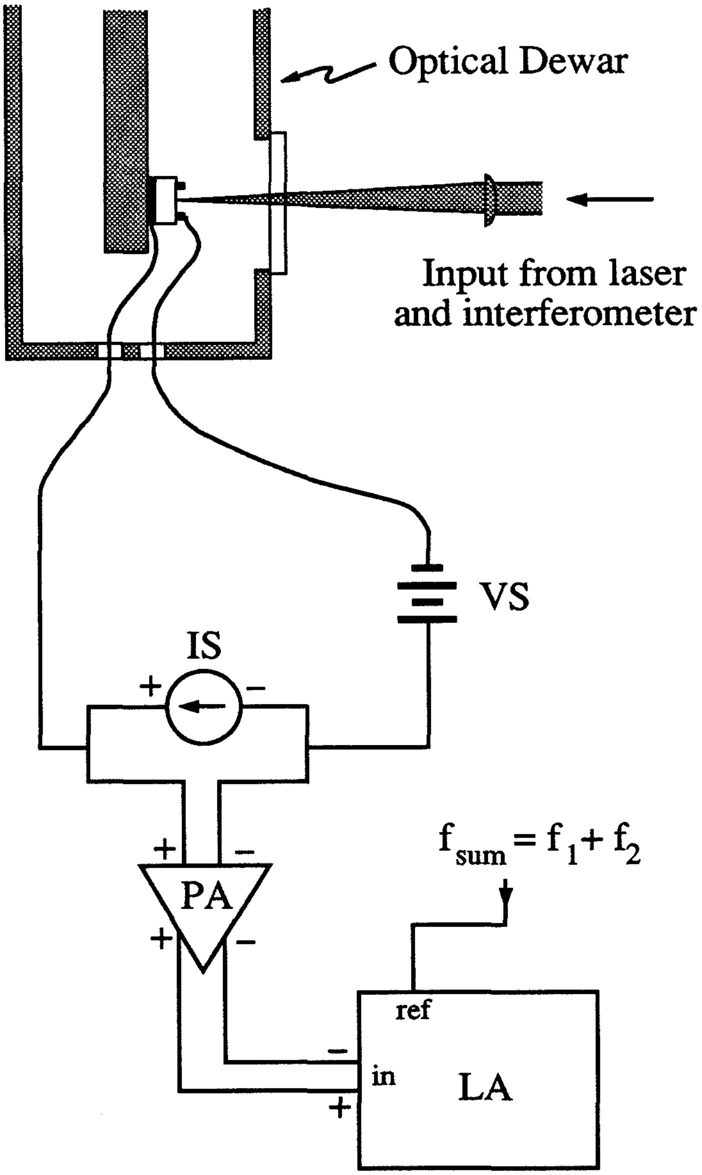

Figure 4.5: Experimental arrangement for photocurrent experiment. Constant voltage bias is provided to the double-barrier device, which is mounted in an optical dewar, by the precision constant voltage source VS. The photocurrent is monitored using the current-to-voltage preamplifier PA, and the output is detected by the lock-in amplifier LA. DC current bypass around the preamplifier is provided by the constant current source IS.

some measurements, but measurements on the higher current devices required the construction of a high-current constant current source using standard high power bipolar transistors. For a given bias voltage, the current source was adjusted so that the current preamplifier operated in its linear range. The output of the preamplifier was detected by the lock-in amplifier labelled LA. The reference signal for the lock-in amplifier was obtained by combining the reference signals from the two choppers using a simple TTL "AND" gate, and recovering the sum-frequency component with a frequency-selective amplifier.

The simplicity of the experimental apparatus in Fig. 4.5 is to be contrasted with the setup required for the all-optical measurements described in Chapter 2, or for electrooptic sampling measurements. All electronics used are low frequency, and it is not necessary to collect luminescence from the sample or to use a spectrometer.

4.3.3 Results

The dependence of the sum-frequency photocurrent upon delay for sample III-221 (28 Å barriers) at –2.4 V is shown in Fig. 4.6. The real and imaginary parts of the photocurrent signal are shown in Fig. 4.6 as solid and dashed lines, respectively, defined with respect to an arbitrary absolute phase. The sum frequency photocurrent signal is on the order of a few microamperes in this scan, which was taken with an optical power of 0.75 mW per beam after chopping. The DC photocurrent is much larger, and is on the order of 800 μA (with both chopped beams on the sample) at a bias of –2.4 V.

As seen in Fig. 4.6 both the real and imaginary parts show significant variation over the ±500 ps delay accessible experimentally. This is in contrast to the only previous study of photocurrents using this technique, in which no change

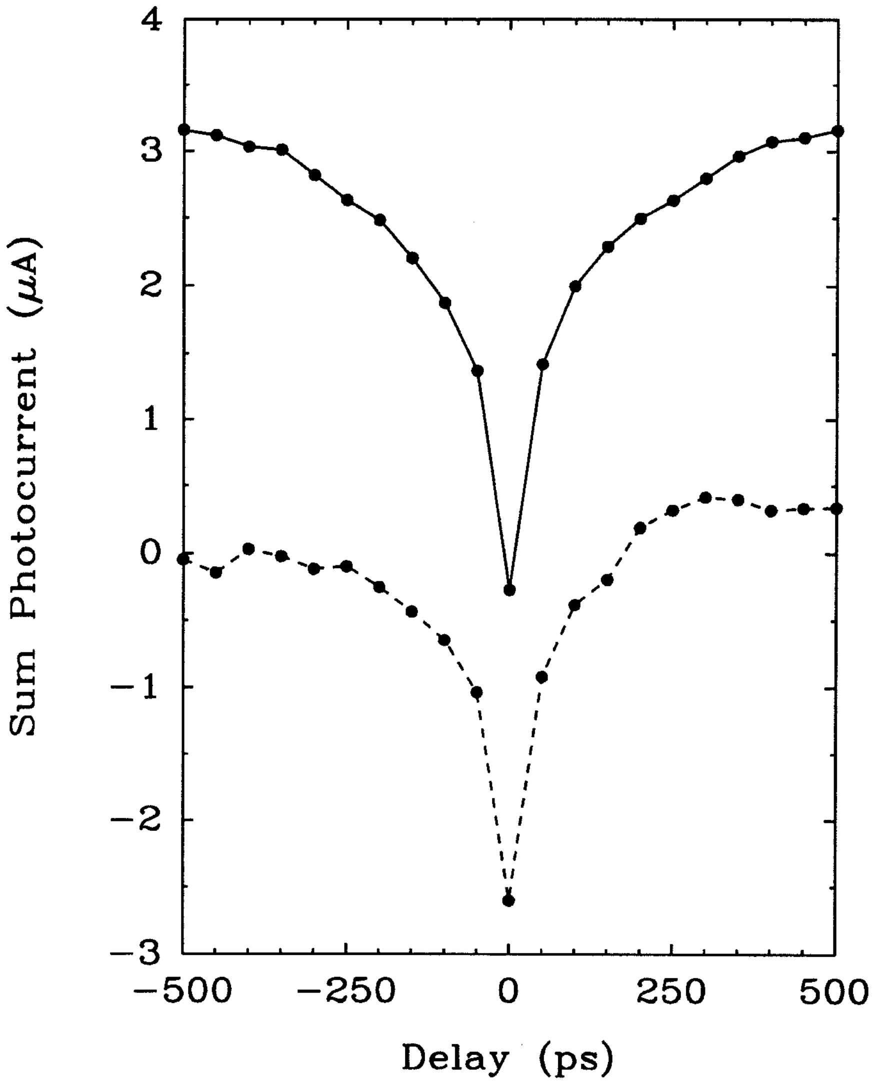

Figure 4.6: Typical sum-frequency photocurrent delay scan, for sample III-221 (28 Å barriers) at a bias of −2.4 V. The real and imaginary parts of the photocurrent, defined with respect to an arbitrary absolute phase, are shown as solid and dashed lines, respectively, where the lines connect the experimental points to aid the eye. The slight asymmetry with respect to zero delay seen in the imaginary component is attributed to noise in the phase of the detected photocurrent.

of the sum-frequency signal with delay was reported [6]. A coherence peak is seen in both scans at zero delay, due to optical interference of the pump laser pulses. The real part of the signal shown in Fig. 4.6 can be described as a sum of a constant and an exponential with a time constant on the order of 200 ps. Optical measurements, presented in Chapter 2, of a similar undoped sample with 28 Å barriers showed a tunneling escape time of 236 ± 20 ps, and suggest that the observed decay of the photocurrent signal may coincide with the time for a tunneling process in the sample.

It can be seen in Fig. 4.6 that the signal is mostly real at long delay, and mostly imaginary for zero delay. The only quantity which was varied during the measurement was the position of the moveable arm of the interferometer used to delay the pulses with respect to each other. Similar changes in phase with delay were observed in the same sample at other bias voltages, and in other samples with differing barrier thicknesses. The change from predominantly real to imaginary was not always as pronounced as in Fig. 4.6, but was a reproducible effect. The fact that the time-varying component of the real part of the photocurrent seen in Fig. 4.6 decays to a nonzero background suggests that the photocurrent signal at the sum frequency consists of signals with two different origins. The variation of the phase with delay suggests that the two signals are out of phase with each other by approximately 90 degrees, which may reflect the difference between resistive and reactive responses. The phase of the total signal then depends upon the relative amplitudes of the two components, which varies with delay. As the two chopping frequencies used in this experiment are 1600 and 2000 Hz, the sum frequency of 3600 Hz has a period of 280 μs. A phase shift of 90 degrees at this frequency corresponds to a time delay between the two processes of one quarter of a period, or 70 μs. The origin of such a long delay in this structure is not clear. However, in photocurrent studies of doped GaInAs/InP superlattices, Ripamonti et al. [13] observed transient photocurrents with a time constant of 200 μs at 80 K, which they attributed to the presence of traps in the n regions of their devices (including InP and the superlattice layers). He and coworkers [14] have also considered the effects of capture of photoelectrons in Si-doped GaAs/$Al_xGa_{1-x}As$ heterostructures, upon persistent photocurrent decay, in which very long time constants were observed. These mechanisms involving traps may be responsible for the component of the photocurrent that has a very long time delay.

The dependence upon bias of the real part of the sum-frequency photocurrent for sample III-221 is shown in Fig. 4.7, defined with respect to the same absolute phase as in Fig. 4.6. The scans are all shown on the same scale, but are offset vertically for clarity. The coherence peak is seen in all scans, although for -2.4 V it is opposite in sign to the peak seen in the other scans. It can be seen that at some biases, there is very little change of the photocurrent signal with delay, and in other cases, there is significant decay over the ±500 ps of delay shown. The greatest decay occurs for a bias voltage of approximately -0.3 V, and then decreases with increasing reverse bias. The bias of -0.3 V can be seen, from the current-voltage characteristic shown in Fig. 4.4(c), to correspond to a bias voltage near the threshold for the tunneling current. For biases past the peak voltage of -2.0 V, the variation of the signal with delay is inverted, as seen in the scan at -2.4 V shown in Fig. 4.7. No further qualitative changes were observed with increasing bias.

The qualitative behavior seen in Fig. 4.7 is reproduced in all three of the samples: there is little decay at low bias, a pronounced decay near the turn-on in tunneling current, little decay between the turn-on and the peak, and pronounced decay again with bias greater than the peak voltage. To compare delay scans from the three samples, we show in Fig. 4.8 photocurrent delay scans for the three samples studied, at bias voltages greater (i.e., more negative) than the

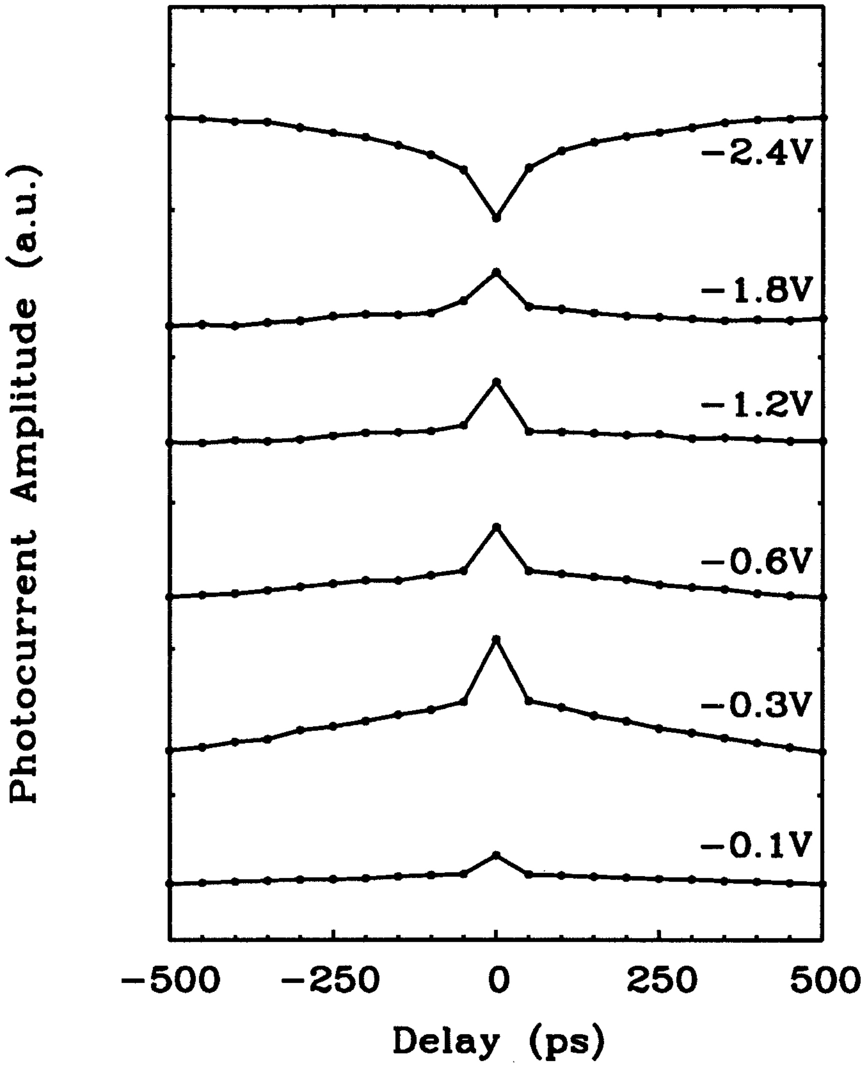

Figure 4.7: The real part of the sum-frequency photocurrent as a function of delay, for sample III-221 (28 Å barriers), as a function of bias. All scans are shown with the same vertical scale, but have been offset vertically for clarity. The solid lines connect the experimental points to guide the eye. The amount of decay varies with bias, showing pronounced decay at –0.3 V and –2.4 V. The photocurrent for –2.4 V, which corresponds to bias greater than the peak voltage, shows inverted behavior with respect to that seen at lower biases.

peak voltage. The decay behaviors seen in the three scans are quite different. While the scans shown in Figs. 4.8(b) and (c), (for samples with 31 and 28 Å barriers, respectively) show a signal which can be described by a constant plus an exponential with a time constant on the order of 200 ps, the scan shown in Fig. 4.8(a) can only be fitted by a constant and an exponential with a time constant long compared to 500 ps. The differing decay behavior may be indicative of the differing tunneling times in the three samples. From the time-resolved photoluminescence measurements of undoped structures presented in Chapter 2, the tunneling times for samples with 34, 31, and 28 Å barriers are expected to be approximately 800, 440, and 240 ps, respectively. Fits of an exponential plus a constant to the data shown in Fig. 4.8 give good agreement between the photocurrent decay times, and the photoluminescence decay times, for the samples with 34 and 28 Å barriers, shown in Figs. 4.8(a) and (c), respectively. However, the time required to fit to the photocurrent decay for the sample with 31 Å barriers is on the order of 200 ps, which differs considerably from the tunneling escape time of 440 ps expected from photoluminescence decay.

4.3.4 Discussion

The photocurrent data clearly show that a photocurrent signal is observed at the sum chopping frequency, and that this photocurrent depends upon bias and sample parameters. The observation of a sum-frequency photocurrent signal indicates that the photocurrent responses to the photoexcitation at the two chopping frequencies, f_1 and f_2, are not independent.* Thus, the magnitude of the sum-frequency photocurrent is a measure of the influence of the presence of

---

*If the responses were independent, then the only frequency components in the detected photocurrent would be at the two chopping frequencies f_1 and f_2.

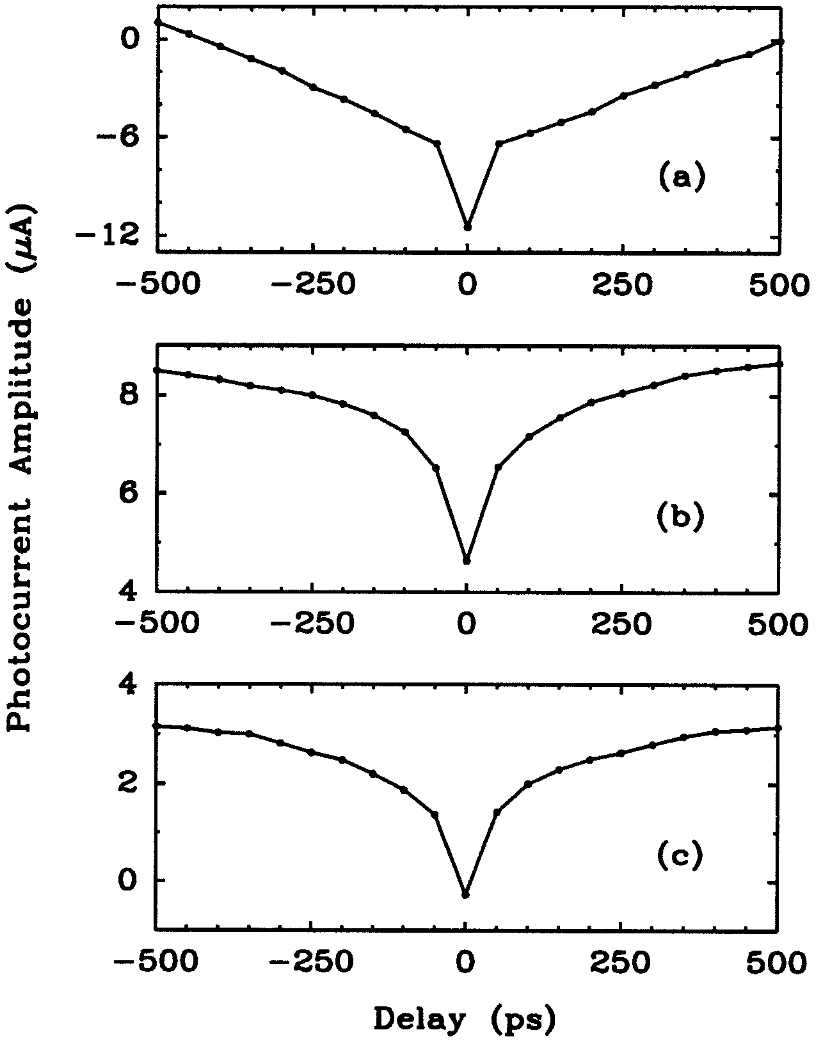

Figure 4.8: Comparative sum-frequency photocurrent delay scans at biases greater than the peak voltage. (a) III-083 (34 Å barriers), (b) III-222 (31 Å barriers), (c) III-221 (28 Å barriers). The differing decay behavior may be indicative of the differing tunneling times in the three samples, which are expected, from the measurements of undoped structures presented in Chapter 2, to be approximately 800, 440, and 240 ps for (a), (b), and (c), respectively. The agreement between the photoluminescence time constants and the decay behavior is quite good for (a) and (c), but not for (b).

photocarriers excited by one pulse train, at frequency f_1, for example, upon the current due to photocarriers excited by the other pulse train at frequency f_2.

The observation of a sum-frequency photocurrent means that we can measure the interaction between the two sets of photocarriers. We now consider the dependence of the sum-frequency photocurrent upon delay, to see why the experimental data might be expected to change with increasing delay between the two pulse trains. With an excitation photon energy of 2 eV, carriers are photoexcited throughout the GaAs electrodes, and in the quantum well of the double-barrier device. Taking the absorption length to be approximately $0.25\,\mu$m for GaAs at this energy [8], we note that significant carrier densities will be photoexcited to a depth from the surface of a few times the absorption length, which is on the order of 0.5 to $1\,\mu$m in this case. In principle, the interaction of the photocarriers from the two pulse trains occurs over the entire photoexcited volume. It is likely, however, that the interaction is strongest in regions in the device where accumulations of carriers, or large electric fields which separate photoexcited electrons and holes, are present. If we assume that the interaction region is confined to a single location, then we can form a simple picture of why the sum-frequency photocurrent might vary with delay between the two pulses. If the lifetime of photoexcited electrons and/or holes in this localized interaction region is τ, then the effect of photocarriers from the first pulse train will be negligible if the second pulse train is delayed by significantly more than τ. This is exactly what happens in the PECS photoluminescence experiment used in Chapter 2. In the photoluminescence experiment, the carriers photoexcited by the two pulse trains interact via the two-particle nature of the photoluminescence process. When the delay between the two pulse trains is greater than both the electron and the hole escape times, then there is no interaction of the photocarriers excited by the two pulse trains, and no sum-frequency photoluminescence signal is detected. Simply stated, the photoexcited carriers from the two pulse trains never coexist in the region of interaction, which is the quantum well in this case. A similar effect could be responsible for the variation of the sum-frequency photocurrent with delay presented above. The time for decay of the sum-frequency photocurrent would be the time required for photocarriers to escape from the region in which they influence the photocurrent from the delayed pulse train. Possible mechanisms for the interaction of the two pulse trains, and their relation to tunneling times, will be considered further in the following paragraphs.

To consider one of several possible mechanisms for the interaction of the carriers that would lead to a sum-frequency photocurrent, we show in Fig. 4.9(a) the conduction band profile, for sample III-083. The profile was calculated using the Thomas-Fermi approximation and solving the Poisson equation at a bias of −0.25 V. The quasi-Fermi levels in the left and right electrodes are assumed to be constant, up to the undoped double-barrier region, and are indicated in Fig. 4.9(a) by dot-dashed lines. The surface of the device is located at −900 Å in Fig. 4.9(a), and we have neglected the effect of surface depletion in this calculation. The depicted bias level of −0.25 V corresponds to the threshold in the current-voltage curves of Fig. 4.4. At this bias, current flow in the absence of photoexcitation is low, and is due to the few electrons in the injecting electrode with sufficiently high kinetic energy to allow tunneling through the quasi-bound state in the quantum well. In Fig. 4.9(b), we show a magnified view of the electron accumulation region and the quantum well. The approximate energy of the confined state in the quantum well is indicated in Fig. 4.9(b) by a dotted line in the quantum well, and the dot-dashed line again shows the position of the Fermi level with no photoexcitation. The electron density will be increased by absorption of photons, and the quasi-Fermi level that would reflect such an increase in electron density is shown in Fig. 4.9(b) for excitation by one or two optical pulses, as shown

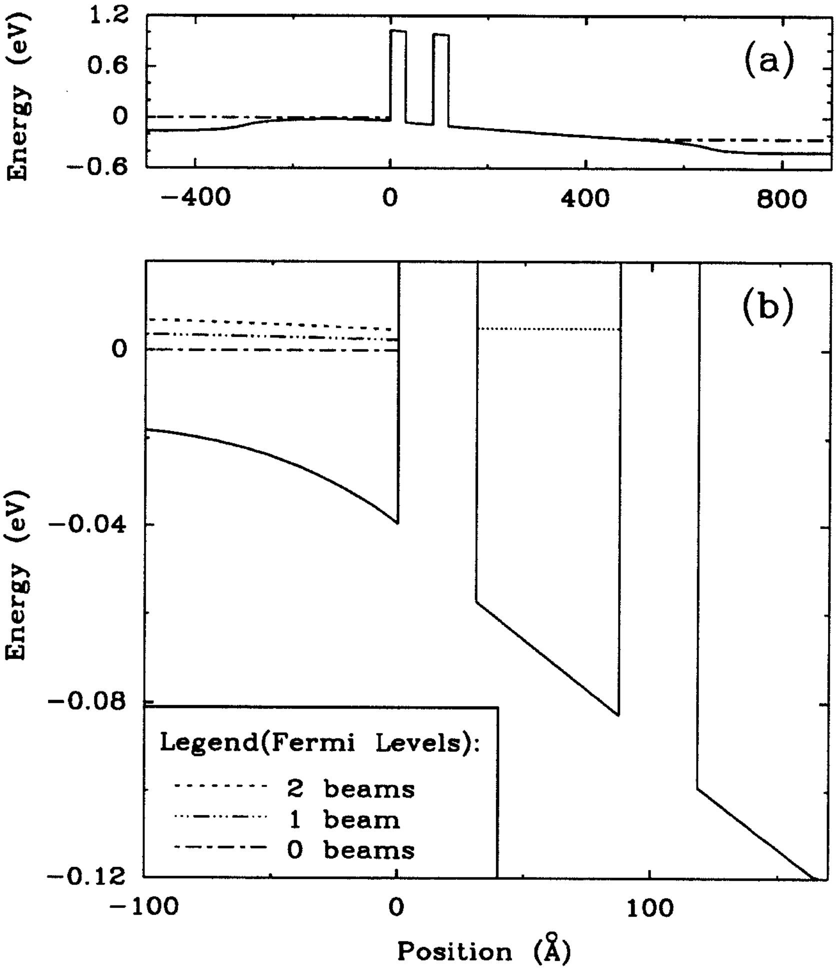

Figure 4.9: (a) Conduction band profile calculated for sample III-221 (28 Å barriers) at a bias of −0.25 V, neglecting depletion at the surface which is at −900 Å. The dot-dashed line indicates the positions of the quasi-Fermi levels in the two electrodes. (b) Magnified view of the accumulation region. The dotted line shows the energy level of the quasi-bound state in the quantum well. The quasi-Fermi levels are shown, as indicated in the legend, for the cases of no photoexcitation, and immediately after photoexcitation by one or two pulses. The photoexcited carriers from the first pulse increase the average energy of the carriers photoexcited by the second pulse.

in the legend to the figure. The increased quasi-Fermi level affects the portion of the injecting electron distribution with large kinetic energy, increasing the density of electrons at an energy sufficient to allow tunneling through the quasi-bound state in the quantum well, and resulting in a photocurrent. In the case of photoexcitation by two optical pulses, the presence of the electrons photoexcited by the first pulse results in a higher average kinetic energy for the electrons excited by the second pulse. This effectively increases the fraction of carriers from the second pulse that have sufficiently high kinetic energy to tunnel through the quasi-bound state, and results in a greater photocurrent. This mechanism would result in an interaction between the two pulse trains, and could explain the observation of a sum-frequency photocurrent. This explanation is supported by the fact that the photocurrent scans shown in Fig. 4.7 show pronounced variation with delay at a bias of –0.3 V, which is very close to the –0.25 V bias illustrated in Fig. 4.9. We suggest that the mechanism described above could be responsible for the interaction between the carriers photoexcited by the two pulse trains, and give rise to the sum-frequency photocurrent data presented in Section 4.3 for biases near threshold. The additional effects of photoexcitation in the quantum well region, which were not considered in the above description, could also prove to be significant.

If, as suggested above, the interaction of the carriers in the tail of the injecting electron distribution is responsible for the observed photocurrent decay, then the appropriate decay time for the interaction, and therefore the sum-frequency photocurrent, would be the time required for electrons to tunnel from the injecting electrode through the double-barrier. This would mean that measurements of the photocurrent decay would reflect the tunneling times in the structures, and explain the similarity between the photocurrent decay times and photoluminescence decay times. It is also possible that the same approach would be successful in many other tunneling structures, such as single barrier [9, 10] or interband tunnel structures [11, 12], which are difficult or impossible to study using time-resolved photoluminescence. The possibility of using the photocurrent technique presented above to study the dynamics of tunneling in these structures suggests that further study of this photocurrent technique could be very fruitful. There are several remaining questions that must be answered regarding the interpretation of data from this type of experiment. For instance, we have only considered one possible mechanism for interaction between the two pulse trains. Others that could be important are interaction in the quantum well, interaction in the surface depletion region, and effects analogous to those described above for the holes photoexcited on the substrate side of the double-barrier. The possible importance of trapping processes, which could be responsible for a component of the photocurrent that is delayed with respect to excitation by long times, and give rise to the varying phase with delay seen in the photocurrent data shown in Fig. 4.6, must also be considered.

As with many correlation techniques, this time-resolved photocurrent experiment is fairly simple. A thorough understanding of the interaction process is necessary, however, in order to interpret the sum-frequency data obtained, and this will require a more detailed study of the processes important to the photocurrents in the double-barrier devices studied.

4.4 Conclusions

We have presented a study of time-resolved photoluminescence and photocurrent in electrically biased GaAs/AlAs/GaAs/AlAs/GaAs double-barrier heterostructures. As expected, the time-resolved photoluminescence from the quantum well region shows a decay time at zero bias that is comparable to similar measurements in undoped structures. However, the behavior with nonzero bias is quite different. Little decay of the quantum well photoluminescence with delay is observed, due to the flow of photoexcited electrons and/or holes from the electrodes into the quantum well. The photocurrents due to the flow of the photoexcited carriers were studied using a time-resolved photocurrent technique, analogous to the PECS photoluminescence technique described in Chapter 2. Using this technique, photocurrents were measured during photoexcitation by two mechanically chopped optical pulse trains, delayed with respect to each other by a variable time γ. Small photocurrent signals were observed at the sum chopping frequency, and were seen to vary with time delay γ, bias voltage, and sample parameters. The time constants extracted from the decay of the sum-frequency photocurrents are similar to the tunneling times measured in undoped structures, although detailed agreement is obtained only for two of the three samples studied. A possible explanation for the observation in the photocurrent of a decay time related to the tunneling time was presented, suggesting that the technique could be used to study other tunneling devices that cannot be studied by photoluminescence.

References

[1] J.F. Whitaker, G.A. Mourou, T.C.L.G. Sollner, and W.D. Goodhue, *Appl. Phys. Lett.* **53**, 385 (1988).

[2] S.K. Diamond, E. Özbay, M.J.W. Rodwell, D.M. Bloom, Y.C. Pao, E. Wolak, and J.S. Harris, in *OSA Proceedings on Picosecond Electronics and Optoelectronics*, Vol. 4 of the OSA Proceeding Series, T.C.L.G. Sollner and D.M. Bloom, eds. (Optical Society of America, Washington, D.C., 1989), p. 101.

[3] T.B. Norris, X.J. Song, W.J. Schaff, L.F. Eastman, G. Wicks, and G.A. Mourou, *Appl. Phys. Lett.* **54**, 60 (1989).

[4] D.Y. Oberli, J. Shah, B. Deveaud, and T.C. Damen, in *OSA Proceedings on Picosecond Electronics and Optoelectronics*, Vol. 4 of the OSA Proceeding Series, T.C.L.G. Sollner and D.M. Bloom, eds. (Optical Society of America, Washington, D.C., 1989), p. 94.

[5] H.W. Liu, R. Ferreira, G. Bastard, C. Delalande, J.F. Palmier, and B. Etienne, *Appl. Phys. Lett.* **54**, 2082 (1989).

[6] F. Sasaki and Y. Masumoto, *Phys. Rev. B* **40**, 3996 (1989).

[7] N. Vodjdani, D. Côte, D. Thomas, B. Sermage, P. Bois, E. Costard, and J. Nagle, *Appl. Phys. Lett.* **56**, 33 (1990).

[8] M. Cardona and G. Harbeke, *J. Appl. Phys.* **34**, 813 (1963).

[9] D.H. Chow, T.C. McGill, I.K. Sou, J.P. Faurie, and C.W. Nieh, *Appl. Phys. Lett.* **52**, 54 (1987).

[10] J.R. Söderström, D.H. Chow, and T.C. McGill, *Appl. Phys. Lett.* **55**, 1348 (1989).

[11] M. Sweeny and J. Xu, *Appl. Phys. Lett.* **54**, 546 (1989).

[12] J.R. Söderström, D.H. Chow, and T.C. McGill, *Appl. Phys. Lett.* **55**, 1094 (1989).

[13] G. Ripamonti, F. Capasso, and W.T. Tsang, *J. Appl. Phys.* **67**, 583 (1989).

[14] L.X. He, K.P. Martin, and R.J. Higgins, *Phys. Rev. B* **36**, 6508 (1987).

Chapter 5

Raman Scattering Determination of Strain in CdTe/ZnTe Superlattices

5.1 Introduction

5.1.1 Background

As discussed in Chapter 1, wide bandgap II-VI semiconductors are of interest because of their potential use as visible light emitters, with application to short wavelength optical storage and printing. The difficulties involved in doping these materials both p- and n-type to useful densities have hindered the development of homojunction devices. This has stimulated interest in heterojunction devices, such as superlattices [1]. CdTe/ZnTe is one system that has attracted attention as the two materials can be usefully doped opposite types and are readily grown by molecular beam epitaxy (MBE) [2] or organometallic vapour phase expitaxy (OMVPE) [3]. Previous work has shown that CdTe/ZnTe superlattices display intense, visible photoluminescence which is orders of magnitude brighter than that from corresponding $Cd_xZn_{1-x}Te$ alloys [4], while $Cd_{0.25}Zn_{0.75}Te$/ZnTe superlattices have recently demonstrated optically pumped, visible-wavelength, lasing at room temperature [5].

An important issue in the fabrication of CdTe/ZnTe heterostructures is the accommodation by elastic strain of the large 6 % lattice mismatch between the two bulk materials, without formation of significant densities of defects. Methods which have been used to determine the strain configuration include photoluminescence (PL) [4], x-ray diffraction [6], *in-situ* reflection high energy electron diffraction (RHEED) [6, 7], transmission electron microscopy (TEM) [8], and resonance Raman scattering [9]. In this chapter we present a study of strain in four CdTe/ZnTe superlattices by Raman scattering.

5.1.2 Summary of Results

The strain configuration in CdTe/ZnTe strained-layer superlattices has been measured by Raman scattering near resonance. The ZnTe-like longitudinal optical phonon energy in the superlattice is significantly shifted from the bulk value to lower energies, and the shift increases with increasing superlattice CdTe fraction. Unlike previous photoluminescence studies of the same samples[4] in which it was not possible to distinguish between unstrained and free-standing strain configurations, the Raman scattering data indicate that the superlattices are significantly strained. The observed shifts agree with calculations of strain shifts based on a free-standing strain distribution, and are consistent with previous studies using X-ray diffraction. In the free-standing strain distribution, the superlattices adopt an in-plane lattice constant that minimizes the strain energy of the superlattice, and is independent of the buffer layer upon which they are grown.

5.1.3 Outline of Chapter

In Section 5.2 we describe the superlattice samples. Section 5.3 describes the experimental setup, and Section 5.4 presents the results of measurements of phonon energies. Section 5.5 presents a discussion of the peak assignments, and discussion of the phonon energies. Finally, conclusions are summarized in Section 5.6.

5.2 Samples

The samples studied were grown on (100) GaAs substrates by MBE in a Riber 2300. Four samples were studied, with layer thicknesses from 23 to 56 Å, grown on a series of buffer layers that has been described previously [4]. The final buffer layer was CdTe for three of the samples, and $Cd_{0.46}Zn_{0.54}Te$ for the fourth. The superlattices each consist of 150 to 200 periods, or a total superlattice thickness between 1.1 and 1.6 μm. Sample layer thicknesses obtained by x-ray diffraction and energy dispersive spectroscopy (EDS) in Ref. [6] are listed in Table 5.1, along with the photoluminescence bandgaps observed at 5 K.

5.3 Experimental Setup

The experimental arrangement used is illustrated schematically in Fig. 5.1. An argon ion laser pumps a Coherent model 590 continuous (CW) dye laser, which is operated with the dye 4-dicyanomethylene-2-methyl-6-p-dimethylaminostyryl-4H-pyran, more commonly referred to as DCM. The dye concentration was 0.38 g/l, in a solvent consisting of 4.9 parts ethylene glycol and 1 part benzyl alcohol. A pump power of 5 W was used, with the Argon laser operating on all visible lines, and an output power of approximately 1 W was obtained. The laser energy was

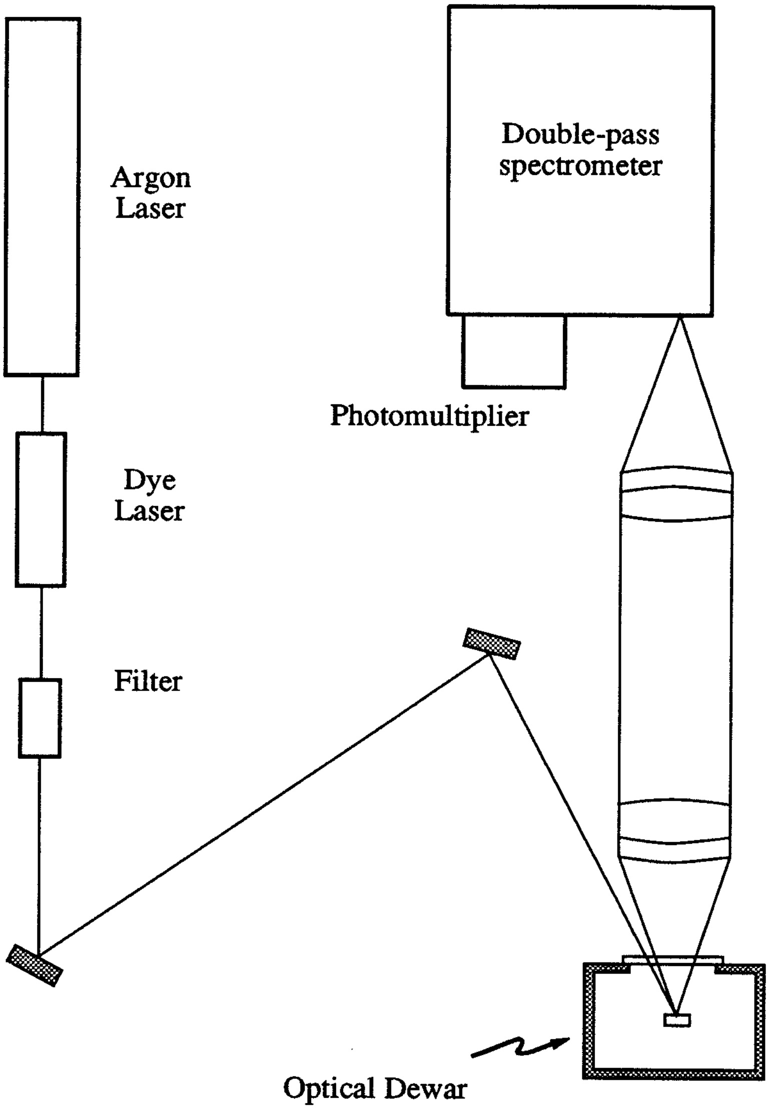

Figure 5.1: Experimental setup for Raman scattering. The output from the tuneable, continuous wave (CW) dye laser, is passed through a grating-slit filter, to remove the fluorescence background, and then focused on the sample. Scattered light is collected with aberration-corrected lenses, and then dispersed by a double-pass spectrometer, which is followed by detection with a GaAs photomultiplier tube and photon-counting electronics.

Sample	Superlattice (CdTe/ZnTe) (Å)	Buffer Layer	PL Bandgap (eV)	LZ_1 Phonon Energy (cm^{-1})
1	26/32	CdTe	1.87	202.4 ± 0.8
2	35/32	$Cd_{0.46}Zn_{0.54}Te$	1.74	199.0 ± 0.5
3	56/50	CdTe	1.69	199.5 ± 1.2
4	31/23	CdTe	1.81	197.4 ± 1.1

Table 5.1: CdTe/ZnTe superlattice sample parameters, observed photoluminescence bandgaps and LZ_1 phonon energies, at 5 K. Samples are ordered by increasing average CdTe content.

tuned with a three plate birefringent tuning element, yielding a linewidth less than $1.5\,cm^{-1}$ for all scans. To remove the fluorescence background, which interferes with the Raman scattering signal, the laser output was passed through a Spex Lasermate grating-slit filter. This filter, which has a bandpass of 12 Å, was readjusted for maximum throughput every time the dye laser energy was changed. Experiments were performed in a quasi-backscattering arrangement, with scattered light collected along the [100] growth direction. The incident beam was polarized along the [010] direction, at an angle outside the crystal of approximately 15° towards the [010] direction. No polarization analyzers were used on the collected light. Scattered light was dispersed with a Spex 1404 double pass spectrometer, and detected by a GaAs photomultiplier tube and photon counting electronics. In order to attain sufficient resolution to resolve the phonon energies to within a fraction of a millivolt, narrow spectrometer slit settings are necessary.

Because the intensity of the scattered light is very low in Raman scattering, it is important to couple as much of the scattered light as possible into the spectrometer. The use of precision doublet lenses, which are corrected for aberrations, and collection optics matched to the *f*-number of the spectrometer, were found to help the signal-to-noise ratio considerably. The incident laser energy for different scans was varied from just above the photoluminescence bandgap to higher energies at which the scattered light became too weak to be detected. All data were taken at 5 K in an atmosphere of helium.

5.4 Results

Typical Raman spectra for the four samples are shown in Fig. 5.2. The scattered intensity is shown as a function of the energy loss from the incident laser energy, and is plotted in the range corresponding to single optical-phonon scattering. The 0.8 Å resolution of the spectrometer is shown on the plots. All scans shown in Fig. 5.2 were taken with incident energies near resonance with the photoluminescence bandgap. It can be seen that the peak occurring at the highest energy loss shifts to lower energy as the CdTe content progressively increases from samples 1 to 4. The spectra show up to four peaks or shoulders, with the maxima in the scattered intensity occurring at the peak with the greatest energy loss in the scans shown. Peaks occurring at lower energy loss are more prominent in the spectra for samples 2 and 3. A linear dependence of the scattered intensity upon pump power was observed over a range of pump powers, confirming the expected behavior for Raman scattering, and distinguishing the observed peaks from photoluminescence, which showed a nonlinear dependence upon pump intensity.

Between five and eleven Raman scans were collected for each sample, with

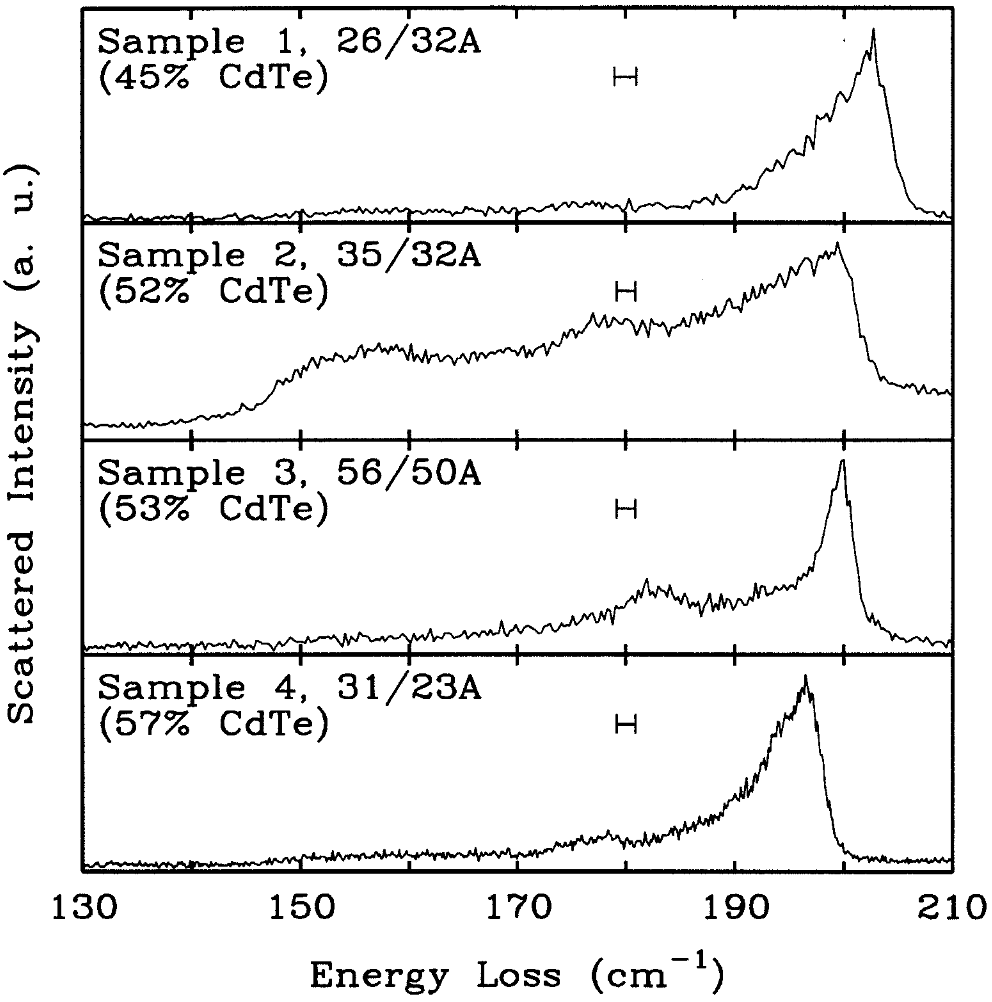

Figure 5.2: Representative near-resonance Raman scattering intensity at 5 K versus energy loss, in the range of single optical-phonon scattering. The peak occurring at the highest energy loss shifts to lower energies as the average CdTe content increases progressively from samples 1 to 4, due to the increasing strain in the ZnTe layers, and shifts the ZnTe-like phonon energy from its bulk value of 208 cm^{-1}. The laser energies for samples 1–4 were 1.965, 1.833, 1.818, and 1.849 eV, respectively. The spectrometer resolution, sample layer thicknesses, and CdTe volume fraction are shown on each plot for reference.

varying laser energies. The values of the energy loss at the highest energy-loss peak in the scattered intensity were averaged for all scans taken on a given sample. The results are summarized in Table I and plotted in Fig. 5.3 for the four samples. The positioning of the points along the horizontal axis in Fig. 5.3 is simply to group the experimental and theoretical results according to the sample, which are ordered by increasing CdTe fraction. The position of the highest energy-loss peak clearly varies with the average CdTe content of the superlattice. The observed energy loss at this peak is the highest in sample 1, which has the lowest average content of CdTe, and is the lowest in sample 4, which has the highest fraction of CdTe. Results for samples 2 and 3 fall between those for samples 1 and 4, but the two are quite close in average composition, and are difficult to distinguish from each other within the uncertainties in the measured values.

5.5 Discussion

To compare the experimentally observed phonon energies with theory, we have estimated the expected energies in the superlattice of the lowest confined longitudinal optical (LO) and transverse optical (TO) phonons propagating in the growth direction. The energies of phonons in a strained superlattice are affected by both strain and confinement, but for our structures the main contribution to the shift from the bulk phonon energies is due to strain, as will be shown in the following. The energy range of the highest-energy peaks observed is from approximately 196 to 203 cm^{-1}, which is quite close to the bulk value of 208 cm^{-1} for the LO phonon in ZnTe [11], and much greater than the value of 170 cm^{-1} for the LO phonon in CdTe [11]. We have therefore confined our attention to the ZnTe-like phonons, i.e., phonons confined in the ZnTe layers. Estimates of the effects of confinement on the LZ_1 mode (the highest-energy confined ZnTe-like

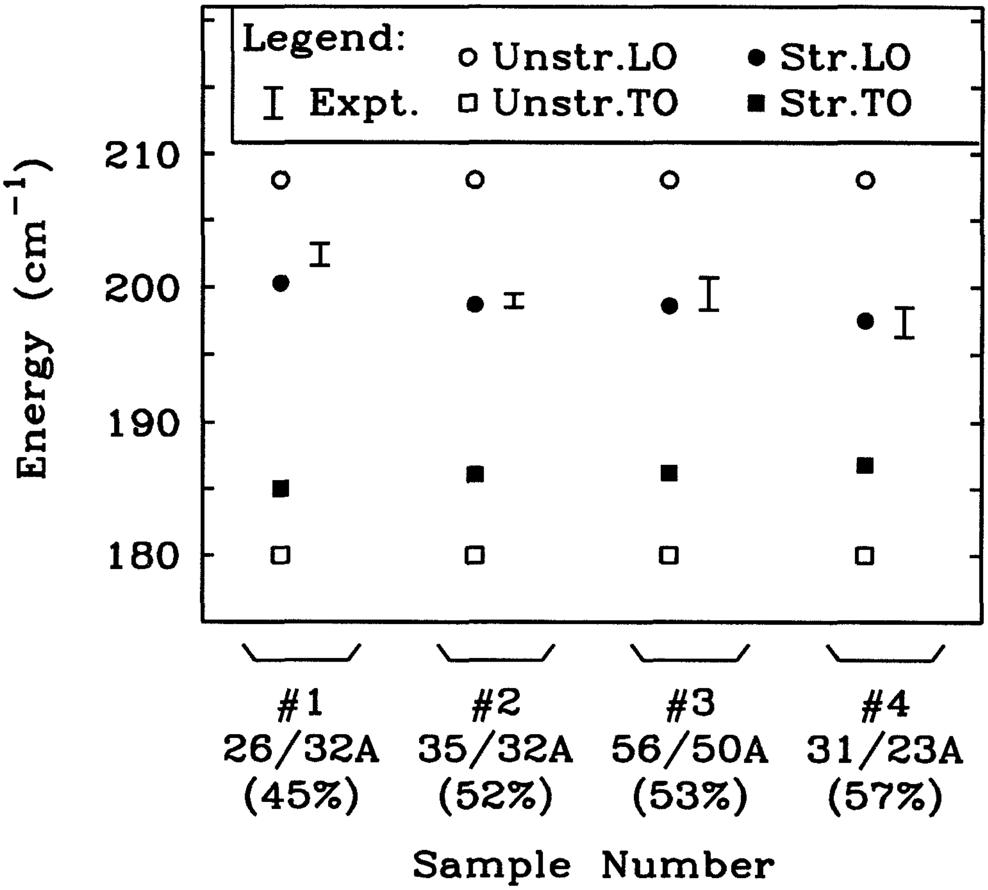

Figure 5.3: Comparison of theoretical with experimental results for the 4 samples, which are ordered by increasing CdTe volume fraction. Data points are the experimentally observed LZ_1 energies. The circles and squares are the bulk ZnTe LO and TO energies, respectively. The open symbols are the unstrained energies, and the filled symbols are calculated for strained bulk with strain appropriate to the free-standing superlattice. The points are positioned along the horizontal axis simply to group the experimental and theoretical results according to the sample.

optical phonon) using a simple spring-mass model of the longitudinal phonons propagating in the growth direction give energy shifts less than $1\,\mathrm{cm}^{-1}$ for the samples studied. Confinement effects on the TO-phonon energies are of a similar magnitude. This small contribution due to confinement has been neglected, which means that the lowest confined LO and TO phonon energies in the superlattice will occur approximately at the strained bulk LO and TO energies. The energies of the LO and TO phonons in strained bulk ZnTe are calculated using the method of Ref. [10]. From Ref. [9], the phonon deformation constants p and q are related to the mode Gruneisen parameter γ by $\gamma = -(\mathrm{p} + 2\mathrm{q})/(6\omega_{\mathrm{LO}}^2)$ and the shear deformation parameter a_s by $a_s = (\mathrm{p} - \mathrm{q})/(2\omega_{\mathrm{LO}}^2)$. We take $\gamma = 1.2$ and $a_s = 0.6$ [9]. Bulk LO and TO energies are taken from Ref. [11] to be: ZnTe LO, $208\,\mathrm{cm}^{-1}$; ZnTe TO, $180\,\mathrm{cm}^{-1}$; CdTe LO, $170\,\mathrm{cm}^{-1}$; CdTe TO, $145\,\mathrm{cm}^{-1}$.

The phonon energies for strained bulk ZnTe have been calculated for the four samples. The strain used in the calculation is that appropriate to a free-standing superlattice, i.e., the in-plane lattice constant is calculated to minimize the elastic energy of the whole superlattice, independent of the composition of the buffer layer on which the superlattice is grown. Values of the elastic constants for CdTe were taken from Ref. [12], and those for ZnTe from Ref. [13]. In Fig. 5.3, we plot the LO (circles) and TO (squares) ZnTe phonon energies for the four samples. The open symbols are the bulk unstrained phonon energies from Ref. [11], and the filled symbols are the bulk strained energies calculated as described above for a free-standing superlattice.

We assign the highest energy loss peak observed to the first confined ZnTe-like LO mode, LZ_1. As the LZ_1 mode is expected to have the highest energy of all the superlattice phonons, assignment of the highest energy loss peak observed to LZ_1 is unambiguous. However, assignment of the lower energy loss peaks observed is much less certain, as they occur at energies which could be assigned to various superlattice phonon modes. The significant shift of the LZ_1 energy from the unstrained value of 208 cm^{-1} indicates that there is significant strain of the ZnTe layers in the superlattices. Comparing the theoretical estimates of the ZnTe phonon energies shown in Fig. 5.3 with the observed values, we see that there is good agreement with the strained LO-phonon energy calculated for the free-standing strain configuration. This is consistent with previous conclusions[4, 6] based on photoluminescence and x-ray measurements. If the ZnTe superlattice layers in our samples were strained to the buffer layer lattice constant, then the energy of the LZ_1 phonon would be the same for samples 1, 3, and 4, and would be much lower than the position observed. The calculated position of the LZ_1 phonon for sample 2, if it is assumed to be lattice matched to the $Cd_{0.46}Zn_{0.54}Te$ buffer layer would be 195 cm^{-1}, which does not agree with the observed position.

Although interface modes in unstrained superlattices have been studied [14, 15, 16], little work has been done in heavily strained superlattices. In unstrained superlattices, interface modes are located between the bulk LO and TO energies. As the highest energy loss peaks observed in our samples occur in the range between the bulk ZnTe LO and TO energies, where interface modes are expected to occur, there is a possibility that they are in fact due to an interface mode, and not to a confined LO mode. If the interface modes in strained superlattices occur at energies determined solely by the bulk LO and TO phonon energies, and are independent of the strain, then no shift with increasing average CdTe content should be observed, which does not agree with the observations. On the other hand, if the interface modes occur at energies determined by the strained LO and TO energies, then some dependence on the average CdTe content might be observed. However, by considering the strained ZnTe LO and TO energies shown in Fig. 5.3, we see that an interface mode occurring at some position midway between the two energies would be at an energy consistently lower than the observed peak positions. Hence, we think it unlikely that the highest energy loss mode observed is an interface mode.

It should be noted that the free-standing strain configuration demonstrated in this chapter is at variance with results reported in a previous CdTe/ZnTe resonant Raman scattering study [9]. Although direct comparison of the two studies is complicated by differences in sample thicknesses and growth conditions, previous structural studies[6] draw into question the conclusions of Ref. [9]. Implicit in the derivation of strains from Raman peak shifts is the assumption of homogeneous strains within like superlattice layers. Structural studies [6] of the superlattices examined here reveal that strain relaxation is not confined to the superlattice/buffer-layer interface, as growth is highly dislocated and nonuniform within approximately one-half micron of this interface. However, a substantial improvement in crystal structure appears beyond this region, as evidenced by TEM [8], *in-situ* RHEED [6, 7], and x-ray diffraction measurements [6]. As the samples used in this study consist of 1.1 to 1.6μm thick superlattices, and the above bandgap light used is sensitive mainly to the surface region, the assumption of strain homogeneity in this work appears sound. The basis of this assumption of uniformity is less clear in the work of Ref. [9], however, as the samples studied were much thinner (less than 0.25μm). Thus, while it is possible that the particular superlattice layer thicknesses chosen in Ref. [9] yielded one superlattice that was coherent with the buffer layer, it is unlikely that another superlattice which was shown to relax had a well-defined strain configuration so close to the superlattice/buffer-layer interface. The relaxation of a thin superlattice to a single free-standing lattice constant for all the superlattice layers would require the nucleation of a large number of defects only at the superlattice/buffer-layer interface, immediately followed by growth at a single in-plane lattice constant.

5.6 Conclusions

In conclusion, we have used near-resonance Raman scattering to measure the confined ZnTe-like phonon energy in four CdTe/ZnTe superlattices. Observed phonon energies are shifted from the bulk energies by amounts that increase with increasing superlattice CdTe content, and indicate that the superlattices are highly strained. Observed energies are in agreement with calculations of the expected phonon energies that account for strain, and indicate that the superlattices relax to a free-standing configuration.

References

[1] R. H. Miles, J. O. McCaldin, and T. C. McGill, *J. Cryst. Growth* **85**, 188 (1987).

[2] G. Monfroy, S. Sivananthan, X. Chu, J. P. Faurie, R. D. Knox, and J. L. Staudenmann, *Appl. Phys. Lett.* **49**, 152 (1986).

[3] D. W. Kisker, P. H. Fuoss, J. J. Krajewski, P. M. Amirtharaj, S. Nakahara, and J. Menéndez, *J. Cryst. Growth* **86**, 210 (1988).

[4] R. H. Miles, G. Y. Wu, M. B. Johnson, T. C. McGill, J. P. Faurie, and S. Sivananthan, *Appl. Phys. Lett.* **48**, 1383 (1986).

[5] A. M. Glass, K. Tai, R. B. Bylsma, R. D. Feldman, D. H. Olson, and R. F. Austin, *Appl. Phys. Lett.* **53**, 834 (1988).

[6] R. H. Miles, T. C. McGill, S. Sivananthan, X. Chu, and J. P. Faurie, *J. Vac. Sci. Technol. B* **5**, 1263 (1987).

[7] G. Monfroy, X. Chu, M. Lange, and J. P. Faurie (unpublished).

[8] P. M. Petroff (unpublished).

[9] J. Menéndez, A. Pinczuk, J. P. Valladares, R. D. Feldman, and R. F. Austin, *Appl. Phys. Lett.* **50**, 1101 (1987).

[10] F. Cerdeira, C. J. Buchenauer, F. H. Pollak, and M. Cardona, *Phys. Rev. B* **5**, 580 (1972).

[11] D. J. Olego, P. M. Raccah, and J. P. Faurie, *Phys. Rev. B* **33**, 3819 (1986).

[12] H. J. McSkimin and D. G. Thomas, *J. Appl. Phys.* **33**, 56 (1962).

[13] D. A. Berlincourt, H. Jaffe, and L. R. Shiozawa, *Phys. Rev.* **129**, 1009 (1963).

[14] A. K. Sood, J. Menéndez, M. Cardona, and K. Ploog, *Phys. Rev. Lett.* **54**, 2115 (1985).

[15] S.-F. Ren, H. Chu, and Y.-C. Chang, *Phys. Rev. B* **37**, 8899 (1988).

[16] H. Chu, S.-F. Ren, and Y.-C. Chang, *Phys. Rev. B* **37**, 10746 (1988).

Appendices

Appendix A

Colliding Pulse Mode-Locked Laser

A.1 Introduction

A.1.1 Background

In this appendix we will discuss the colliding pulse mode-locked (CPM) dye laser, which is the source of ultrafast pulses used in the work described in this thesis. Before discussing the CPM, however, we will briefly review sources of short optical pulses that are currently available. Since the first demonstration in 1960 of lasing action in ruby [1], the laser has proved to be an invaluable tool in scientific studies, because it provides a unique source of coherent optical radiation. In 1964 and 1965 it was realized that the longitudinal modes of the laser, could be locked together (mode-locked) to create short pulses [2]-[4]. By forcing a number of cavity modes to oscillate with a fixed phase relationship, periodic pulse trains can be formed with pulse widths inversely proportional to the frequency width of the laser spectrum. Since 1965 there has been great progress in mode-locking of lasers, and at the present there are a wide variety of techniques used [5]-[7], which we will examine in the following paragraphs.

Active mode-locking uses external radio-frequency modulation of cavity loss or phase, with a period corresponding to the round-trip delay for light travelling around the optical resonator. This type of mode-locking is commonly used in argon ion, krypton ion, Nd:YAG (trivalent neodymium ions in a host yttrium aluminum garnet, $Y_3Al_5O_{12}$ crystal) or Nd:YLF (neodymium in yttrium lithium fluoride, $LiYF_4$) lasers, which can produce relatively high average output powers (1-20 W) with pulse widths on the order of fifty to several hundred picoseconds. These lasers operate at a finite number of frequencies, characteristic of the line spectrum of the gain medium, that cover the range from $1.06\,\mu$m (Nd:YAG, Nd:YLF) to the blue region of the spectrum (argon and krypton). Active mode-locking of semiconductor injection lasers is also possible, and can be achieved by high-frequency modulation of the drive current, to produce pulses as short as 20 ps [8, 9].

Synchronous pumping is another form of mode-locking, based on periodic optical modulation of the laser gain by another mode-locked laser. The typical pump laser in such systems is an actively mode-locked ion, or frequency-doubled Nd:YAG (or Nd:YLF) laser, and the synchronously pumped laser is most often a dye laser. Mode-locking in these lasers is due to the periodic modulation of the dye laser gain by the absorption of pump photons, requiring close matching of the period of the pump laser to that of the dye laser. This stringent matching requirement is a major practical difficulty with synchronously pumped lasers, and has prompted some companies to incorporate active cavity length stabilization schemes in commercial products [10]. The large organic dye molecules used in such systems have a very wide gain spectrum (extending for example from approximately 5400 to 6600 Å in Rhodamine 6G [11], a typical commercially available dye) which allows formation of very short pulses. In addition to the wide tunability of any given dye, a great variety of dyes are available spanning the entire visible spectrum, and extending into the near infrared [12]. Synchronously pumped dye lasers are tunable over a wide range, produce up to 500 mW average output power (when pumped by approximately 2 W), and produce pulses as short as 220 fs [10].

Another approach to mode-locking, which is used to generate the shortest optical pulses, is known as passive mode-locking. Passive mode-locking, which does not involve any externally modulated elements in the optical cavity, arises from the presence of a saturable absorber* in the laser cavity. When the cavity starts lasing, but before mode-locking is established, many longitudinal modes oscillate with random phase. The randomly oscillating modes will occasionally have a phase relationship that results in an increased intensity, due to constructive interference, at the saturable absorber. When this occurs, saturation of the absorber results in decreased cavity loss, and subsequent increase of the intensity of the modes that have the phase relationship required to saturate the absorber. This process continues to preferentially amplify the modes that are phase-locked, and finally results in stable mode-locking and pulse formation [13]. The advantages of the passively mode-locked laser include formation of the shortest optical pulses, tolerance of fluctuations of the total cavity length (in contrast to synchronously pumped systems), and compatability with CW pumping schemes using lasers, or flashlamps. Passive mode-locking is used in high-power solid-state lasers such as ruby [14] and Nd:glass [15], where the output pulse energies can be as large as 10 mJ per pulse with pulse widths of 2 to 20 ps. Passive mode-locking is also used in dye lasers [16], and has produced pulses as short as 27 fs in the CPM dye laser

---

*An absorbing dye whose opacity decreases with increasing incident optical power

[17]. The main difficulty with passive mode-locking is the required matching of the nonlinear properties of the saturable absorber to a particular gain medium. This has limited the spectral range that can be accessed by passively mode-locked dye lasers to less than that which can be achieved with synchronously pumped dye lasers. French et al. [18] have developed several dye-absorber combinations producing pulses shorter than 1 ps and spanning the range from 4900 to 8000 Å, although not all intermediate wavelengths are accessible. In the red to near infrared portion of the spectrum, recent developments of the Ti:Al_2O_3 laser show great promise. The extremely broad gain spectrum in Ti:Al_2O_3 covers the entire range from 6800 Å to 1.05 μm [19]. Passively mode-locked Ti:Al_2O_3 lasers have generated 1.4 ps pulses using nonlinear optical effects in a fiber-optic external cavity [20], or 4 ps using a saturable dye jet [21]. Finally, passive mode-locking has been used to produce trains of mode-locked pulses as short as 0.65 ps from semiconductor diode lasers [22]-[24]. The origin of the saturable nonlinearity used to cause mode-locking in semiconductor lasers has varied, and has included dark line defects in the laser caused by aging [22], defects created by intentional proton bombardment of the laser [23], and multiple quantum wells placed in an external cavity [24].

In addition to the ability of mode-locked lasers to provide short pulses, the output from such a laser may subsequently be amplified [25], or modified to shorten the pulses, or change the wavelength and bandwidth pulses. This allows the production of ultrafast laser pulses with wavelengths, pulse lengths, and energies unavailable directly from mode-locked lasers. Pulse shortening using nonlinear properties of optical fibers, in conjunction with diffraction gratings [26], or diffraction gratings and prisms [27], can significantly reduce optical pulse widths. The shortest optical pulse ever generated, with a width of 6 fs, was produced by compressing the output of a CPM dye laser [27]. In addition to the use of nonlinear processes for pulse compression, there are a wide variety of nonlinear optical processes that can be used to shift the wavelength of mode-locked lasers. For example, second harmonic generation using a mode-locked Nd:YAG laser operating at $1.06\,\mu$m produces pulses at 5320 Å, and tripling the output frequency is also practical. The high peak powers available with mode-locked lasers make such nonlinear processes quite efficient, and conversion efficiencies greater than 10% are possible. Similar mixing processes can be used to combine the output more than one laser (typically a synchronously mode-locked dye laser and its pump laser), to produce tunable pulses in spectral regions inaccessible by other means. Parametric oscillators, also based on nonlinear processes, have been used to generate tunable subpicosecond pulses, and show potential tunability over the range from 0.72 to $4.5\,\mu$m [28, 29]. The technique of continuum generation, based on self-phase modulation in ethylene glycol or water jets, is a very powerful technique for generation of ultrafast pulses. The pulses created with this technique are spectrally broadened, possessing components extending over the entire visible spectrum, while maintaining pulsewidths as short as 80 fs [30]. These provide a unique source of ultrafast pulses that can be used to make time-resolved absorption measurements.

In summary, there are many ways of producing short optical pulses by direct generation using a mode-locked laser. Subsequent modification of a mode-locked laser output can consist of amplification, pulse compression, or nonlinear conversion to other spectral regions. This field has advanced extremely rapidly in the last 10 years, and reliable sources of short optical pulses are becoming increasingly available.

A.1.2 Outline of Appendix

The appendix begins with Section A.2, a brief description of the operating principles of a CPM laser. Section A.3 describes some design considerations for a CPM laser. Section A.5 presents a detailed procedure for aligning the laser. Section A.6 describes routine maintenance procedures necessary in day to day use of the laser, and finally, Section A.7 describes the performance of the laser.

A.2 Operating Principles

The CPM dye laser used in the present work, and described in this appendix, is a passively mode-locked dye laser. An excellent description of the CPM laser is presented in Ref. [31], and a more theoretical analysis is given in Refs. [32] and [33]. The content of these papers will not be reproduced here, but a brief summary will be presented.

The CPM laser, illustrated in Fig. A.1, uses a ring cavity, a gain dye jet, a saturable absorber dye jet, and dispersion compensation. Based on the original demonstration of passive mode-locking of dye lasers by Ippen et al. [16] the CPM ring resonator was the first to produce pulses shorter than 100 fs [34]. Theoretical work by Martinez et al. [32, 33] suggested that the proper balancing of self-phase modulation (SPM), which occurs due to nonlinearities in the dye jets, and group velocity dispersion (GVD) in the cavity could lead to soliton-like pulse shaping [36]. Valdmanis et al. demonstrated this behavior, producing pulses as short as 27 fs [17, 31]. One of the important advances was to use a four-prism sequence [35] to add a continuously adjustable negative group velocity compensation to the cavity. At the time of writing, the 27 fs pulses produced by the dispersion-compensated CPM laser are the shortest directly produced by any mode-locked

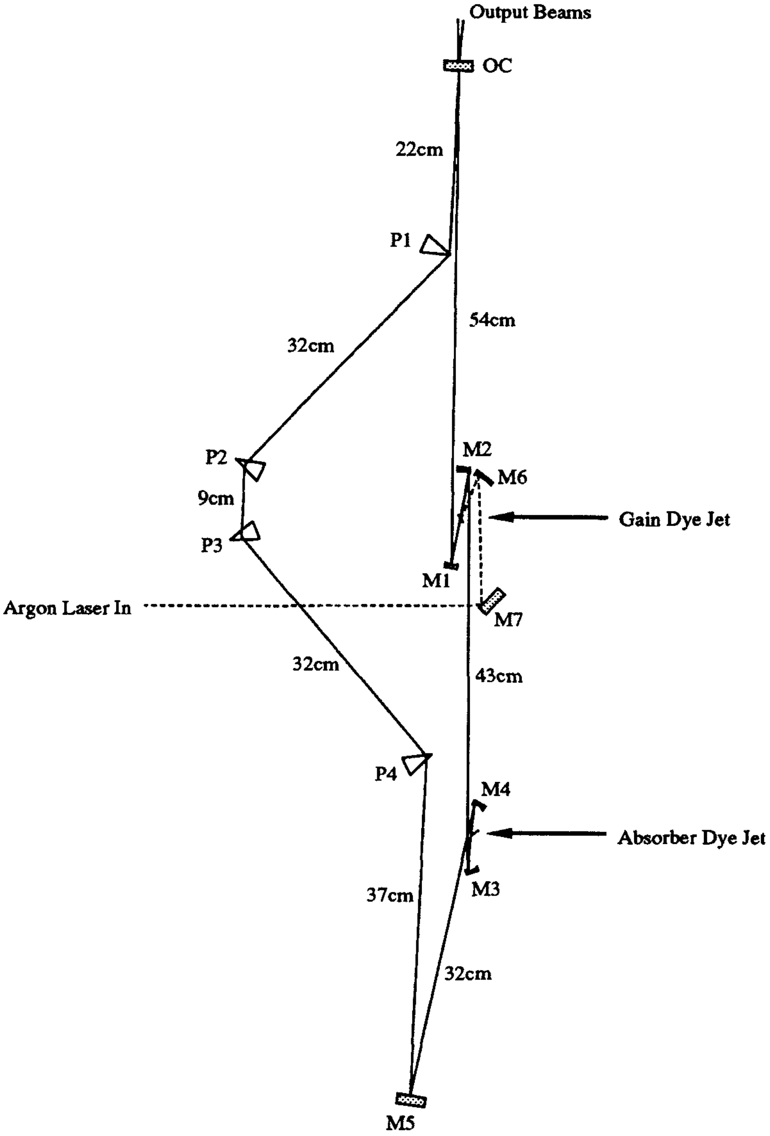

Figure A.1: Plan view diagram of the 6-mirror CPM laser (to scale). Mirrors M1 and M2 (the gain cavity), and mirrors M3 and M4 (the absorber cavity), are separated by approximately 10 and 5 cm, respectively. Prism sequence P1-P4 is used for group velocity dispersion compensation. The angles formed by the beam travelling along M2-M1-OC, and M1-M2-M3, are 5°, and angles M2-M3-M4 and M3-M4-M5 are 7°.

laser.

The experiments described in this thesis were performed with two similar variants of the CPM, one with seven mirrors, and one with six; dispersion compensation was used in some experiments, and not in others. The most satisfactory operation of the laser was obtained with the dispersion compensated 6-mirror cavity shown in plan view in Fig. A.1. The entire CPM laser is mounted on a 2×4 ft optical breadboard. The two dye jets flow from stainless steel nozzles, and fall vertically through holes in the optical breadboard where they are collected and recirculated continuously. The output at 5145 Å of a CW argon ion laser is directed by flat mirror M7, and focused onto the gain dye jet by mirror M6 (radius R=10 cm). The pump laser is polarized parallel to the optical breadboard, and the dye and absorber jets are both oriented at Brewster's angle with respect to the intracavity beam. Both M6 and M7 are coated for peak reflectivity at 5145 Å and normal incidence. The cavity formed around the gain jet by mirrors M1 and M2 (R=10 cm each) serves to focus the intracavity beam to a waist at the gain jet that is coincident with the pump beam. Mirrors M4 and M5 (R=5 cm) similarly focus the intracavity beam to a waist at the absorber jet, with the shorter focal length of the pair resulting in a smaller beam waist at the absorber than the gain jet. Mirror M5 is a high reflector (HR) and the partially transmissive output coupler OC couples a small fraction of the intracavity beam out of the laser. Several values of the output coupler transmission were used, but the most reliable operation was obtained with 2% transmission. With higher output coupler transmission, the output power for a given intracavity intensity is higher; however, the additional loss makes it increasingly difficult to achieve high enough intracavity intensities to cause the nonlinearities necessary for mode-locking. Although multistack dielectric mirror coatings are normally used to give high reflectivity over a wide bandwidth, the dispersion caused by these mirrors result in pulse broadening in the CPM [31]. Accordingly, single stack dielectric coatings were used for all intracavity mirrors, optimized for peak reflectivity at 6328 Å and normal incidence. Prism sequence P1-P4 is used to provide adjustable group velocity dispersion. The four-prism sequence provides a net negative group velocity dispersion (GVD), because of the geometrical arrangement of the prisms [35]. In addition, the material dispersion of the prisms (which are made from Schlieren grade fused silica) results in positive GVD proportional to the distance the intracavity beam travels through the prism material. Since both prism faces are oriented at Brewster's angle to the intracavity beam, the prism may be translated perpendicular to their base without producing deviation of the intracavity beam. This allows a variable amount of prism material to be added to the cavity, by translating one of the prisms perpendicular to its base, while lasing is sustained. This enables continuous adjustment of the total cavity GVD for formation of the shortest pulses, or the greatest stability.

During mode-locked operation, the intracavity beam in the laser consists of two counterpropagating pulses, which collide at the absorber jet, once per roundtrip. The pulse formation process that leads to stable mode-locking in the CPM is quite complex, and is similar to soliton propagation in optical fibers [36]. The self-phase modulation (SPM) in the dye jets, combined with the appropriate GVD, leads to stable formation of short pulses. As with solitons in optical fibers, stable pulse shortening (and mode-locking) is only possible for negative GVD, and the correct adjustment of the intracavity prism material is crucial to stable operation of the laser. A highly asymmetric dependence of pulse formation upon the sign of the GVD is observed in such lasers, and no stable formation of pulses is possible if the net GVD is positive [31]. This characteristic behavior is easily observed in the laser spectrum, which becomes progressively wider (indicating narrowing of the pulses) as the GVD is made more positive, until the shortest pulses are formed. Further positive GVD results in an abrupt shift of the laser spectrum, and disappearance of the laser autocorrelation trace, which are indicative of loss of mode-locking.

A.3 Design Considerations

In this section we will discuss some aspects of the implementation of a CPM laser. The 6-mirror CPM laser was constructed by modifying a 7-mirror CPM constructed by M.B. Johnson [37]. Many of the aspects of the design were well described in Ref. [37], and will not be reproduced here. We will concentrate upon the modifications made to the laser, and the rationale behind them.

One of the main reasons for choosing the 6-mirror cavity was because of difficulties in obtaining a symmetrical and stable Gaussian spatial mode with the 7-mirror cavity. Stable transverse mode formation, which is essential for the PECS measurements described in Chapter 2, is easier in the 6-mirror CPM because of decreased astigmatism [31, 38]. The astigmatism in the CPM originates in the use of spherical lenses for off-axis focusing in the dye and absorber cavities formed by M1 and M2, and M3 and M4, respectively. This off-axis placement leads to astigmatism because rays in the saggital and tangential planes are focused at different points [39]. In CW dye laser cavities, this astigmatism can be corrected by the presence of the dye jet, which is also asymmetrical with respect to interchange of the tangential and saggital planes [40]. Such compensation is not possible in the CPM, because of thin dye and absorber jets necessary for mode-locked operation and formation of short pulses. Therefore, in a CPM it is important to use the spherical mirrors as close to normal incidence as possible, by reducing the fold angles around the dye and absorber cavities as much as possible. Because the radius of curvature is smaller in the absorber cavity (M3 and M4), the astigmatism is more severe than at the gain jet. The minimum fold angles are determined by the requirement for clearance of the collimated beams (between M2 and M3, and between M4 and M5) around the absorber jet. The coma-compensated absorber cavity in the 6-mirror CPM allows the absorber jet to be placed asymmetrically, using a portion of the jet closer to the edge, and thus allows smaller fold angles than the "Z" absorber cavity used in the 7-mirror CPM.

In addition to the reduced astigmatism possible with the 6-mirror CPM, there are other cavity parameters that affect the spatial mode of the laser. In order to achieve efficient coupling of the pump laser to the intracavity mode, it is necessary to focus the pump to a small spot on the gain jet. This results in heating of the ethylene glycol solvent, and thermal lensing (also known as thermal blooming because of the increased size of the transmitted pump spot at the onset of thermal effects). This thermal lensing that occurs in the gain jet can affect the alignment of the optical resonator. It is necessary, then, to align the resonator using low pump powers (1-2 W), where thermal lensing is less important. Finally, when mode-locking is desired, the pump power is increased to 4-5 W, and the absorber dye is added. At high pump power, and in the absence of the absorber dye, the spatial mode of the laser will be asymmetrical and poor, because of the thermal blooming. However, addition of the absorber improves the mode dramatically, and the same spatial mode obtained at low powers in the alignment procedure can be recovered when pumping at high powers. This is because the Gaussian intracavity beam profile saturates the absorber dye more at the center of the beam than at the edges, resulting in a "soft aperture" around the beam at the absorber jet, which controls the spatial mode very nicely.

In addition to problems with the spatial mode, fluctuations in the output power, and loss of mode-locking were problems with the laser. In a properly constructed CPM, the main sources of noise are the pump laser fluctuations, and mechanical instabilities of the dye jets [41]. In order to reduce instabilities in the dye jets, it is important to pay attention to the pumping mechanism, and the manner in which the flowing dye is collected after the dye nozzle. The pumping scheme used, described in detail in Ref. [37], involves pulsation dampening, and dye accumulation. This was modified somewhat in the present work by mechanically isolating the pulsation dampener and accumulator from the vibrations of the pump motor. It has been suggested [38, 41, 42] that the correct design of the dye catching tube is important. This is necessary in order both to avoid foaming of the dye upon contact with the catcher tube, and also to create a stable flow pattern that does not suffer from instabilities. To accomplish this, custom-made glass catching tubes were fabricated, paying particular attention to the smooth flow of dye from the point where it strikes the surface of the glass. The nozzles used to create the dye jet have an opening approximately $0.3\times2\,\mathrm{mm}$ (gain jet) and $0.12\times2\,\mathrm{mm}$ (absorber jet). This produces a thin flat jet that flares out in width after exiting the nozzle. Further from the nozzle, a series of nodes and antinodes are formed, where the jet changes both in width and the orientation of the flat surface. To minimize instabilities, the glass catching tube was positioned so that the dye jet struck the tube at a glancing angle, and at a node in the jet flow pattern.

The use of a 6-mirror CPM required some design changes in the optics and the optical mounts. In order to reduce the "Z" fold angles in the gain cavity (M1 and M2), and keep the pump and intracavity beams as close to collinear as possible, mirror M2 was cut in half, yielding a D-shaped mirror approximately 7 mm across. Because mirrors M1 through M4 are only adjusted infrequently, and to prevent accidental misalignment, these mirrors were mounted in Newport OEM mounts, which are adjusted by set screws. Although this complicates the alignment procedure somewhat compared to precision micrometer mounts, it reduces any subsequent temptation to readjust these mirrors once they are correctly set. These mounts are also much more compact, and cheaper than precision mounts. Mirrors M1-M4 were all mounted on translation stages, that allowed the motion of the mirrors towards the dye jet, which is essential in alignment of the laser. In particular, it was found to be helpful to have M2 mounted on such a stage, to allow adjustment of the resonator mirrors while leaving the focusing of the pump laser (by M6) and the position of the gain jet unperturbed.

A recurring problem with the CPM was the accumulation of dust on the optics, due to the fairly high levels of dust in the laboratory. This caused problems when dust particles landed on the optics, which occasionally resulted in diffraction of the intracavity beam, and affected operation of the laser. Because this problem was fairly common, and nearly impossible to diagnose, the entire 2×4 ft optical breadboard was mounted under a Dexon filtered blower. The blower and filter were mounted to the laboratory roof using unistrut beams, and plastic curtains were hung from the blower to the breadboard. This approach solved the problem with dust, which greatly reduced the required amount of cleaning of optics (along with the associated misalignment and wear). However, the high air flow was found to affect the jets, and resulted in a fluctuations in the jet positions. This effect was minimized by reducing the airflow to the absolute minimum required to exclude dust, which was easily determined during operation due to scattering of the intracavity beam by the dust.

A.4 Diagnostic Equipment

Several pieces of equipment are useful in diagnosis of the CPM. In order to observe the spatial mode, one or more lenses are used to magnify the output of the laser, and project the magnified image upon a screen or wall. It is most helpful if the magnified mode is quite large (20-40 cm in diameter) and easily accessible for close inspection and measurement. As will be described in Section A.5, the adjustment of the gain and absorber cavity mirror separation affects the size of the mode, and detailed observations of the size, shape, and stability of the mode during alignment are essential. Perhaps the most powerful diagnostic tool, and also one of the simplest, is a diffraction grating, arranged to project the laser spectrum onto a screen or wall. The wavelength scale of diffracted pattern can be calibrated, and serves both as an indication of whether mode-locking is occurring, and of the length of the pulse. A photodiode with sufficiently fast response to resolve pulses separated by the cavity round trip time of 10 ns is useful, and is routinely monitored during laser operation. This allows the detection of "double-pulsing," where mode-locking is incomplete and pulses are formed in the cavity at twice the round trip frequency, as well as loss of mode-locking. The photodiode also allows observation of rapid (1-50 Hz) fluctuations in the laser output power. Finally, an autocorrelator is useful for absolute calibration of the laser pulsewidth, and as a check of proper mode-locking. The autocorrelator used in the present work was constructed using a stepper motor to adjust the length of the moveable arm of the interferometer, and the autocorrelation was obtained by recombining the beams in KDP, a crystal used for second-harmonic generation (SHG). The SHG signal was detected by a photomultiplier tube (after filtering to remove the red components of the beam), and displayed on an oscilloscope. The stepper motor was rapidly scanned under control of an IBM PS/2 Model 80 microcomputer, which supplied pulses to the stepper, and also output a voltage proportional to the stepper position, for the oscilloscope display. The stepper motor arrangement was sufficiently stable to generate an interferometric autocorrelation trace [43, 44], while scanning the autocorrelation trace faster than once per second. Metal-coated retroreflectors were used (Newport "BBR"), because they preserve the polarization of the beam. This is important because the reflectivity of the beam splitter used is a function of the polarization of the incoming light, and rotation of the polarization by solid retroreflector cubes based on total internal reflection results in differences between the intensities of the two recombined beams. The degree of mode-locking can be ascertained from the peak-to-background ratio of the autocorrelation trace [5], and the pulsewidth can be obtained from the autocorrelation full width at half maximum (assuming a $sech^2$ pulse shape [32, 33]) by dividing by 1.55.

A.5 Alignment Procedure

This alignment procedure is intended to be used only when the laser is aligned from the very beginning. It is not intended to be performed on a regular basis, and in fact, a major portion of the development work on this laser was to develop operating procedures which avoided this tedious alignment procedure. It is possible to align a CPM laser once, and then routinely replace the dyes and adjust only the positions of the saturable absorber jet, and the dispersion compensating prisms, in order to return to standard operating conditions. The routine maintenance procedures are described in Section A.6.

The final 6-mirror, coma-compensated cavity shown in Fig A.1 is a complicated optical resonator. It contains two dye jets, eight mirrors (six in the cavity, and two for the pump beam), and four prisms. With x, y, and z translational, and either two or three rotational degrees of freedom, there are more than fifty degrees of freedom in the optical alignment alone. In addition, there are dye concentrations, jet pressures, and the optical pump power. In order to make this problem manageable, it is necessary to build the final mode-locked laser up from the simplest possible CW laser, in a series of stages. At each stage, it is important to focus one's attention on the correct alignment of a small, manageable subset of the degrees of freedom, with clear objectives and ways of determining their achievement. Once a subset of the cavity parameters/positions has been determined, it is possible to move on to add more components, and for the most part, to leave settings already determined alone.

A.5.1 Linear Cavity, Gain Only

Alignment commences with the simple linear cavity shown in Fig. A.2(a). At first, only ethylene glycol (EG) is circulated through the gain jet, at a pressure of approximately 60 psi. The argon pump (run at a power of 2 W) beam is aligned from M7 to M6 to be parallel to the optical table. Although it is expected that best operation be obtained when the pump beam strikes M6 as close to the edge near M2 as possible, higher output power from the linear cavity was obtained when the beam struck M6 approximately 1 cm from the edge of M2. The same height from the table used for the pump beam will be used for all beams in the cavity, and it is helpful to have a metal ruler with a small hole drilled in it at the height desired. Mirror M6 is adjusted so that the beam is focused slightly before the jet, and is centered on a flat portion of the jet, avoiding the edges, where the jet is thicker and more unstable. The dye used was Rhodamine tetrafluoroborate, a variant of the R6G laser dye (which is based on a chloride version of the same dye molecule). A sufficient quantity (4 g) of Rhodamine dye is dissolved in 200 ml of methanol, and heated slightly to aid the dissolving of the dye. Once dissolved, 200 ml of EG is added to the mixture, and it is left on a hotplate (at low heat) for several hours, to evaporate the methanol. This supersaturated stock solution is then slowly added to the pure EG circulating in the gain jet, until the pump

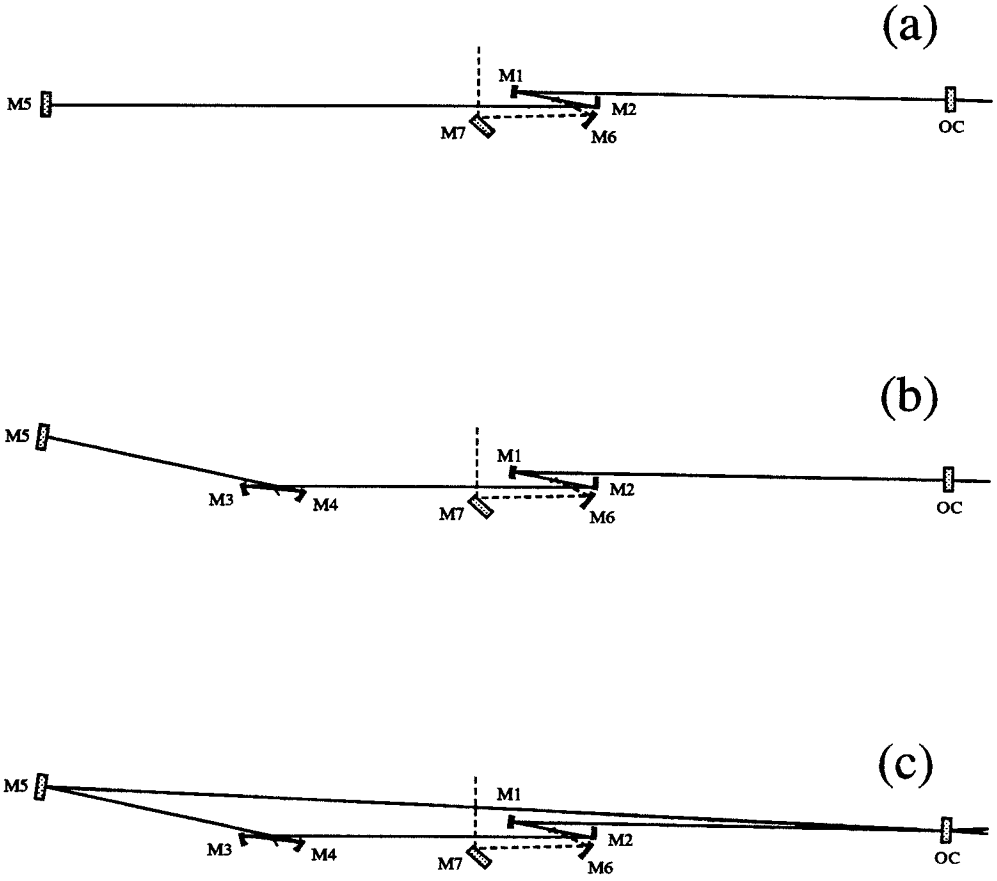

Figure A.2: CPM configuration during alignment. (a) Linear cavity, (b) Linear cavity with gain and absorber jets, (c) Ring cavity with gain and absorber. The figure is drawn approximately to scale.

laser transmission is 5%. It is important to check the shape of the transmitted pump beam to ensure that no evidence of thermal lensing is evident at this stage. Also, the jet should be oriented at nearly Brewter's angle to the pump; this can be determined by monitoring the pump reflection from the jet surface. It is also necessary that the flat region of the jet be oriented perpendicular to the table surface, which can be determined by measuring the height of the beam reflected from the surface. It was found that a concentration of 1.48 g/l yielded the required 5% transmission. Once the required dye concentration is attained, pump beam should be focused slightly before the jet, and slightly before the onset of thermal lensing. It is necessary, however, to be very close to the onset of thermal lensing in order to get sufficient coupling to allow proper mode-locking at later stages.

With the pump beam striking the gain jet, bright fluorescence will be emitted from the pumped volume. This fluorescence will be imaged by M1 (towards OC) and M2 (towards M5), and is used to align M1 and M2. To align M1, an iris approximately 2 mm in diameter is placed near M2, at the height and position desired for the final intracavity beam. The fluorescence imaged through this iris is viewed on a card placed near OC, and aligned to the desired intracavity beam height. Then M1 is translated towards the jet until the fluorescence spot is focused at a distance on the order of approximately 2 m (place a flat mirror between M1 and OC to determine this, without having to remove OC). M2 is aligned using the same procedure, placing an iris as close to M7 as possible, and translating M2 until the fluorescence spot is focused at the same distance used in aligning M1 (approximately 2 m). Now M5 and OC are adjusted to obtain lasing by retroreflecting the fluorescence spots through the irises and back into the jet. When aligning OC, it is helpful to view the fluorescence spot imaged on M5; when OC is correctly aligned, a brighter spot will be seen. Similarly, align M5 while viewing the fluorescence spot on OC. When the irises are opened, lasing should be observed, and M5 and OC should be adjusted to obtain maximum power. The dye jet should be rotated until it is at exactly Brewster's angle to the intracavity beam, which can be determined by observing the reflection of the intracavity beam from the jet. The optimized intracavity beam should be at the desired height throughout the cavity; if it is not, it is indicative of a problem with the previous alignment, which should be repeated more precisely. In particular, the precise orientation of the jet perpendicular to the optical table is essential.

The final requirement in the alignment is to precisely set the separation of M1 and M2, which controls the cavity spatial mode. As discussed by Valdmanis [31], variation of the spacing results in a series of stable and unstable cavity modes, whose size (at the output) increases with decreasing separation. For small separations, a large mode is obtained, which becomes crescent shaped, and finally cannot be sustained for sufficiently small separation. Best operation is obtained for slightly larger separation, at the next stable mode that can be obtained. This behavior is observed by adjusting the translation of M1 and M2 symmetrically with respect to the jet (using the translation stage micrometers for reference), and viewing the spatial mode as described in Section A.4. After each adjustment of the translation, M5 and OC should be readjusted for maximum power. It was found that the stable mode desired was obtained over a range of 0.5 mm in the separation; a separation close to the center of this range was chosen.

The final outcome of this stage of the alignment should be a stable, Gaussian mode, and an intracavity beam that is parallel to the optical table at all points. The output power, for an input power of 2 W, and a 2% output coupler, should be approximately 400 mW.

A.5.2 Linear Cavity, Gain and Absorber

Once the alignment described above is complete, the cavity shown in Fig. A.2(b) is aligned. This is performed by placing M3 in the cavity, and ensuring that the fluorescence spot is imaged at the correct height in the direction of M4. Then M4 is placed to image the spot towards M5, at the correct height. M4 is placed at a distance from M3 that preserves the diameter of the fluorescence spot defined by the iris placed between M3 and M2. M5 is then repositioned as shown in Fig. A.2(b), and adjusted to retroreflect the beam, obtain lasing, and optimize the output power. The separation between M3 and M4 should be adjusted, by translating M4 and reoptimizing the output power with M5, until the same cavity mode obtained in alignment described in the previous subsection is recovered. The intracavity beam should be parallel to the optical table, and any deviation is likely due to slight misalignment of M3 and M4; this should be corrected by viewing the fluorescence spots, and repeating the above procedure. An output power of approximately 270 mW should be obtained. Now the absorber jet, which should only be circulating pure EG at this point (at a pressure of 16 psi), is moved into the beam between M3 and M4, near the focus, and at Brewster's angle with respect to the intracavity beam. It may be necessary to slightly adjust M5 to regain lasing; once this is accomplished, the absorber jet should be rotated to minimize the surface reflection of the intracavity beam, indicative of correct positioning at Brewster's angle. M4 may need to be translated slightly to regain the correct Gaussian spatial mode, and the output power should be approximately 260 mW.

A.5.3 Ring Cavity

Now the cavity shown in Fig. A.2(c) can be aligned, simply by adjusting M5 and OC to reflect the beam around the ring cavity. Because the total cavity length in the ring cavity is greater than the linear cavity shown in Fig. A.2, it may be necessary to adjust the separation between M3 and M4 slightly to recover the desired cavity mode. An output power of approximately 100 mW per beam should be obtained. The final step in the alignment of the CW laser before mode-locking is obtained is the addition of the prism sequence P1-P4, shown in Fig. A.1. The prisms should be added without adjusting any of the rest of the cavity, and it is useful to view the fluorescence spots transmitted through the prisms as P1 through P4 are aligned. The fluorescence spots should pass through the prisms near the apices, and correct orientation of the prism at Brewster's angle can be obtained by noting that the deviation of the fluorescence spots is at an extremum when the prism is oriented at Brewster's angle. Once the fluorescence spot has been aligned correctly from P1 to P4, the final prism P4 should be translated until the fluorescence spot from P4 on M5 overlaps with the spot from M4 on M5. When this is achieved, lasing can be regained. The prisms are then all adjusted to yield maximum output power, by rotation, tilt, and translation, keeping the beam as close as possible to the prism apices. The correct adjustment of the tilt of the prisms can be determined by monitoring the weak reflections from the two prism surfaces. Both reflections from any given prism should be collinear, and can be observed far from the laser. The output power should be approximately 100 mW per beam at this stage.

A.5.4 Achieving Mode-Locking

The final stage in the alignment, which is to achieve mode-locking, should be performed with a pump power of 4-5 W. A stock solution of 2 g of DODCI in 200 ml of EG is slowly added to the EG circulating in the absorber jet. As the DODCI is added, the output power of the laser will decrease. The absorber jet can be positioned at the focus of the absorber cavity by maximizing the output power of the CPM at low DODCI concentrations. The jet should be moved slightly away from the focus for best operation. At a concentration of approximately 0.24 g/l signs of structure with a period of the round trip time of the cavity are observed in the photodiode trace. More DODCI is added, and eventually mode-locking is achieved. This requires adjustment of the position of the absorber jet, and may require adjustment of the pump pointing mirror M7. To obtain the shortest pulses, prism P1 should be translated parallel to its base, to increase the length the intracavity beam travels through the prism material. For a pump power of 4 W, stable mode-locking was routinely achieved at a concentration of approximately 0.75 g/l, and an average output power of 25 mW per beam.

A.6 Routine Maintenance of Laser

Immediately after replacement of the dyes, the only adjustments to the CPM normally required are to M7, which compensates for drift of the pump laser pointing, and to the position of the absorber jet, which affects mode-locking. Cleaning of the optics is not necessary, because of the clean air environment in which the laser is operated.

After a period of approximately two weeks, a noticeable degradation in the laser performance becomes apparent, due to degradation of the laser dyes. This is evidenced by poor mode-locking, and accompanying fluctuations and instabilities in the laser output. It is possible to add a small amount of DODCI to the absorber solution, but eventually it becomes necessary to replace the dyes completely. Dye replacement is a fairly simple procedure that does not require repetition of the entire alignment procedure described in Section A.2. The old dye filters and solutions are removed, and replaced with clean filters and new EG (occasionally methanol is circulated throughout the system for cleaning). The stock Rhodamine tetrafluoroborate solution is prepared as described in Section A.2, and the standardized quantity determined by absorption measurement is added. It is not necessary to measure the absorption every time the dyes are replaced. Then, with the pump laser at 2 W, CW lasing is recovered. This will usually require adjustment of the pump pointing, and the absorber jet position. Occasionally, it is necessary to slightly adjust M5 and OC to optimize the output power, which should be the same obtained in the original alignment of the cavity. Then the same procedure described in Section A.2 for addition of DODCI to achieve mode-locking is repeated. It was found that this simple dye replacement procedure was very reliable, and was capable of restoring the CPM to a consistent state. The advantages associated with avoiding the complete realignment are tremendous, and make the laser a much more useful tool for experiments.

A.7 Performance of Laser

At a pump power of 4 W, stable mode-locking was obtained with average output powers of 20-35 mW per beam. The pulse width could be varied from a minimum of approximately 80 fs to a maximum on the order of 300 fs. The spectrum of the laser extended from approximately 6200 to 6300 Å with 300 fs pulses, and from 6100 to almost 6400 Å with 80 fs pulses. The average output power was stable to a few percent, and mode-locking could be maintained during significant variations in pump power.

References

[1] T.H. Maiman, *Nature* **187**, 493 (1960).

[2] M. DiDomenico, *J. Appl. Phys.* **35**, 2870 (1964).

[3] L.E. Hargrove, R.L. Fork, and M.A. Pollack, *Appl. Phys. Lett.* **5**, 4 (1964).

[4] A. Yariv, *J. Appl. Phys.* **36**, 388 (1965).

[5] P.W. Smith, M.A. Duguay, and E.P. Ippen, *Progress in Quantum Electronics* **3**, 107 (1974).

[6] A. Yariv, *Quantum Electronics, 2nd Ed.*, (Wiley, New York, 1975), Chapter 11.

[7] J. Hermann and B. Wilhelmi, *Lasers for Ultrashort Light Pulses,* (North-Holland, Amsterdam, 1987), which is a revised English translation of *"Laser für ultrakurze Lichtimpulse,"* (Akademie-Verlag, Berlin, 1984).

[8] P.-T. Ho, L.A. Glasser, E.P. Ippen, and H.A. Haus, *Appl. Phys. Lett.* **33**, 241 (1978).

[9] M.B. Holbrook, W.E. Sleat, and D.J. Bradley, in *Picosecond Phenomena II*, Vol. 14 in the Springer Series in Chemical Physics, R.M. Hochstrasser, W. Kaiser, and C.V. Shank, eds., (Springer-Verlag, Berlin, 1980), p. 26.

[10] See, for example, literature on the "Satori" 774 dye laser, Coherent Inc., 3210 Porter Drive, P.O. Box 10042, Palo Alto, CA, 94303.

[11] B.B. Snavely, in *Dye Lasers, 3rd. edition*, Topics in Applied Physics Vol. 1 of the Topics in Applied Physics Series, F.P Schäfer, ed. (Springer-Verlag, Berlin, 1990), p. 91.

[12] *Dye Lasers, 3rd. edition*, F.P. Schäfer, ed. (Springer-Verlag, Berlin, 1990).

[13] See Ref. [7], Chapter 6.

[14] B. Wilhelmi, E. Heumann, and W. Triebel, *Kvant. Electr.* **3**, 732 (1976).

[15] D. von der Linde, *IEEE J. Quantum Electron.* **QE-8**, 328 (1972).

[16] E.P Ippen, C.V. Shank, and A. Dienes, *Appl. Phys. Lett.* **21**, 348 (1972).

[17] J.A. Valdmanis, R.L. Fork, and J.P Gordon, *Opt. Lett.* **10**, 131 (1985).

[18] P.M.W. French, J.A.R. Williams, and J.R. Taylor, *Revue Phys. Appl.* **22**, 1651 (1987).

[19] P.F. Moulton, *J. Opt. Soc. Am. B* **3**, 125 (1986).

[20] J. Goodberlet, J. Wang, and J.G. Fujimoto, *Opt. Lett.* **14**, 1125 (1989).

[21] N. Sarukura, Y. Ishida, H. Nakono, and Y. Yamamoto, *Appl. Phys. Lett.* **56**, 814 (1990).

[22] E.P. Ippen, D.J. Eilenberger, and R.W. Dixon, in *Picosecond Phenomena II*, Vol. 14 in the Springer Series in Chemical Physics, R.M. Hochstrasser, W. Kaiser, and C.V. Shank, eds., (Springer-Verlag, Berlin, 1980), p. 21.

[23] J.P. van der Ziel, W.T. Tsang, R.A. Logan, R.M. Mikulyak, and W.M. Augustyniak, *Appl. Phys. Lett.* **39**, 525 (1981).

[24] P.W. Smith, Y. Silberberg, and D.A.B. Miller, *J. Opt. Soc. Am. B* **2**, 1228 (1985).

[25] W.H. Knox, *IEEE J. Quantum Electron.* **QE-24**, 388 (1988).

[26] C.V. Shank, R.L. Fork, R. Yen, R.H. Stolen, and W.J. Tomlinson, *Appl. Phys. Lett.* **40**, 761 (1982).

[27] R.L. Fork, C.H. Brito Cruz, P.C. Becker, and C.V. Shank, *Optics Lett.* **12**, 483 (1987).

[28] E.S. Wachman, D.C. Edelstein, and C.L. Tang, *Optics Lett.* **15**, 136 (1990).

[29] D.C. Edelstein, Ph.D. thesis, Cornell University, Ithaca, New York, 1990.

[30] R.L. Fork, C.V. Shank, C. Hirlimann, R. Yen, and W.J. Tomlinson, *Optics Lett.* **8**, 1 (1983).

[31] J.A. Valdmanis and R.L. Fork, *IEEE J. Quantum Electron.* **QE-22**, 112 (1986).

[32] O.E. Martinez, R.L. Fork, and J.P. Gordon, *Opt. Lett.* **9**, 156 (1984).

[33] O.E. Martinez, R.L. Fork, and J.P. Gordon, *J. Opt. Soc. Am. B* **2**, 753 (1985).

[34] R.L. Fork, B.I. Greene, and C.V. Shank, *Appl. Phys. Lett.* **38**, 671 (1981).

[35] R.L. Fork, O.E. Martinez, and J.P. Gordon, *Opt. Lett.* **9**, 150 (1984).

[36] For a discussion of solitons in optical fibers, see Y.R. Shen, *The Principles of Nonlinear Optics*, (Wiley, New York, 1984), p. 517ff, and references therein.

[37] M.B. Johnson, Ph.D. thesis, California Institute of Technology, Pasadena, California, 1988.

[38] J.A. Valdmanis, private communication.

[39] See, for example, F.A. Jenkins and H.E. White, *Fundamentals of Optics, Fourth Edition*, (McGraw-Hill, New York, 1976), pp. 167-170.

[40] See Ref. [7], p. 67.

[41] M.J. Rosker, Ph.D. thesis, Cornell University, Ithaca, New York, 1987.

[42] M. Dantus, private communication.

[43] A. Watanabe, H. Saito, Y. Ishida, and T. Yajima, *Optics Comm.* **69**, 405 (1989).

[44] T. Kurobori, Y. Cho, and Y. Matsuo, *Optics Comm.* **40**, 156 (1981).